

Title

Physical phenomena during nanoindentation deformation of amorphous glassy polymers

First author: Prakash Sarkar

PhD student, Department of Metallurgical Engineering and Materials Science, Indian Institute of Technology Bombay, Mumbai- 400076, Maharashtra, India

ORCID: 0000-0002-4404-916X

Second author: Prita Pant

Professor, Department of Metallurgical Engineering and Materials Science, Indian Institute of Technology Bombay, Mumbai- 400076, Maharashtra, India

ORCID: 0000-0002-0807-4157

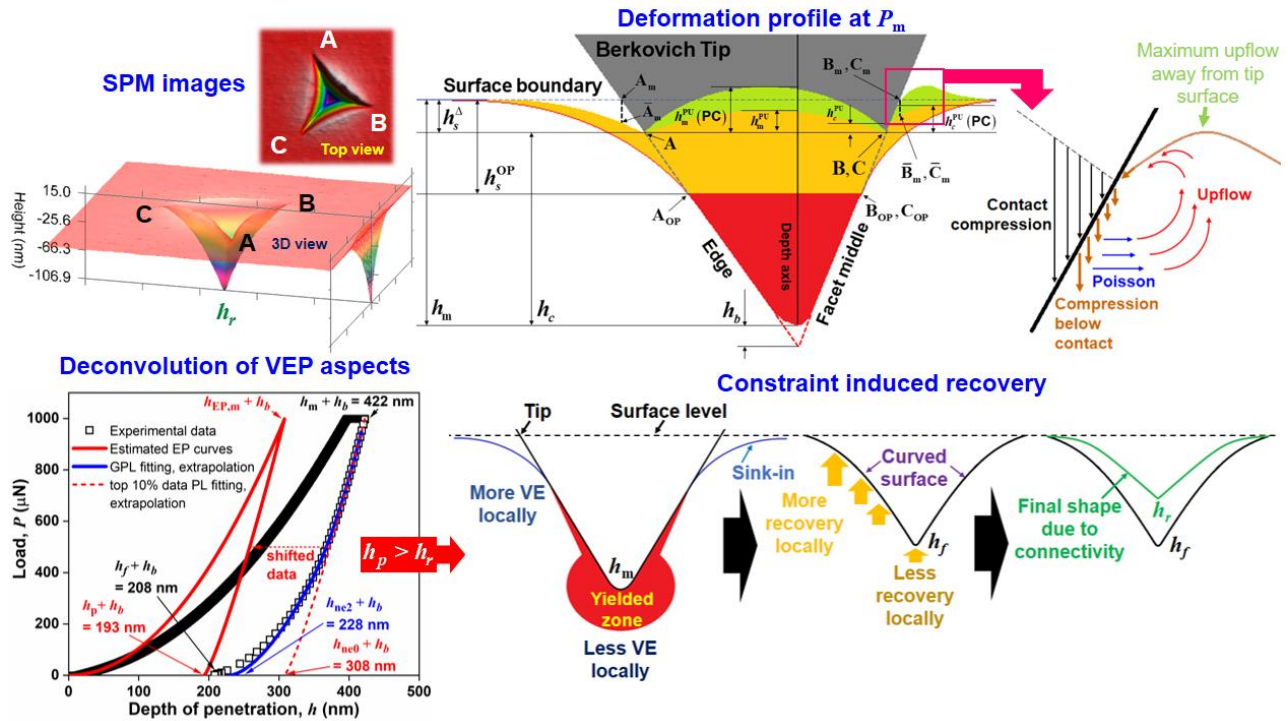
Corresponding author: Hemant Nanavati

Professor, Department of Chemical Engineering, Indian Institute of Technology Bombay, Mumbai- 400076, Maharashtra, India

*E-mail: hnanavati@iitb.ac.in

ORCID: 0000-0002-5982-6531

Table of Contents (TOC) graphic



Abstract

In this work, we examine material phenomena in glassy polymers during Berkovich nanoindentation, a form of locally imposed deformation. We consider both, thermoplastics (PC and PMMA) and thermosets (partially and maximally crosslinked SU-8 epoxy). Visco-elasto-plastic (VEP) effects occur simultaneously, from the onset of glassy polymer nanoindentation. Visual observation via *in-situ* nanoindentation indicates mainly sink-in during loading, with pile-up after unloading. Scanning Probe Microscopy (SPM) indicates significant volume conserving upflow (below the tip) for these compliant materials, with high geometric fractional contact depth at maximum displacement (including blunt height, h_b), $\frac{h_c^\Delta}{h_m^\Delta} \sim 0.9$. Considering the Berkovich tip as a family of cones, with cone angles ranging over the included angles of the tip, enables contact area calculation and a visual depiction of the upflow and the displacement paths below the tip. The combination of SPM and P - h data, indicates a mixed comparison with uniaxial deformation, with conventionally defined hardness, $H < 3\sigma_y$ and nanoindentation modulus $E_N > E$. By rationally removing viscoelastic (VE) effects during loading, we find instant, zero-time hardness $H_{L0} > 3\sigma_y$. Constraint-induced VE recovery of the highly yielded tip-apex region is consistent with the significant constraint effects on the conventionally defined E_N and H_{L0} for compliant materials such as glassy polymers.

Keywords: Nanoindentation Phenomena; Upflow; Scanning Probe Microscopy (SPM), Viscoelastoplastic (VEP) Deformation, Glassy Polymers, Compliant materials.

1. Introduction

Nanoindentation enables determination of material behaviour of very small systems and devices [1] over a region $\sim 10 \mu\text{m}^2 - 100 \mu\text{m}^2$, and up to a depth of $\sim 100\text{nm} - 5 \mu\text{m}$. Also, along with bulk measurement methods such as uniaxial, shear, torsion, bending, etc., it can enable investigation of mechanical behaviour over multiple scales. The material response to nanoindentation loads, is significantly richer in variety and distribution, than that to bulk loading methods. Deformation via bulk loads is broadly uniform, i.e., either tensile or compressive for uniaxial loads, or well graded from tensile to compressive for bending experiments, or measurable shear. Only if the deformation is beyond the elastic limit, does plastic flow occur. Viscous effects, which participate, depending on the rate of deformation, do so uniformly over the bulk. In contrast, nanoindentation is locally imposed deformation. It is constrained, constraint-forced and non-uniform. Localized elastic behaviour and viscoplastic (VP) flow occur simultaneously, and exhibit a complex distribution, from the onset of measurable deformation.

The nanoindentation process, is characterized by the relationship between the applied load, P (up to the maximum load, P_m), and the resultant penetration depth (for load-controlled experiments), h (up to the maximum depth, h_m), followed by that in the unloading process, which is considered elastic recovery. The framework developed by Oliver and Pharr [2]–[4] (OP), has been employed almost universally, since they have demonstrated its validity over a broad range of elasto-plastic (EP) materials. The OP framework follows the elastic nanoindentation analysis of Love [5] and Sneddon [6]–[8] (LS) to correlate the $P-h$ behavior, at the onset of the elastic unloading, to contact depth at full load, $h_c = h_m - h_s$ (h_s is the non-contact sink-in depth, a consequence of nanoindentation).

In addition to sink-in, nanoindentation also gives rise to pile-up. A pile-up is a surface level bulge adjacent to the indent [9]–[20], which, if small, is ignored by the OP framework. For significant pile-up, the framework by Loubet [21] considers $h_c \sim \zeta h_m$, where, $\zeta > 1$ [13], [14], is a constant.

The LS analysis essentially correlates the elastic loading $P-h$ data in terms of the elastic constants, including the modulus, E , and the Poisson ratio, ν . The contact depth corresponds to a boundary condition, in their analysis. This means that the effective true stress is correlated with P/A_c , where A_c is the geometry based, depth-correlated projected contact area; the strain is also implicitly correlated to the same indentation depth. An assumption, also implicit in this framework, is that the loading causes vertically downward compressive displacement, and unloading leads to vertically upward recovery; during loading the volume conserving Poisson widening is lateral, moving radially away from the contact with the indenter tip.

The OP method is not applicable when there is significant pile-up. This method employs the ideas of Bulychev *et al.* [22], of employing stiffness, $S = (dP/dh)|_{P_m, h_m}$, the unloading onset slope, to separate the strain measure due to the overall penetration, from the contact area measure. It thus attempts a separation of the elastic contributions from the EP deformation. The OP method retains the basic idea of the LS method to relate the contact region size to the elastic component of the deformation. Here, the LS analyses phenomena have been mapped to the elastic *unloading* $P-h$ data, in terms of S , to yield h_c . These have been employed to obtain nanoindentation properties, i.e., the nanoindentation modulus, $E_N \approx (1-\nu^2)S\sqrt{\pi}/(2\sqrt{A_c})$ (for relatively compliant materials such as polymers) [23], and the hardness, $H = P_m/A_c$. For a broad set of EP materials, $E_N \sim E$ and $H \sim 3\sigma_y$ (σ_y is the yield stress).

In our work, we examine amorphous glassy polymers. This is a class of yield exhibiting compliant materials, which were not present in the range of materials which led to OP framework. However, they have still undergone nanoindentation analyses via the OP method, although empirical corrections have been reported (e.g., [24], [25]).

Numerical simulation approaches which implement Finite Element (FE) Methods (FEM) or Finite Element Analyses (FEA) [26]–[54]), broadly identify materials parameters (including via user-defined models) and phenomena to match the P - h data, and then infer insights into other phenomena such as stress and strain distributions in the sample. However, in case of a complex nanoindentation deformation of yield-exhibiting compliant materials, these computations as well as other predictive models, need to be consistent with a greater range of experimental observations, beyond P - h data.

Thus, our objective experimental analysis recognizes the high compliance amorphous glassy polymer, and identifies various aspects of material behaviour. *In-situ* observation of nanoindentation a glassy polymer, yields qualitative insights into this deformation phenomenon. Topological imprint images indicate that the contact region is significantly greater than the OP framework estimate, and less than via the Loubet method. This is because compliant materials undergo deformation more easily, giving rise to the greater volume-conserving material upflow beneath the indenter tip, whose effects we account for in our approach. Based on such “direct observations”, we provide indentation profiles and suggest the deformation flow paths. Along with the nanoindentation P - h data, we estimate the conventionally defined nanoindentation properties, E_N and H . We interpret these estimates in terms of the material behaviour, and deconvolute the various components of the viscoelastoplastic (VEP) deformation into VE, EP and elastic components. These provide insights into the effects of constraints of the surrounding region, on the locally imposed deformation.

Predictive modelling, while successful for bulk glassy polymer behavior, needs to incorporate a wider range of experimental observations of nanoindentation phenomena. FEA or FEM also need to be consistent with a range of phenomena, such as those identified in this work. An analysis such as ours, would thus provide guidelines to the way forward for formal characterization of polymer nanoindentation, in terms of predictive modelling as well as numerical simulations.

2. Background

The OP method provides the metrics, reduced modulus, $E_r = \left[\left((1-\nu^2) E_N^{-1} \right) + \left((1-\nu_i^2) E_i^{-1} \right) \right]^{-1}$ and H , of the EP nanoindentation deformation phenomena (ν_i and E_i are the Poisson's ratio and elastic modulus of the indenter, respectively; for less compliant materials, the indenter compliance makes a measurable contribution). This method considers that both, the elastic as well as plastic components of the loading are parabolic, i.e., $P \propto h^2$ [10]; the unloading data (in the range from $0.2 P_m$ to $0.95 P_m$), corresponding to elastic recovery, are modeled by a power law (PL), $P = B(h - h_f)^m$; the resulting estimate of the stiffness, S , yields $h_c = h_m - h_s = h_m - (\varepsilon P_m / S)$. For a conical tip, $\varepsilon = 0.72$ (obtained by combining with the LS result, $(h_c/h_m) = (2/\pi)$); for a Berkovich tip, $\varepsilon = 0.75$ [2]; for a flat punch tip, $\varepsilon = 1.0$). For an ideal Berkovich tip, $A_c = C_0 h_c^2$, where $C_0 = (3\sqrt{3} \tan^2 \alpha) \approx 24.5$ ($\alpha = 65.27^\circ$ is the semi angle of the Berkovich tip). The wear of the tip apex with usage is accounted for by regular calibration with standard materials (usually quartz), whose H and E_r are known. The back-calculated contact areas are fit to $A_c = \sum_{i=1}^8 C_i h_c^{2-(i-1)}$, where C_i are the bluntness constants [2]. Another approach considers the wear in terms of the blunted height, h_b , as $A_c^\Delta(h_c) \approx 24.5 \times (h_c + h_b)^2$ [27], [55]–[61].

OP justified their relationship between S and h_c , by comparing their computed A_c , with those obtained by direct imaging of the imprint area, on six EP materials: aluminum (modulus ~ 68 GPa), fused silica, soda lime glass, quartz, tungsten, sapphire (modulus ~ 440 GPa); we will call these materials the OP materials. This imprint area is formed by connecting the outer corners of the permanent Berkovich edge imprints (length= a) into a triangle [2], [23], [62]; i.e., $A_c^\Delta = \sqrt{3}a^2/4$. For indentation of compliant but yield-exhibiting materials such as glassy polymers (moduli $< \sim 10$ GPa), h_c values would be much greater, and the A_c calibration needs to extend to corresponding depths. Therefore, A_c calibration in terms of OP-based h_c , has been reported via Polycarbonate (PC) [25], [63] and other soft materials such as PS-1TM[63], PS-4TM[64], PS-6TM [65], [66] photoelastic polymer coating (Vishay Micro-Measurements, USA), and Polymethyl methacrylate (PMMA)[67]. In this context, limiting h_f/h_m values of 0.7 [2] or 0.83 [68] have been recommended for applicability of the conventional OP method for OP-type materials.

Progress beyond the OP framework, in describing the nanoindentation deformation phenomena, has been broadly in two categories. One category is in terms of numerical simulations such as FEA, as described in the previous section. The second category is in terms of estimating S and A_c . Modifications such as polynomial fits (as well as normalizations P/P_m and h/h_m) to the unloading data [69]–[72], have been reported. Among these, there was also recognition [71], [72] that in load controlled experiments, h is the dependent variable and P is the independent variable. However, on applying these OP-type concepts to a VE material (the polymer, PA12), resulted in an unphysical fitted value, $h_f \sim 10^8$. We note that these analyses have achieved excellent R^2 values in their fitting. However, fidelity to the phenomena, requires examination of the fitting residuals as well; based on such examination, our earlier work [73], [74], suggests non-applicability of the PL equation for polymeric systems, over the prescribed unloading range. Therefore, the corollary that the OP

method (including for use as a standard [25], [63]–[67]) could determine h_c for polymers, also needs to be re-examined.

The contact region can be identified via direct imaging of the surface topography; e.g., via methods such as atomic force microscopy (AFM), scanning electron microscopy (SEM), Scanning Probe Microscopy (SPM), optical microscopy, etc. The pile-up indicated above as reported in the literature, has been discerned via such topographical images of the residual nanoindentation imprint. This pile-up is added to the h_c , for calculation of A_c ; $A_c(h_c) \approx 24.5 \times (h_c + h_m^{\text{PU}})^2$, where h_m^{PU} is the imaged maximum post-unload pile-up (PU) height (see [14], [15]). A report on polymer nanoindentation [15], suggests that any sink-in should be disregarded if there is pile-up (observed via SPM), so that $h_c = h_m + h_m^{\text{PU}}$. This method assumes that the entire pile-up, exists at full-load, and is in load-bearing contact with the tip. A more rigorous method [11], [12], [16]–[20], considers the area of a sector of the circle of maximum height, h_m^{PU} , as the pile-up contact area, to be added to the OP-based A_c . Randall *et al.* [75] have considered the SPM residual imprint which included the imprint of the additional circle-sector pile-up contact as A_c .

One reported [76] claim of correspondence between the OP method and the imaged contact area for polymers, needs to be scrutinized, because in that work, (i) there is inconsistency in their reported depths between the SPM images and the P - h data and (ii) their reported E_r and H values are far removed from the corresponding values widely reported [25], [77], [78] for the same polymers and (iii) their H estimates, based via unspecified image analysis of the indent, does not correspond with those when the A_c is estimated by considering their SPM top views and vertical sections [2], [23].

AFM [56], [79]–[85], and SPM (scanning probe microscopy) [15], [62], [75], [86], [87] are processes where the indenter tip itself scans the residual indent, and enables easy determination of

the A_c . SEM [88] and optical photographs [89] of the residual imprints, have also been employed to estimate A_c . Some approaches [56], [82], have adopted Johnson's spherical conical cavity model [90], to correlate the indentation properties to the parameters of vertical sections of the residual imprint topography, at different load levels. Their analyses are based on accepting the validity of the OP framework, and modifying the Johnson model to match the OP framework.

Physical phenomena during nanoindentation have been modeled by Voyiadjis *et al.* [77], [78], [91], [92] in terms of shear transformations and shear transformation zones, and in our group [74], in terms of activation volume. In these works, only elastic and plastic components have been considered; the VE components are considered inactive, since the analyses are during rapid unloading, after a significant hold time. The OP method has been extended for decomposing the VEP contributions to polymer deformation as well [93], [94].

In all cases, over the broad gamut of the literature on polymer nanoindentation analyses, the physical phenomena have been inferred via modeling frameworks, which are based on nanoindentation properties, E_r and H , which, in turn, have been obtained via the OP framework. A comparison [95] of the OP and Loubet methods for analysing polymer nanoindentation, indicates significantly different estimates of the nanoindentation properties.

There is no evidence that validates any version of the OP method on polymers, in terms of the estimate of h_c , from the unloading $P-h$ data. Nor is there evidence to justify the Loubet method, that the complete depth, in addition to the pile-up, is in load-bearing contact. Such evidence if found, should be via direct *in situ* observation or via rational and rigorous analyses of the imprints, to infer the load-bearing full-load A_c , including pile-up, and its relationship with the unload onset tangent. Such a method was implemented to validate the OP method [2] for EP materials.

As part of this work, we examine how the conventionally defined E_N and H , when estimated faithfully as per their definitions, provide clues to the actual deformation phenomena. We aim to provide a qualitative, model-free representation of the actual phenomena, based on our experimental observations on glassy polymer nanoindentation. This description of the evidenced phenomena, could be the basis of predictive modeling or computational methods such as FEA, at a subsequent stage. Such understanding is necessary so that the FEA inputs for the user defined models, reproduce all the phenomena that can be inferred from macroscopic experiments, and provide further insights, such as quantified distributions of stress and strains within the material.

3. Materials and sample fabrication

3.1. Thermoplastics

Among the materials we investigate here are commercial grade acrylic sheet (PMMA), and commercial PC, which represent thermoplastics. At room temperature, these polymers are glassy. Their high transparency indicates that they are amorphous. In the literature, they have been investigated well for bulk properties as well as via nanoindentation [77], [78], [89], [96]–[99].

3.2. Thermosets

We consider SU-8 epoxies, cross-linked to two extents, as representative glassy thermosets. The SU-8 2050 grade epoxy resin employed in our experiments and analyses, has been supplied by MicroChem Corporation™. The samples are fabricated on silicon (Si) substrate, by following the standard photo-lithography process [74], illustrated in [Fig. 1](#). For the less crosslinked sample (called PB05), we have carried out the post-exposure baking (PB) step for 5 min only. For the maximally crosslinked sample (called HB15), we have performed 30 min of PB, after which, we have continued

to the hard baking (HB) step for 15 min. To evaluate the extent of cross-linking of SU-8, we have collected *in-situ*, Fourier Transform Infrared Spectroscopy (FTIR) spectra at the baking temperature (PB and HB) [100], [101], by employing a 3000 Hyperion FTIR Microscope with Bruker Vertex 80 (Germany) spectrometer. We find (Appendix A) that PB05 corresponds to 82% cross-linking, and HB15 corresponds to 95.5% cross-linking. This difference in the extents of cross-linking, gives rise to a difference in response to nanoindentation.

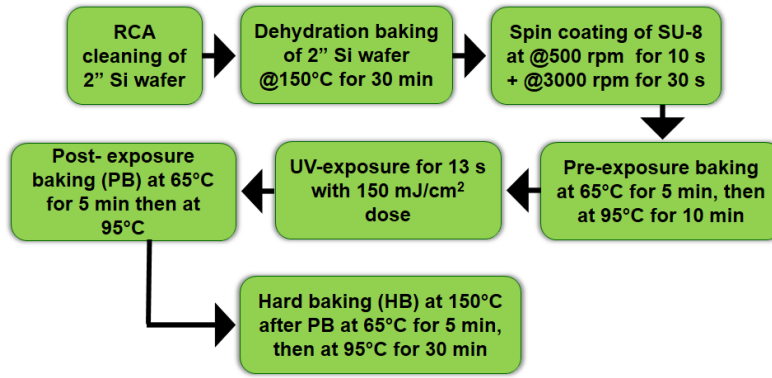


Figure 1: Schematic of the steps involved in the standard photo-lithography process.

4. Experimental protocol

4.1. Nanoindentation Experiments

Nanoindentation experiments have been performed with a diamond Berkovich tip (pre-computed h_b) via a nanoindenter (TI Premier, Bruker corporation™) on two cross-linked SU-8 epoxies (PB05, HB15), PC, and PMMA. The residual indent imprints are acquired via SPM imaging.

We have first evaluated h_b (i.e., calibrated the tip) at different experiment times (0 days to 600 days) from the first day of tip usage. We have followed the conventional area calibration procedure [2] at each time, making 30 tip area calibration indents on the quartz standard. The maximum load, P_m , varies from 100 μN for the first indent, progressively up to 10,000 μN , for the thirtieth indent.

In our nanoindentation experiments, we account for thermal drift variation during indentation [102]. We also verify that (i) there is negligible thickness and roughness variation along the sample surfaces [103], [104], (ii) there are no pop-in or large load deflections in $P-h$ data during loading and unloading [105]

Since an epoxy surface is likely to adhere to the tip surface [106], [107], we have coated the surfaces of our fabricated PB05 and HB15 with 2 nm gold (which will contain ~ 14 layers of gold atoms) via a controlled and optimized sputter process (Orion Sputter PHASE, AJA international, Inc.). This gold coat acts as the barrier between the tip and sample surfaces, without affecting the sample's nanoindentation properties. The PC and PMMA samples remain uncoated in our experiments.

All samples have been indented by applying a constant $0.1 \text{ /s } \dot{P}/P$ loading rate. We consider two P_m levels, $1000 \text{ }\mu\text{N}$ and $9000 \text{ }\mu\text{N}$. Although the $1000 \text{ }\mu\text{N}$ load results in penetrations well beyond the Hertzian limits reported limits of indentation size effects [92], [108], the $9000 \text{ }\mu\text{N}$ load provides for effective comparison with the data available in the literature [77], [78], [109], [110]. For each sample, we have performed four indents at each load. To overcome VE effects on unloading data, we provide sufficient holding time (70 s for cross-linked SU-8, 100 s for PC and 150 s for PMMA) for the deformation to reach a plateau, followed by a rapid unloading rate (2 s unloading for all samples, at both P_m values) [14], [111].

4.2. Sample Surface Analysis

We carry out this analysis in two ways. One way is the live, *in-situ* nanoindentation, and the other method is the post unload imprint analysis.

4.2.1. *In-situ* nanoindentation

We have carried out *in-situ* nanoindentation (Bruker Corporation™ indenter in Fei Quanta 3D FEG SEM) on PB05, with a diamond Berkovich tip. The PB05 surface has been coated with a 5 nm layer of gold to counter adhesion effects and to permit direct observation of the deformation.

4.2.2. Post unload surface topology analysis

We have acquired the residual indent impression images, employing the nanoindenter itself by scanning at an optimized frequency (for image clarity), i.e., at 0.8 Hz over areas, $7\mu\text{m} \times 7\mu\text{m}$ for PB05 and HB15 ($P_m = 1000 \mu\text{N}$), $10\mu\text{m} \times 10\mu\text{m}$ for PC and PMMA ($P_m = 1000 \mu\text{N}$), and $20\mu\text{m} \times 20\mu\text{m}$, for all samples indented up to $P_m = 9000 \mu\text{N}$.

5. Results and discussion

Our examination of the response of amorphous glassy polymers to Berkovich nanoindentation, involves identifying the various physical phenomena during nanoindentation deformation.

- We first examine the unloading P - h data, to rationally estimate the elastic portion of this segment.
 - Next, we examine the visible nanoindentation features, where we can consider our observations to be explicit evidence. We begin with live observation via *in-situ* indentation, the visible response of an amorphous glassy polymer (PB05) during nanoindentation.
 - Then we perform a rigorous analysis of the SPM images of the post-indentation imprints (based on exact tip geometry and bluntness). These images provide directly, the contact and non-contact geometry at full load. Combining the SPM data and the P - h data with *in-situ* visualization, we provide a basic schematic which describes the displacement pattern within the material
-

continuum, during the indentation process. These include the up-flow during contact deformation and the material indentation profile at full load.

- We determine next, the conventionally defined nanoindentation properties (E_r and H). These estimates provide clues to the physical phenomena during nanoindentation.
- We then examine the nanoindentation loading data and develop a framework, to decompose of the deformation into its EP and VE components. This deconvolution of the various components, provides insights into the constraint effects, on deformation and recovery.

5.1. Unloading Analysis: Viscoelastic Effects

We first consider simplified 3-element VE models to qualitatively represent time-dependent phenomena during unloading (Fig. 2). These are solid-like models, because for the glassy polymers considered here, the displacement becomes constant (creep rate ~ 0) beyond the respective implemented hold times. For either of these models, an ideal high rate (instantaneous) unloading curve would correspond an effective zero-time modulus, E_0 , and be free from flow effects.

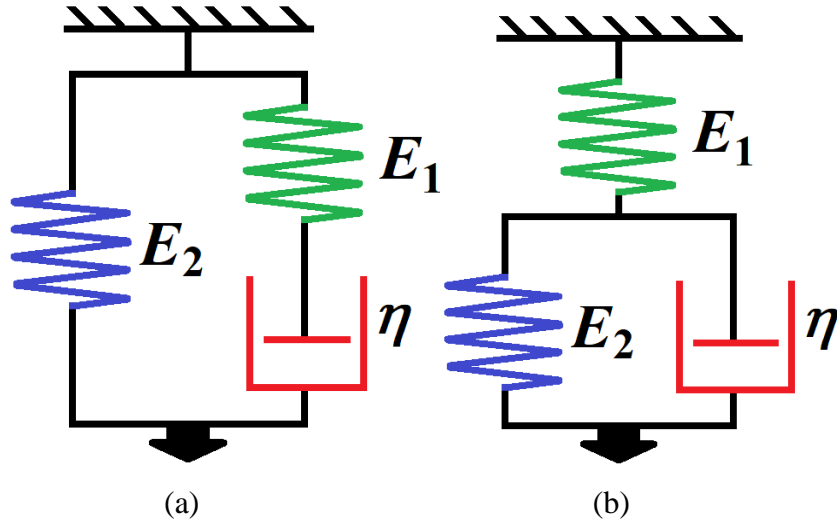


Figure 2: Schematic of three element solid model (a) Voigt model ($E_0 = E_1 + E_2$) and (b) Zener model ($E_0 = E_1$)

While instantaneous unloading is not possible, rapid unloading reduces VE effects. We examine further, the phenomena during unloading. Hence, while there are simultaneous elastic and non-elastic contributions to deformation during loading, part of the elastic component is recovered during rapid unloading. Additional recovery occurs over time, which is due to VE effects. We begin with the analysis of the unloading step.

5.1.1. Rate effects during unloading

Since unloading begins just after the hold period, the *set* rate is achieved by accelerating from constant load; the unloading ends with deceleration, as the load reaches zero. Hence, it is first necessary to identify the approximate E_0 regime, from within the unloading step.

In our load function, we have *set* nominal unloading time = 2 s (unloading rates, 500 $\mu\text{N/s}$ and 4500 $\mu\text{N/s}$, for $P_m = 1000 \mu\text{N}$ and from $P_m = 9000 \mu\text{N}$, respectively). This ensures that the instantaneous relative unloading rate, \dot{P}/P , and its variation with unloading time, throughout the unloading step, is independent of P_m . **Figure 3** contains the plots of the *measured* normalized unloading rate, \dot{P}/P_m , vs the normalized unloading P values, P/P_m , for all polymers as well as for the quartz standard. We observe that the constant *set* unloading rate range is from $\sim 0.3 P_m$ to $\sim 0.95 P_m$ ($\sim 0.98 P_m$, for $P_m = 9000 \mu\text{N}$). This constant \dot{P}/P_m range, depends primarily on the nominal unloading time and very slightly on P_m , but is independent of the sample material.

The deceleration in \dot{P}/P_m as the load reaches zero (P range from $\sim 0.3 P_m$ to zero), adds significant VE effects to the estimate of E_0 component. Therefore, we estimate the hypothetical non-elastic residual depth, h_{ne2} , corresponding to the 2 second unloading, *continuing* at the *set* rate, up to $P = 0 \mu\text{N}$. We describe next, a framework to estimate h_{ne2} . We then explore whether this first

approximation, $(h_m - h_{ne2})$, could correspond to the approximate E_0 (Fig. 2) elastic portion of the indentation displacement. The choice of this approximation, recognizes that VE effects begin immediately at the onset of unloading. The non-zero duration of this step, enables contribution of VE effects. However, the magnitude of the relative unloading rate, \dot{P}/P , increases as unloading progresses at the set rate. This increase in the nanoindentation recovery rate during this time, would be expected to resist the time-dependent phenomena. We explore this idea progressively in Sections 5.1.2 (significantly reduce VE effects) and 5.1.3 (qualitatively eliminate VE effects).

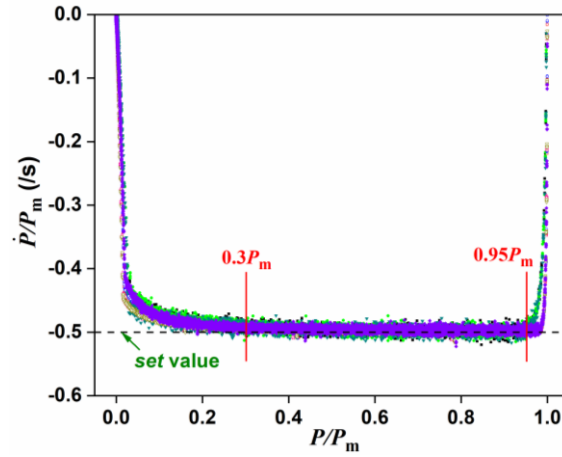


Figure 3: Actual normalized unloading rate vs normalized unloading P for all indents performed on PB05, HB15, PC, PMMA and quartz for $P_m = 1000 \mu\text{N}$ and $9000 \mu\text{N}$. The solid symbols are for $P_m = 1000 \mu\text{N}$ and open symbols are for $P_m = 9000 \mu\text{N}$. For the unloading step, the loading rate is -ve; its absolute value increases downward.

5.1.2. Modeling unloading data: Constant rate range

The conventional PL equation ($P = B(h - h_f)^m$) for modeling the unloading h - P data yields:

$$h = BP^{\frac{1}{m}} + h_{ne2}^{\text{PL}} \quad \text{eqn. 1}$$

The estimates of $h_{ne2}^{PL} = h|_{P=0}$ (considering constant power exponent, m), are unphysical; they are negative, or significantly lower than the experimental h_f (listed in Table 1). Therefore, the PL model for the unload data, is inappropriate for glassy polymer systems.

In contrast, we will find the estimate h_{ne2} (whose values are also listed – in the last row of Table 1) is likely to be relevant for onward analyses. These tabulated h_{ne2} values have been estimated next, by direct fitting of the h - P data (h is the dependent variable, in our load controlled (LC) experiments), to a generalized PL model, via the framework described next.

In this framework we generalize the relationship between $\ln P$ and $\ln(h - h_{ne2})$ recognizing that the tangent slope (power exponent), m , is not a constant, as in the PL model; i.e., it varies along the curve. For clarity, we represent the force metric, $F = \ln P$, and displacement metric, D , for the models for $\ln(h - h_{ne2})$. Therefore, we can write, $dD/dF = k_2 F^2 + k_1 F + k_0$ for quadratic fitting of the varying slope. k_0 , k_1 and k_2 are the fitting constants (the values are listed in [Supporting Information 1](#), along with the corresponding values and value ranges of the slope, $1/m$). Thus, for all the four polymers, we obtain the resultant relationships for h vs P (eqn. 2),

$$h = g P^{\frac{D_F}{F}} + h_{ne2} \quad \text{eqn. 2}$$

g is a fitted parameter and $D_F = \int_0^F (dD/dF) dF = D(F) - D(0)$. The details of this analysis are provided in [Appendix B](#).

We find that this GPL (Generalized Power Law) framework describes well the relationship between $h - h_{ne2}$ and P . The relative residuals of this fitted equation are small, scattered and random (up to

$\sim 0.03\%$), with $R^2 \sim 0.999$. The h_{ne2} values (last row of Table 1) obtained by fitting the entire constant \dot{P} range data to eqn. 2 (See [Supporting Information 1](#)), are physically viable.

The PL fit of P vs h (plotted in [Fig. 4\(a\)](#)), appears adequate superficially ($R^2 \sim 0.998$). Although the relative residuals are significantly greater than those via our GPL method ([Fig. 4\(b\)](#) and [Supporting Information 2](#)), they are still small, up to $\sim 2\%$, even in the low P - h region ($P \sim 0.20P_m$). Hence, in order to understand the inadequacy of the PL equation fitting for glassy polymers, we examine a magnified plot in the neighborhood of h_{ne2} ([Fig. 4\(c\)](#)) and of the experimental h_f . Here, we find that the PL equation fitted curve indicates a non-zero load, consistent with the unphysical fitted h_f value ($= h_{ne2}^{PL} = h|_{P=0}$).

Table 1: Nanoindentation depths, h_m , h_f , h_{ne2}^{PL} and h_{ne2} for $P_m = 1000 \mu\text{N}$ and $P_m = 9000 \mu\text{N}$.

h (nm)	P_m (μN)	PB05	HB15	PC	PMMA	Quartz
h_m	1000	405 ± 2	421 ± 1	565 ± 5	478 ± 8	--
	9000	1370 ± 11	1375 ± 7	1860 ± 16	1537 ± 10	287 ± 2
h_f	1000	191 ± 1	172 ± 1	300 ± 3	304 ± 7	--
	9000	529 ± 15	473 ± 7	983 ± 15	904 ± 4	133 ± 0
h_{ne2}^{PL}	1000	39 ± 5	-198 ± 24	111 ± 9	322 ± 5	--
	9000	347 ± 13	209 ± 6	810 ± 16	1033 ± 9	139 ± 1
h_{ne2}	1000	211 ± 2	206 ± 5	335 ± 11	336 ± 13	--
	9000	711 ± 9	697 ± 13	1119 ± 27	1062 ± 15	--

We first estimate the stiffness, S , which is a measure of the events at the immediate onset of unload, before the subsequent time-dependent phenomena occur.

For each indent, $S = dP/dh|_{P_m} = \left(dh/dP|_{P_m} \right)^{-1}$. Hence,

$$S = \left(\frac{gP^{\frac{D_F}{F}}}{P} \frac{dD}{dF} \right)_{P_m}^{-1} \quad \text{eqn. 3}$$

From our data-faithful GPL framework, we find (Table 2) $S(\text{PB05}) < S(\text{HB15})$ and $S(\text{PC}) < S(\text{PMMA})$. [Appendix B](#) discusses the comparison of our S estimates with those from literature methods.

Table 2: Calculated S ($\mu\text{N}/\text{nm}$) estimates via the GPL framework

P_m (μN)	PB05	HB15	PC	PMMA
1000	10.59 ± 0.09	11.02 ± 0.09	9.87 ± 0.04	12.22 ± 0.09
9000	30.63 ± 0.14	34.31 ± 0.06	27.97 ± 0.02	33.12 ± 0.07

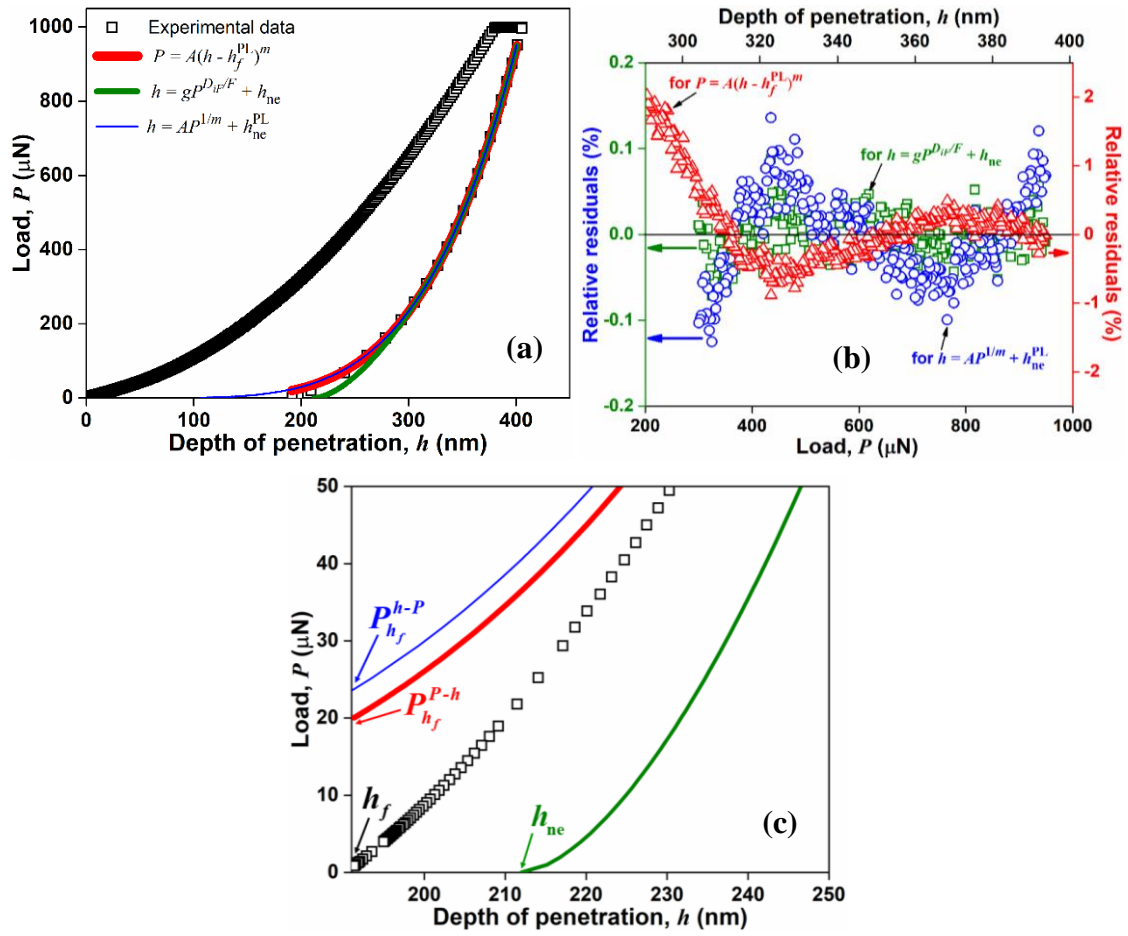


Figure 4: (a) P - h curve with fitted equation for $P_m = 1000 \mu\text{N}$ and (b) relative residuals from PL equation fitting for P data (red), PL fitting for h data (blue) and GPL fitting (green), (c) magnified portion near the residual depth for PB05.

In nanoindentation, $E_N \propto S/\sqrt{A_c}$, and E_N should scale with the uniaxial modulus. We discuss this further in [Section 5.3.4](#), after we discuss the phenomena that lead to the non-OP A_c for glassy polymers, in the upcoming sections. Our experimental results suggest that the GPL framework

described here, corresponds well with the unloading data for compliant VEP materials such as glassy polymers, in the same way that the conventional PL framework is valid for EP materials such as quartz, metals, etc. However, the variation in the exponent corresponds to a greater recovery – which suggests that unloading creep occurs, even though the fraction of unload modeled is that at constant \dot{P} and increasing \dot{P}/P . Thus, considering the constant \dot{P} range, only reduces the effect of unload creep, but does not eliminate it. We discuss the rational elimination of unload creep, in the next section ([Section 5.1.3](#)).

5.1.3. Modeling unloading data: Unloading onset range

The unloading step, although rapid, also contains viscoelasticity effects. In order to remove these time-dependent effects, we consider the PL fitting (analog of eqn. 1) of the *top* 10% of the unloading data at the set rate (from $0.95 P_m$ to $0.885 P_m$). The difference here, is that in eqn. 1 we replace h_{ne2}^{PL} with h_{ne0} . This is the expected residual depth after zero-time (instantaneous) unload (corresponding to E_0 in [Fig. 2](#)), i.e., if the PL exponent m were independent of P (continue to be constant from the onset of unload at $P = P_m$, to completion of unload at $P = 0$) The fitted parameters are listed in Table 3. The fitted data lie in a very small range, and there can be some uncertainty in the nonlinearly fitted parameters; e.g., the nonlinear fitting resulted in a different set of parameters for PMMA at 3000 μN . Since with a broad consistency, this step results in a small range of values for the exponent, $m \sim 1.24 \pm 0.03$, we have fixed the exponent $m \sim 1.25$. This fixing of m , does not change the quality of the fit ($R^2 \sim 0.9995$).

As expected, the fitted $h_{ne0} (\sim 0.7 h_m - \sim 0.8 h_m) > h_{ne2} (\sim 0.5 h_m - \sim 0.7 h_m)$. We verify the pure elastic nature of this hypothetical unload, which exhibit similarities in its signatures with those of the unloading $P-h$ data of nanoindentation of the quartz standard ([Appendix C](#)); these are:

- i. h_{ne0} increases with P_m .

- ii. B decreases with P_m
- iii. $m(\text{polymers}) \sim 1.24 \pm 0.03$, $m(\text{quartz standard}) \sim 1.28 \pm 0.03$, $m(\text{OP materials}) \sim 1.35 \pm 0.1$ [2].
- iv. For all polymers and for quartz, $S \propto \sqrt{P_m}$.

Table 3: PL Fitting of the top 10% of the constant rate unloading P - h data

	PB05			HB15		
P_m (μN)	1000	3000	9000	1000	3000	9000
m	1.23 ± 0.01	1.26 ± 0.00	1.23 ± 0.01	1.23 ± 0.01	N.A.	1.25 ± 0.01
B	0.42 ± 0.03	0.34 ± 0.00	0.23 ± 0.02	0.46 ± 0.02	N.A.	0.24 ± 0.02
$h_{\text{ne}0}$	289 ± 3	501 ± 15	996 ± 10	297 ± 1	N.A.	1023 ± 8
R^2	~ 0.9996	~ 0.9995	~ 0.9999	~ 0.9995	N.A.	~ 0.9998
	PC			PMMA		
P_m (μN)	1000	3000	9000	1000	3000	9000
m	1.21 ± 0.01	1.21 ± 0.00	1.23 ± 0.00	1.27 ± 0.02	1.25 (fixed)	1.26 ± 0.00
B	0.45 ± 0.02	0.32 ± 0.01	0.25 ± 0.01	0.45 ± 0.05	0.30 ± 0.00	0.25 ± 0.01
$h_{\text{ne}0}$	432 ± 6	758 ± 14	1440 ± 17	372 ± 11	658 ± 10	1195 ± 9
R^2	~ 0.9995	~ 0.9998	~ 0.9999	~ 0.9989	~ 0.9995	~ 0.9997

Over the small fitting range, we find corroborating phenomenological similarity between the polymers and quartz, in terms of the elastic aspects. Therefore, the PL unloading curve (constant m), is a qualitative approximation of pure elastic unloading. We address this aspect in [Section 5.4](#). Note that S is the same, whether we obtain it via the PL ($h_{\text{ne}0}$ basis) or via the GPL ($h_{\text{ne}2}$ basis).

In order to estimate the contact and non-contact geometry, we carry out a direct observation of the surface response: (i) We observe an indentation process live, via *in situ* indentation ([Section 5.2](#)). (ii) we perform topological analyses of the post-unload indented surface via SPM ([Section 5.3](#)).

5.2. Direct observation of nanoindentation

Here, we examine visually, one aspect of the physical response of the material to nanoindentation via *in-situ* monitoring. In [Fig. 5](#), we see that as the loading progresses followed by hold, the sinking indenter tip casts a gradually darkening shadow, over the entire surrounding region. This darkening reduces with distance, away from the surface-tip contact (for details see the video, [Supporting](#)

Information 3). As loading progresses, the darkening of the shadow bordering the tip surface indicates that that part of the sample surface, enters a region of greater shadow, i.e., below the visible surface, which is further away from the tip. Therefore, we infer that throughout the loading and hold steps for PB05, sink-in occurs along the edge, as well as along the facet of indenter.

During the rapid unloading step, the shadow cast by the indenter lightens. This lightening is greater in the regions very close to the surface-indenter contact, indicating that the sunk-in surface is rising. At the end of the unloading, there is a permanent imprint, corresponding to the non-elastic component of the deformation. In addition, there is a bright line about the indented region, corresponding to an elevation above the average surface level. This is the post-unload pile-up.

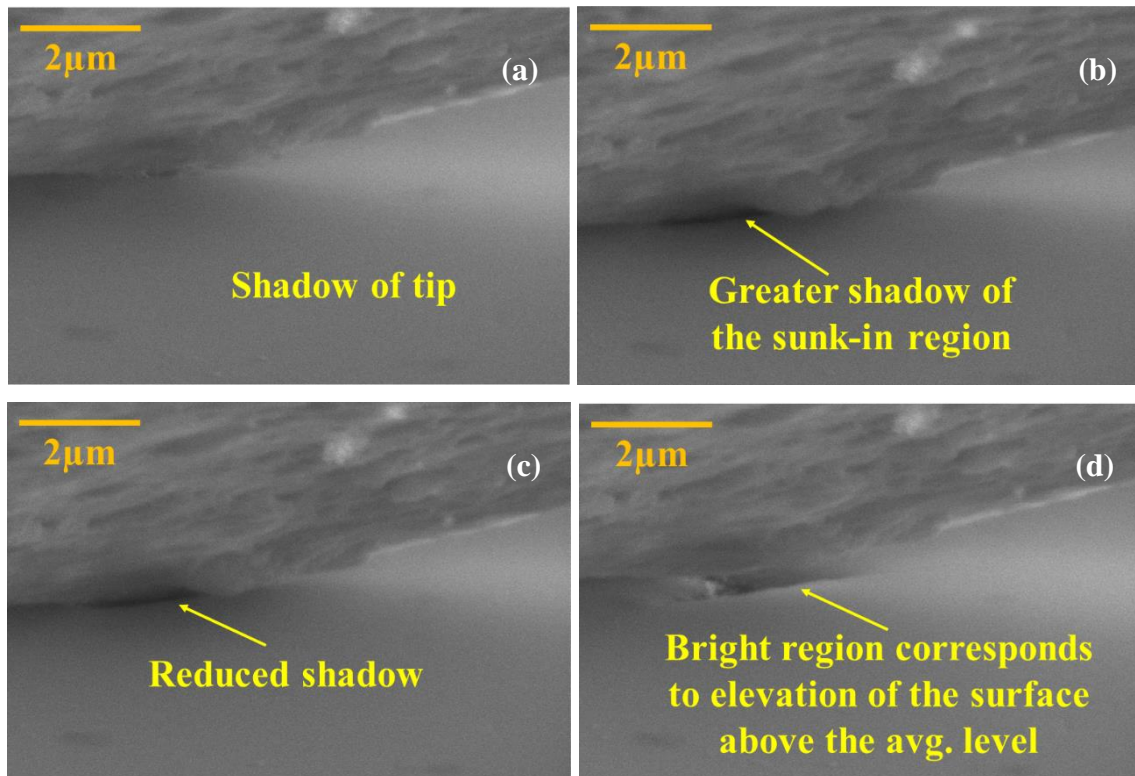


Figure 5: SEM images of indentation events (a) beginning of loading, (b) applied load up to P_m , (c) during unloading, and (d) after complete unload for PB05.

Pile-up has been reported via *in-situ* nanoindentation by other researchers [112]–[116]. In case of pliant or ductile systems – such as elastomers, pure materials, single crystals or materials at higher temperatures, examination of the *in-situ* frames suggests that often, these materials exhibit only sink-

in during loading. Visible pile-up (particularly in the recorded region, close to the tip) then occurs only during unloading. Such materials are effectively monolithic or homogeneous, and non-granular, with no preferential regions for fracture or dislocation. For such materials, explicit evidence is required to infer pile-up during loading. For composites, alloys, blends, fine-grained crystals, etc., there are interfaces within the bulk. These could be preferential regions for fracture or dislocation. For these materials, there is clear evidence of significant up-flow close to the tip surface, even during loading. However, here too, a close examination is necessary, to determine the full-load pile-up in contact with the indenter tip, h_c^{PU} , vis-à-vis the maximum pile-up, h_m^{PU} .

We continue next with the direct observation analysis by examining post-unload indentation imprint to the estimate the contact and non-contact geometry, and develop insights into the deformation pathways within the material continuum.

5.3. Post-unload nanoindentation imprint analysis

We analyze here the post-nanoindentation residual imprints acquired via SPM. In order to characterize these imprints, it is first necessary to precisely characterize the geometry of the tip. **Figure 6** illustrates a typical Berkovich tip, as it becomes blunt over usage time. As described in **Appendix D**, the bluntness is linear with usage time (measured in days) [117], $h_b = pt + q$. In our SPM examination of the responses of our indented materials, we incorporate the h_b values, corresponding to the usage day of each experiment.

Our analysis in this section consists of the following steps:

1. Based on the SPM images, we provide preliminary geometry-based estimates (in terms of the edge-imprint contact depth, h_c) of the load bearing contact area.
-

2. Then, combining the SPM image analyses with the ideal and elastic Berkovich deformation profile estimates, we provide for glassy polymers, a full load indent profile estimate and a schematic of the deformation mechanism.
3. The above steps enable estimates of the actual contact area (including contact pile-up); this overall contact area, when combined with the S determined from P - h data in [Section 5.1](#), enables definition-faithful estimates of hardness, H , and the nanoindentation modulus, E_N .

These estimates of H and E_N , provide further clues of the deformation phenomena, which are addressed in [Section 5.4](#).

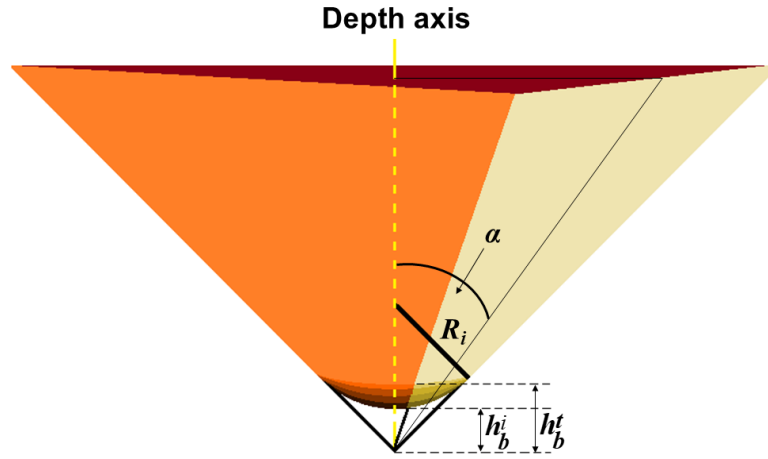


Figure 6: Schematic diagram of pyramidal Berkovich tip with bluntness. R_i is the initial tip radius, h_b^i and h_b^t are the blunt heights, initially, and after t days, respectively.

5.3.1. SPM images after indentation

Indentation loading of the surface causes it to sink-in around the indenter tip. This sink-in decays with distance from the indenter tip, where the surface ideally asymptotes to the unstressed zero-level. The sink-in depth, h_s , is thus the boundary of the contact between the material (at the material surface) and the tip. The material is in contact with the tip from h_s to h_m . We identify via SPM, the contact region for Berkovich nanoindentation of glassy polymers. [Figure 7\(a\)-\(b\)](#) are the top view and vertical section, respectively, of the residual indentation imprint ($P_m = 1000 \mu\text{N}$) on PB05,

obtained via SPM imaging. (for $P_m = 9000 \mu\text{N}$ on PB05 and for both loads on HB15, PC, and PMMA, please see [Supporting Information 4](#)). The high stress concentrations along the edges, cause instantaneous yield and a permanent imprint (invariant for 12 hours after unload) there [2], [23]. The imprint at the tip edges, indicates the limit of contact between the sample and the tip. In [Fig. 7\(a\)](#), the outermost tips of the permanent imprints, A, B and C, thus form the corners of the contact area at full load. The constant height contours are concave outwards (bowed inwards). The concave contours have been considered as measures for A_c^Δ estimates previously (i.e., $A_c^\Delta < \sqrt{3}a^2/4$) (e.g., ref. [15], [118] for PMMA). Such inferences are based on imprints available post-unload, rather than those at full load (which, in general, are not accessible).

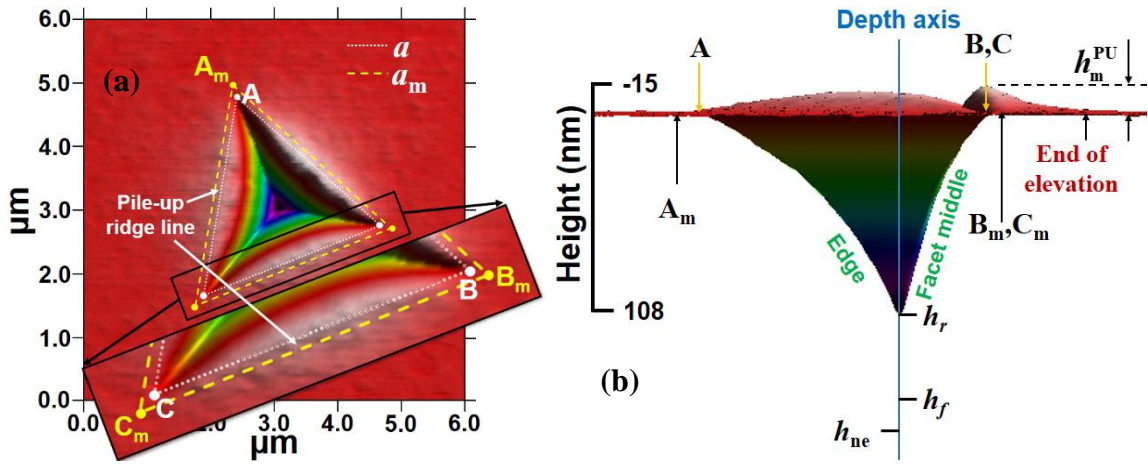


Figure 7: (a) Top view of SPM image of PB05 indicating the pile-up ridge, relative to the a -line = 2988 nm and the a_m -line = 3164 nm (b) vertical section of SPM image.

In order to unambiguously identify the actual contact profile at full load, a direct view would be most effective. In this regard, for transparent amorphous materials such as soft silicone elastomers, special arrangements [54], [119], have enabled horizontal optical views from beneath the sample and vertical views from alongside the sample, at full load during Vickers (at mm scale) and Berkovich indentations (at 50μ scale). The images indicate that the contact corners are the ends of the sharp edges of the indenter, with the in-between sides bowed inwards. The corresponding *in situ* Berkovich nanoindentation, is consistent, i.e., it indicates [113] a significantly greater sink-in along the facets

than along the edges, where the visible sink-in at the facet, begins further away from the tip surface. For such soft materials, the post-unload SPM images retain only diffused edge imprints, and there is no clear post-unload contact pile-up.

In contrast, when the elastomer is coated with Au-Pd, the *in situ* images for the harder surface, indicate a reduced sink-in along the facet at full load, along with a slight pile-up after complete unload. The stress decreases towards the middle of the facet [120]. For harder materials, this causes greater upflow along the facet middle, away from the edges, ranging from a greater recovery to an unloading pile-up ($\sim 0.8\% - 8\%$ of h_m), about the a -line (line joining the edge-imprint corners) triangle. Hence, the slight post-unload pile-up visible in our SPM images, also suggests that we could consider the a -line triangle to mark the contact boundary for glassy polymers [2], [23], [62]. This means that the inward bowed contours correspond to greater vertical displacement recovery away from the edges [89]. The edge regions, and specifically, the apex, undergo greater permanent deformation due to stress concentration (decrease in stress along the facet, increases elastic contribution to the deformation there). Thus, the apex exhibits the maximum residual deformation. Hence, the vertical sections (Fig 7(b)) have convex-upwards profiles, along both, the edge as well as the facet middle; i.e., fractional upward recovery increases with radial distance from the apex.

Based on the above, we recognize that the contact region which corresponds to the imprint of the edges; this is the contact depth at full load for Berkovich- nanoindentation, h_c , with contact area, $A_c^\Delta(h_c) \approx 24.5 \times (h_c + h_b)^2$ for ΔABC ([27], [55]–[61]). We find from our calculations that for all our samples, the residual imprint area (A_c^Δ) is always greater than the quartz-calibrated area (A_c^Q) (Table 4) due to upflow, which reduces the sink-in.

For ideal Berkovich geometry, the triangular geometry of the horizontal projection of the imprint, indicates that the geometric contact height, $h_c^\Delta = h_c + h_b = a / (2\sqrt{3} \tan \alpha)$. The projection based

maximum depth, $h_m^\Delta = h_m + h_b$. In addition to the polymers exhibiting a greater than OP contact depth, h_c^Δ , one consistent observation is that at the end of the hold period over the P_m range, $h_c^\Delta \propto h_m^\Delta$. The ratio, $\kappa = h_c^\Delta / h_m^\Delta$, does not change even as loading time (and thus P_m) increases. This suggests that κ is independent of loading time and the time-dependent VE effects. The κ values for the various polymers (in increasing order) are ~ 0.92 (HB15), ~ 0.94 (PMMA), ~ 0.95 (PB05), ~ 0.96 (PC) (Fig. 8). For HB15, κ varies slightly from ~ 0.86 to ~ 0.92 , over the P_m range in this work. For glassy polymers, $(h_f/h_m) \sim 0.6$, which satisfies the requirement for the OP method validity ($(h_f/h_m) < 0.7$). Thus the OP method significantly overestimates h_s , indicating that the (h_f/h_m) criterion is not sufficient, and additional phenomena need to be recognized. Similar to our findings, one simulation [42] has predicted that for PMMA, low sink-in and linear depth contours are a consequence of fitting the P - h data. That work has implemented the phenomenological quadratic constitutive parameters which relate load to displacement [121], [122].

Table 4: A_c^Δ values from imprint vs A_c^Q from OP tip area calibration on Quartz Standard.

P_m (μN)	A_c values (μm^2)	PB05	HB15	PC	PMMA
1000	A_c^Q	3.34 ± 0.03	3.44 ± 0.03	5.56 ± 0.10	4.18 ± 0.18
	A_c^Δ	3.85 ± 0.02	3.50 ± 0.01	7.11 ± 0.12	4.89 ± 0.08
9000	A_c^Q	32.35 ± 0.59	32.22 ± 0.38	62.48 ± 1.25	42.96 ± 0.64
	A_c^Δ	43.68 ± 0.19	40.35 ± 0.23	75.96 ± 1.16	51.86 ± 0.29

The polymers considered here are compliant materials; i.e., their respective elastic moduli, lie in the range 2 GPa – 3 GPa [73], [74], [123]–[126]. The Poisson's ratios for these polymers are in the range 0.34 (SU-8) [127] to 0.39 (PMMA) [67]. In contrast, the OP materials have moduli in the range 68 GPa (aluminum) to 440 GPa (sapphire) [2]. The Poisson's ratios are in the range 0.08 (quartz) to 0.34 (aluminum). The greater compliance of the polymers, enables greater displacement, in the implemented P_m range. The greater penetration could decrease the bulk volume. This volume

reduction is resisted, because of the greater Poisson's ratio, causing a greater upflow close to the indenter tip. This upflow causes a greater h_c^Δ (and κ), i.e., a significantly reduced sink-in. Hence, the high, and broadly invariant values of κ , are because of volume conservation effects.

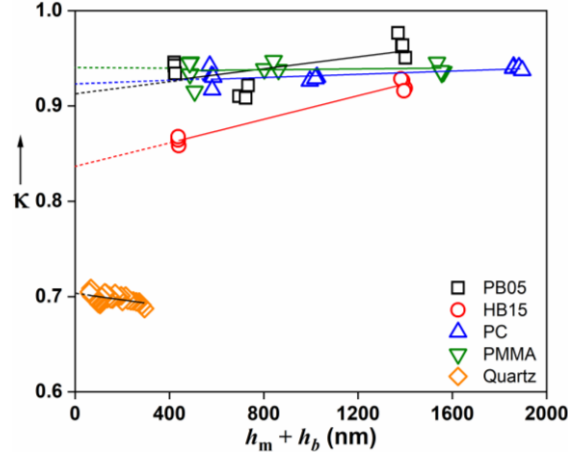


Figure 8: Contact depth fraction, κ vs effective maximum depth, $(h_m + h_b)$. κ is almost constant over the entire depth range for a quartz and the polymers. For HB15, κ varies slightly.

In contrast to the invariant imprint from the Berkovich edges, the SPM images indicate that the tip apex is at depth, $h_r < h_f$. This is because SPM imaging is completed in ~ 6 min after complete unload, during which, VE recovery occurs (e.g., see [81], [83], [84], [87]). This recovery has been observed to continue even after 12 hrs. **Figure 7(b)** indicates all the three levels, h_r , h_f and h_{ne2} .

We will consider these phenomena in greater detail in **Section 5.3.2**.

In **Fig. 7(a)-(b)**, the a_m -line corresponds to the tip cross-section at P_m , at the same level as the surface. For PB05, there is sink-in (**Fig. 5**) at P_m . Hence, the open sample surface at the a_m -line, is below that cross-section of the tip. As mentioned above, every glassy polymer sample also exhibited a small pile-up, that begins inside the a -line, and continues past the a_m -line.

Also, we note that the maximum pile-up, h_m^{PU} , in the facet direction, is located beyond the geometry-based contact radius (a -line). This is not clear in **Fig. 7(a) – (b)**, but is visible under a greater

magnification of Fig. 7(a) (See Supporting Information 4). In addition, in order to maintain the continuity in the contact displacement and its derivatives at the contact boundary (displacement decreasing with respect to radial distance), the maximum pile-up, *prima facie*, is likely to be radially further away than at geometric contact. This becomes unambiguous after we remove VE effects of recovery creep, as addressed in detail in Section 5.3.2. Also, we observe in previous researchers' [112]–[116] *in-situ* nanoindentation pile-up frames, that the maximum height of piled-up material, always appears to be away from the tip surface, and out of contact (seen previously for PEEK, [79]).

The key features in case of glassy polymer nanoindentation, identified by SPM, are:

- a) *in situ* nanoindentation indicates that pile-up is only during unloading
- b) the contact and sink-in along the edges is clear and unambiguous
- c) the contact fraction is significantly greater than in the case of OP materials,
- d) the post-unload SPM images indicate simultaneous sink-in and pile-up and
- e) the maximum pile-up, is likely to be radially further away than at geometric contact

Accounting for this combined set of observations, we estimate next the deformation profile at full load, which will enable an understanding of the material response during nanoindentation.

5.3.2. Deformation Profile during Berkovich Nanoindentation

We estimate the deformation profile for glassy polymers via two steps.

- (i) We first propose a schematic for the response of an ideal elastic solid to ideal Berkovich nanoindentation, based on the previously proposed schematic [128] for ideal conical indentation.
 - (ii) Considering the SPM-imaged surface topology, we then extend the elastic nanoindentation framework, to understand the response of amorphous VEP glassy polymers; we estimate the surface topology at full load to obtain the deformation profile, including the contact pile-up, h_c^{PU} .
-

I. Ideal elastic nanoindentation by an ideal Berkovich tip

In the LS analysis of the response of a purely elastic material, the Berkovich indenter is considered to be an equivalent *cone* with half-angle 70.23° . For a perfect conical indenter with a circular cross-section, this LS analysis has determined $h_s/h_m = (\pi - 2)/\pi$. The basic premise of this analysis is that deformation is localized under the indenter tip, and the compressive displacement is vertically downward, with lateral Poisson widening, into the surrounding material. The deformation pathways have been determined previously [129], [130].

For actual Berkovich indentation, we propose to progress beyond the equivalent cone. A Berkovich tip possesses sharp edges and flat sides, and not a curved surface. Previously [54], [119], in estimating the OP sink-in for elastomers, two cones were implicitly considered with half angles, $\theta = 77.03^\circ$ on the edge side, and $\theta = 65.27^\circ$ along the facet middle (although $h_{s,edge} < h_{s,facet}$).

In section 5.3.1, we have found that for glassy polymers, the baseline sink-in is uniform around the tip. At this stage, our objective is to find easily useable equations for the final form (and not a fundamental behavior-describing equation). Hence, in this work, we generalize the half-angle variation, all about the Berkovich indenter, and consider it qualitatively for ideal Berkovich indentation of an elastic material; i.e., we consider a Berkovich indenter to be a system of continuously varying cones, with half-angle $\theta = 77.03^\circ$ in the edge direction, decreasing to $\theta = 65.27^\circ$ in the facet middle direction. There is a corresponding variation in the contact radius.

Figure 9 illustrates the response of a purely elastic medium to indentation in terms of this varying cone interpretation of the Berkovich tip. The difference between the *equivalent* cones and an actual Berkovich tip, is that the Berkovich surfaces of the varying cones, are not uniformly circular; they vary from being a sharp edge surface to a flat facet surface. In our model-free development, this variation would not affect the final mapping to the empirically observed surface. This cone-family

framework retains the required conditions that for the indented surface topology, that the contact boundary, exhibits continuity with radial distance, in the displacement and its derivatives. This makes the resultant surface topology estimate, an objective and a functional approximation. It is depicted in [Fig. 9](#), which is the previously [129], [130] reported conical indentation schematic, adapted for Berkovich indentation, as described above.

The contact radius in the edge direction, $a_{c,ed} = a/\sqrt{3}$ and along the facet-middle direction, $a_{c,fa} = a/2\sqrt{3}$. According to the LS analyses (r is the radial distance from the tip apex), the non-contact radial (inward) (see [Supporting Information 5](#)) and axial (downward) displacements (i.e., sink-in profile, $h_s^p(r)$) are:

$$\text{Radial shift}|_{z=0, r>a_c} = -\frac{1-2\nu}{4(1-\nu)} \frac{a_c^2 \cot \theta}{r} \quad \text{eqn. 5}$$

$$h_s^p(r) = \cot \theta \left[a_c \sin^{-1} \left(\frac{a_c}{r} \right) + \sqrt{r^2 - a_c^2} - r \right] \quad \text{eqn. 6}$$

As indentation progresses, A_c increases, with a corresponding (but less than proportionate) increase in the sink-in as well. As illustrated in [Fig. 9](#), the radial and axial displacements (see [Supporting Information 5](#)) occur until the surface touches the tip, following which, only axial displacement occurs. Eqn. 7 is the resultant expression for inward radial deformation in the contact region, with respect to the instantaneous contact radius, and the downward axial deformation follows the surface of the varying cones of the Berkovich tip.

$$\text{Radial shift}|_{z=0, r<a_c} = \frac{1-2\nu}{4(1-\nu)} r \cot \theta \left[\ln \left(\frac{r/a_c}{1 + \sqrt{1 - (r/a_c)^2}} \right) - \frac{1 - \sqrt{1 - (r/a_c)^2}}{(r/a_c)^2} \right] \quad \text{eqn. 7}$$

This development for the nanoindentation of an ideal elastic material by an ideal Berkovich tip, is extended next, to the real Berkovich nanoindentation of glassy polymers (compliant VEP materials).

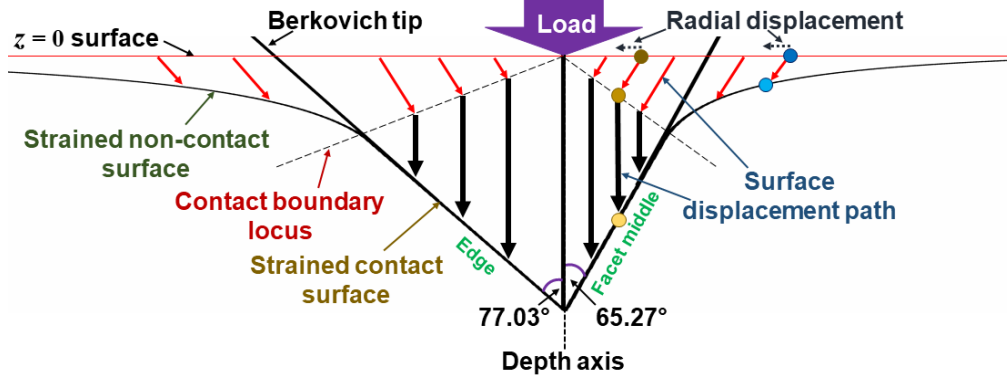


Figure 9: Schematic diagram of displacement paths of surface elements of the elastic medium when it is indented with a perfect Berkovich tip. For $a_c > r$, the radial displacements are shown in different shades of yellow; for $a_c < r$, they are depicted in different shades of blue. This is our Berkovich indentation adaptation of the previously reported schematic for conical indentation [129], [130].

II. Berkovich indenter deformation of glassy polymers

We estimate here the surface topology of amorphous glassy polymers undergoing real Berkovich indentation. We do so by superimposing the pile-up and sink-in (geometric) data obtained via SPM imaging, onto the ideal Berkovich deformation of an ideal elastic solid (eqns. 5-7, Fig. 9).

Figure 5 clearly indicates that for PB05, only sink-in occurs during loading, and surface elevation occurs at the end of unloading. In this case, the difference in the sink-ins (between the edge and the middle of the facet) would be the contact pile-up, h_c^{PU} , i.e., the full-load contact portion of the measured pile-up. To estimate h_c^{PU} , we begin with the measured pile-up, i.e., the maximum pile-up height, h_m^{PU} , at zero load. We find that for various glassy polymers, there is such a pile-up along the facet, to varying degrees (see Supporting Information 4). This pile-up effect is analyzed appropriately to add the h_c^{PU} contribution to the SPM-based A_c^Δ .

As per Table 5,

- a) For PB05, HB15 and PMMA, $h_m^{\text{PU}}/h_s^{\Delta} < 1.0$. For PC, $h_m^{\text{PU}}/h_s^{\Delta} \geq 1.0$ (consistent with PC exhibiting the highest κ); i.e., pile-up for PC might have begun during loading.
- b) $h_m^{\text{PU}}/h_s^{\Delta}$ is greater for PB05 than for HB15, and for PC than for PMMA.

To estimate the *contact* pile-up, h_c^{PU} , we analyze the SPM-imaged topology data in some detail; i.e., we need to consider VE effects between full load, elastic unload and imaging.

Table 5: $h_m^{\text{PU}}/h_s^{\Delta}$ for all samples for $P_m = 1000 \mu\text{N}$ and $P_m = 9000 \mu\text{N}$.

P_m (μN)	PB05	HB15	PC	PMMA
1000	0.540 ± 0.075	0.095 ± 0.004	1.106 ± 0.083	0.515 ± 0.065
9000	0.854 ± 0.102	0.245 ± 0.019	1.096 ± 0.032	0.416 ± 0.031

Viscoelastic recovery from indentation

We recall from 5.3.1, that $h_r < h_f < h_{\text{ne}2}$; h_r is the depth recorded by SPM imaging, and $h_{\text{ne}2}$ is an estimate of the depth after elastic recovery. We also recall that all recovery is vertically upward. An analogous situation exists in the case of the maximum pile-up. Although the a -values (corresponding to permanent plastic deformation) are invariant with VE effects, the residual depth and pile-up profiles, rise upwards over time; i.e., h_r decreases and h^{PU} increases (see [Supporting Information 6](#)). Considering this, we estimate next, the deformation at P_m , in terms of the contact pile-up on the facet side. We do so in two steps. First, we recognize that the pile-up is due to the full load contact, and can be represented as the surface profile at $P = 0$, after the removal of VE effects. Hence, in the second step, we determine the contact pile-up by intersecting the estimated zero-load pile-up profile with the location of the indenter tip surface, for a hypothetical full contact displacement, h_c (without any sink-in). To obtain the full load deformation profile, we sink this h_c profile by the full load elastic sink-in profile. We elaborate on these steps below.

(i) Removal of VE Effects: VE effects cause the tip apex imprint to rise with time, (i) from the hypothetical h_{ne0} or h_{ne2} , to the experimental h_f (at the end of the load removal, where the last 30% of the unload is at a decelerating rate), and (ii) from h_f to the imaged h_r (during unloading and ~6min hold for the SPM). Similarly, the SPM measured $h^{PU} (=h_m^{PU})$ contains time-dependent VE effects, prior to which, the elastic-recovery-based $h^{PU} (=h_{ne2}^{PU})$ is likely to be lower. Such behavior is consistent with that observed by earlier researchers [81], [83], [84], [87]. Hence, to estimate h_c^{PU} , from h_m^{PU} , we progress to the hypothetical pile-up, h_{ne2}^{PU} , corresponding to the rapid elastic recovery. Therefore, we first develop quantitative estimates of the time-dependent recovery observed via SPM. We obtain 2 consecutive SPM profiles (~ 9 min apart), immediately following rapidly unloaded indentations on HB15 and PC (Appendix E). For $r > a_c$, at times t_1 and t_2 , they satisfy $\frac{h_{r1}^{p,PU}(r)}{h_{r2}^{p,PU}(r)} \approx \frac{(h_c - h_{r1})}{(h_c - h_{r2})}$; then $\frac{h_{ne2}^{p,PU}(r)}{h_r^{p,PU}(r)} \approx \frac{(h_c - h_{ne2})}{(h_c - h_r)}$. This geometry-based profile estimate, $h_{ne2}^{p,PU}(r)$ (at the instant of hypothetical recovery to h_{ne2}), then helps estimate h_c^{PU} .

We have considered h_{ne2}^{PU} , instead of estimating pile-up at h_{ne0} , which we have estimated to correspond to VE-free unloading. We recall that the very small fitting range for h_{ne0} , would make its estimate qualitative. For quantitative measures, examination of a reasonable fraction of the unloading, is necessary to model the unloading step. We consider the entire constant rate region, as the required reasonable fraction. In addition, $(h_c - h_{ne0}) < (h_c - h_{ne2})$. Thus, the resultant reduction estimate, $(h_m^{PU} - h_c^{PU})$, is slightly more conservative, and hence, more appropriate, in recognizing the uncertainties in this approach.

(ii) Intersecting surface topology estimate with indenter tip profile: In order to estimate h_c^{PU} (Fig. 10(a)-(b)), we note that the recovery of the non-contact region is fully elastic. On full

unload, the LS- z (elastic) profile recovers so as to reach $z = 0$ uniformly, for all r . For glassy polymers, elastic recovery of the apex region, is up to h_{ne2} . At elastic recovery to zero load, the sunk surface contact would rise by h_s , resulting in zero displacement along the edge-line for $r > a_c$ and a pile-up along the facet. Hence, we construct a full contact profile at displacement h_c , so that the full load sunk-in edge-line, has zero displacement for $r > a_c$; this is also the profile at zero load. In the absence of pile-up, even the sunk-in facet middle line would have zero displacement for $r > a_c$, at both, zero load and for the full contact profile at displacement h_c . The pile-up profile along the facet then, also corresponds to that at zero load, and to when the full contact displacement is h_c ; the extension of the contact line on the facet middle meets the pile-up profile, $h_{ne2}^{p,PU}(r)$. Thus, h_c^{PU} corresponds to this intersection of the $h_{ne2}^{p,PU}(r)$ profile estimated above for $r > a_c$, with a line along the surface of the imaginary indenter tip (for the facet middle, slope=cot 65.27°), rising from the z -axis at $h_c^\Delta = h_m^\Delta - h_s^\Delta$. Here, we consistently find that h_{ne2}^{PU} is beyond the geometric contact for contact displacement h_c^Δ , making the contact pile-up, $h_c^{PU} < h_{ne2}^{PU}$. We note that the actual contact at h_c^{PU} would follow a smoother curve, to enable at the contact boundary, continuity in the displacement and its derivatives with radial distance.

As depicted in the estimated profile in Fig. 11(a)-(b), the LS analyses provide eqn. 6 (the LS- z equation), to compute the downward non-contact displacement as function of the radial distance. We recall that for a given h_s , the purely elastic maximum penetration of an ideal conical indenter is $h_e = h_s [\pi/(\pi-2)]$. Therefore, we consider the sink-in z - r relationships for our experiment, to correspond to radially outward-shifted z - r relationships (i.e., by outward shifting of the z -axes) for the cones of depth h_e , such that the shifted h_e cones share the surface lines with the experiment cones. We propose this relationship for the edge direction. At this time, in the absence of a physics-

based profile development, which accounts for all the events identified in this section, we employ this shift-based profile. This concept ensures that at the contact boundary, there is a continuity in the displacement and its derivatives (with respect to radial distance), as built into the available eqns. 5 - 7. These profiles are also similar to those reported via FEA [54], [113] as well as via optically recorded video frames of PDMS indentation [119], [129], [131].

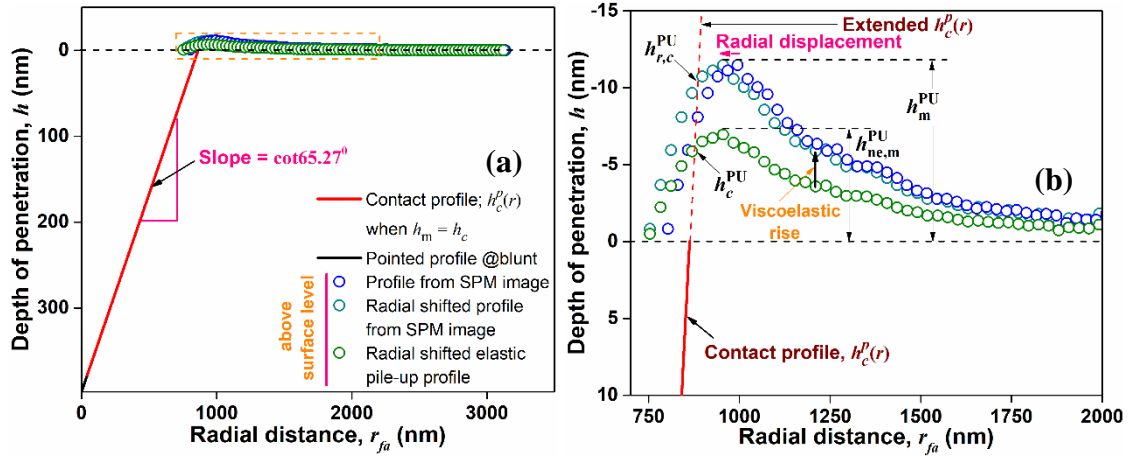


Figure 10: (a) Full indentation profile at full load, (b) magnified indentation profile toward facet middle side for one indentation of PB05 for $P_m = 1000 \mu\text{N}$. Note that h_{ne2}^{PU} the maximum pile-up, corrected for VE effects, is beyond geometric contact. Hence $h_c^{PU} < h_{ne2}^{PU}$. The actual profile would be smoothened to exhibit continuity at contact, in displacement and its derivatives with respect to radial distance.

For the facet direction, we employ the LS- z equation, and superimpose the estimated contact pile-up profile (Fig. 10(b)). Therefore, to estimate the pile-up on the facet, we consider the shifted, elastic deformation-based LS- z equation, on which we superimpose the $h_{ne2}^{p,PU}(r)$ profile (Fig. 11(b)).

Figure 11 is a rational estimate of the likely surface topology at P_m , which, if superimposed on VE recovery, would yield the zero-load profile, that we obtain via SPM imaging. The case for HB15 (polymer with minimum pile-up) is depicted here. The maximum pile-up observed in our work is with PC, whose estimated profiles are provided in Appendix F.

The resultant profiles are similar to those suggested previously (e.g., [43], [86], [132], [133]). In this regard, one report [27] considers tip bluntness as well as sink-in or pile-up. Their schematic clearly indicates that $h_c^{\text{PU}} < h_m^{\text{PU}}$, and is based on the intersection of the facet side surface topography with the indenter tip boundary. Their work then reports the best match FEA parameters for effective conical indentation ($\theta = 70.23^\circ$), leading to the corresponding A_c . Thus, our surface profile estimate via minimal modifications of the currently available equations, is likely to be similar to the real profile. Then the estimated profiles in Fig. 10 and Fig. 11, provide a basis for further analysis.

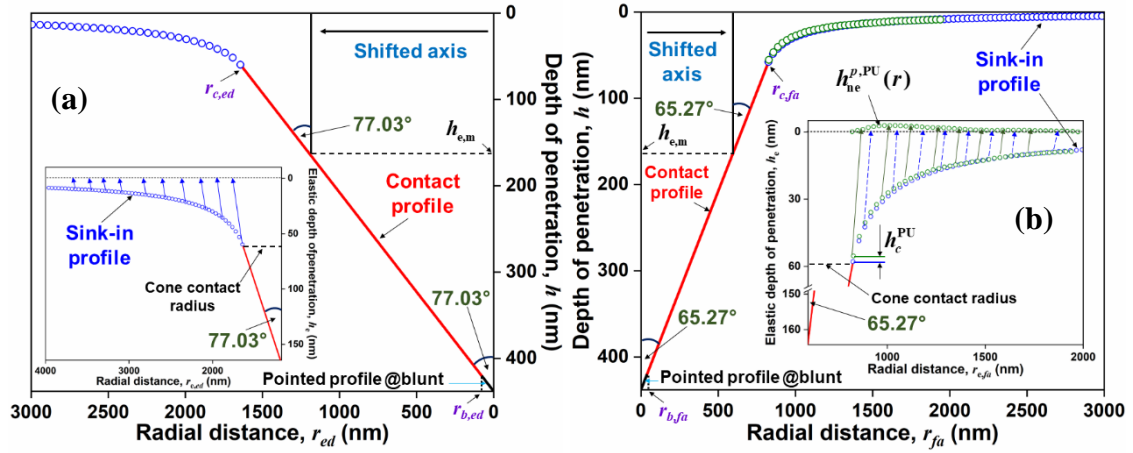


Figure 11: Deformation profile for HB15 at full load (a) edge side, (b) facet middle side.

Pile-up causes the contact area to be greater than the imprint or sink-in based estimates, A_c^Δ [9]–[20]. The geometry-based calculation for the additional contact area for A_c , is provided in Appendix G. Errors in estimating A_c due to tilt between the indenter tip and the indented surface [134], have been addressed in Supporting Information 6.

We note that additional area due to pile-up (comparing Table 5 with Table S.6.1 in Supporting Information 6), increases A_c for HB15 and PMMA by $\sim 0.3\%$ (h_c^{PU} basis) to $\sim 2\%$ (h_m^{PU} basis). For PB05 and PC, the respective additional pile-up areas are $\sim 2\%$ and 8% . Thus

$$\left(A_c(h_m^{\text{PU}}) - A_c(h_c^{\text{PU}}) \right) < \left(A_c(\text{Loubet}) - A_c(\text{OP}) \right); \text{ i.e., the choice of the parameters (between } h_c^{\text{PU}}$$

and h_m^{PU}) itself affects only slightly, the subsequent analyses for glassy polymers. However, the framework which considers h_c^{PU} , provides an objective platform for future development. Based on the SPM imaging as well its consequent analysis in this section, we propose next, a schematic of the deformation phenomena – in terms of the profiles and the paths.

5.3.3. Berkovich nanoindentation mechanism of glassy polymers

In this section, we propose for amorphous glassy polymers, a qualitative schematic of the nanoindentation profile as well as of the deformation mechanism (pathways) in the material, based on the experimental data discussed and analyzed in [sections 5.3.1](#) and [5.3.2](#). The proposed schematic at full load is depicted in [Fig. 12\(a\)-\(b\)](#).

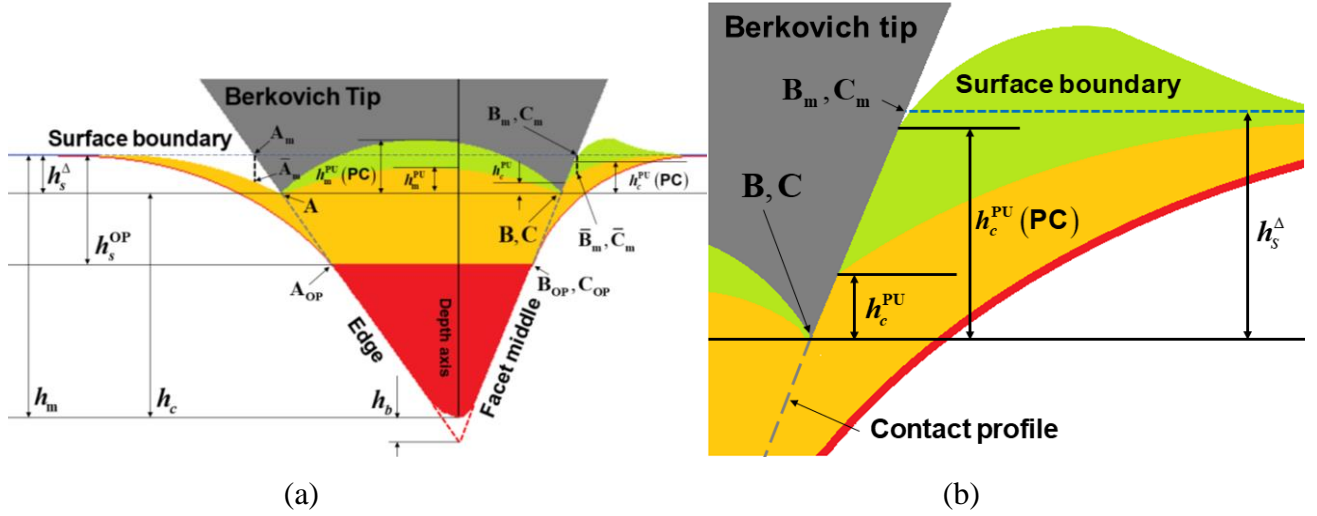


Figure 12: (a) Schematic diagram of the deformation profile at h_m (and P_m). (b) magnified contact pile-up at h_m (or P_m) vis-à-vis the OP estimate (Red Curve), close to the zero level.

As described above in [Section 5.3.1](#), the contact corners are A, B, C. The corners for indentation depth h_m^Δ , are A_m , B_m and C_m , on the tip edges, at the level of the surface, outside contact, but within the sink-in region. The sample surface has sunk in, such that the sample surface triangle $\bar{A}_m\bar{B}_m\bar{C}_m$ corresponding to the a_m -line at full load, lies beneath the corresponding section

$A_m B_m C_m$ of the indenter tip. The elastic sink-in as per the OP or LS method, would have occurred up to A_{OP} , B_{OP} and C_{OP} (i.e., $h_s^{LS} \sim h_s^{OP}$). A reduction in the sink-in makes ABC the contact region. For most polymers, pile-up occurs only during unloading, and thus the reduced sink-in is below the surface level at full load (yellow region). Table 5 indicates that pile-up for PC might have occurred during loading as well, as represented by the green zone. We discuss here, the causes of this reduced sink-in, and extend the discussion to pile-up, which would correspond to the upward-bulging yellow and green contact regions on the facets, above the ABC (h_c^Δ) level in Fig. 12(a)-(b). This is consistent with the outward-bowed contours beyond the a -lines, in Fig. 7(a). In section 5.3.2, they have been identified as the locus of contact pile-up heights, along the facet. These are discussed next.

We have discussed in section 5.3.1, that elastomer nanoindentation images indicate [54] elastic sink-in along the facet. We suggest that this is because the soft surrounding material can absorb well, the compression due to the lateral Poisson widening below the indenter tip. Poisson expansion and upflow might have possibly occurred over a wider area, beyond the recorded region. Along the facet, the stresses are lower, since the indenting surface is flat. Hence, in case of glassy polymers, the least resistance to upward flow is at the middle of the facet, and results in a maximum elevation of the contact surface on the facet. The consequence of the reduced stress effects, is that the contact boundary is an arc, between the edges, across the facet. This greater upflow, closer to the tip surface, leads to a greater h_c along the tip facet. Analogous phenomena have also been proposed previously [43], [86], [132], [133].

During indentation, the downward compression by the angled surface of the Berkovich indenter, gives rise to graded lateral Poisson expansion, that resists volume change. The lateral flow due to Poisson deformation is directed radially away from the tip initially, towards the hard, undeformed region surrounding the indenter tip. The outer region would need to undergo lateral compression to

accommodate the compression-induced lateral expansion of the inner regions below the tip. Unlike in the case of uniaxial compression, the open vertical surface (laterally directed surface normal) is far from the deformation. This tendency toward graded lateral compression leads to vertical upward expansion, towards the free upper surface (vertically upwards directed surface normal), which is closer, and can accommodate this deformation more easily. Along the edges, stress concentrations, cause the greatest downward compressive stresses. These result in the lowest extents of upward flow there. Hence, for our materials, this upward flow at the edges, remains within the zero-level boundary (no pile-up), and only causes reduction in h_s .

We recognize that in competition to the upflow, as the tip moves downward during loading, downward yield flow occurs immediately, particularly along the edge. Thus, corresponding to the downward compressive stress at the interface, and consistent with the downward movement of the angled surface (of a conical or Berkovich tip), the layer of the solid *wetting* the tip surface moves downward, along with the tip (Fig. 13). The frictionless surface usually considered for purely compressing flat surfaces as in flat-punch tip or macroscopic compression plates, is to enable lateral volume-conserving, Poisson widening. The downward compressive forces being normal to the widening direction, prevent only upward slip (upward flow at the contact with the tip). There would be no effect of contact friction for lateral widening, since contact with the angled tip ceases, the instant the material moves laterally, however slightly.

Therefore, in the case of Berkovich indentation, the previous FEA-based suggestions of friction effects between the tip surface and the indented material (e.g., [44], [50], [53]), need to be re-examined. Consistent with our postulates, friction has been found to be inconsequential in some reports [38], [42], [45], or effective only if pile-up is significant [48], [51]. Hence, as opposed to friction, the resistance to lateral widening arises only from the hard, surrounding material, via resistance to its own lateral compression. This gives rise to vertical upflow, some radial distance

away from the indenter tip surface (Fig. 13), along the path of least resistance. The indicated downward and inward flows at the top, represent eqns. 5 – 7, caused by the downward pull of the tip.

The consequence is that the maximum pile-up is radially away from the geometric contact distance, and that the pile-up measured via SPM has undergone post-unload increment, due to VE effects. This is in contrast to FEA reported earlier (e.g., [50], [53]), where the maximum pile-up is in contact with the indenter tip. We explain this by noting that both, the upflow as well as the downward tip drag, dissipate with radial distance. This combination pushes the location of maximum upflow, h_m^{PU} , to beyond the corresponding tip radius; then the contact pile-up, $h_c^{PU} < h_m^{PU}$. This result is illustrated in the schematic of the indenter and the region of the pile-up (Fig. 13)

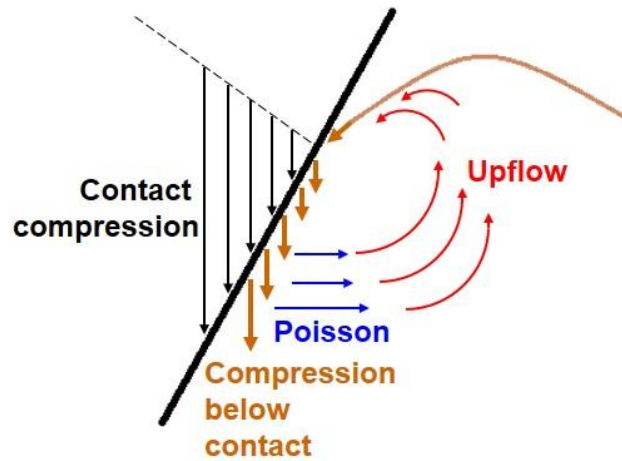


Figure 13: Schematic of transformation of lateral Poisson deformation into upflow.

To describe a material's nanoindentation via FEA, it is important to incorporate the physical phenomena as inferred via the indentation data as well as observables such as topology. A careful analysis of the phenomena is necessary to incorporate “user described” material properties. The current work identifies various phenomena which could be inputs to FEA, which in turn, would yield further insights. Our subsequent analyses (Section 5.4), builds on the idea of considering and accounting for additional phenomena, taking clues from the definition-faithful estimates of the nanoindentation properties in Section 5.3.4.

5.3.4 Nanoindentation properties: E_r and H

In order to acquire further clues on the nanoindentation phenomena we list in Table 6, our estimates of the nanoindentation properties for glassy polymers, as conventionally defined for EP materials, i.e., $E_r \times (1 - \nu^2) \sim E_N \approx (S/\sqrt{A_c})(1 - \nu^2)\sqrt{\pi}/2$ (since the indenter compliance is negligible) and $H = P_m/A_c \cdot S$ (Section 5.1.2) and A_c (Section 5.3.2) have been determined above.

As mentioned briefly for S in Section 5.1.2, one intuitively expects that E_r and H , to increase with crosslinking. While several literature-reported trends from simulation (e.g., [135]) and bulk measurements of modulus (e.g., [136]–[140]), are consistent with this intuitive trend, there are contrary reports as well [141]–[143]. We find that on increasing the degree of crosslinking from the less cross-linked PB05 and almost fully cross-linked HB15, the definition-faithful estimates of S and E_r increase with crosslinking. Similarly, H also increases with cross-linking. For PMMA and PC, following the trends for the uniaxial moduli (see [25], [67], [73], [123]–[126]), our definition-based estimates of E_r and H for PC, are lower than those for PMMA.

Table 6: Nanoindentation properties for $P_m = 1000 \mu\text{N}$ and $P_m = 9000 \mu\text{N}$.

Property	P_m (μN)	PB05	HB15	PC	PMMA
E_r (GPa)	1000	4.58 ± 0.04	5.05 ± 0.04	3.05 ± 0.04	4.38 ± 0.01
	9000	3.96 ± 0.03	4.68 ± 0.03	2.69 ± 0.02	3.81 ± 0.03
H (MPa)	1000	237.7 ± 1.2	267.1 ± 0.3	120.7 ± 2.9	163.0 ± 2.5
	9000	191.1 ± 2.8	213.5 ± 3.1	105.1 ± 1.1	150.3 ± 2.2
E_N/E	1000	N.A.	1.9	1.2	1.4
	9000	N.A.	1.7	1.1	1.2
H/σ_y	1000	N.A.	2.8	1.7	1.4
	9000	N.A.	2.3	1.5	1.3

We have also estimated the E_r and H , following various methods proposed by previous researchers [2], [14], [15], [19], [62], [69], [71], [72] (Fig. 14; methods and values are listed in Supporting Information 7). Figure 14 indicates that the nanoindentation properties of the polymers

examined in this work, estimated employing previous methods, can deviate up to $\sim 50\%$ from our estimates.

For PMMA and PC, all methods yield the expected trend of lower E_r and H values for PC, compared to those for PMMA. In case of literature methods for SU-8, only methods where S is obtained by fitting h vs P relationships [71], [72], and only to our nanoindentation data at $P_m = 9000 \mu\text{N}$, indicate an increase in E_r with crosslinking. Methods that consider higher estimates of A_c , such as via residual imprint [62] or by adding the h_m^{PU} (maximum pile-up) effect to A_m^{Δ} (considering the full tip in contact, with $h_s=0$) [19], [20], yield the similar trends in H .

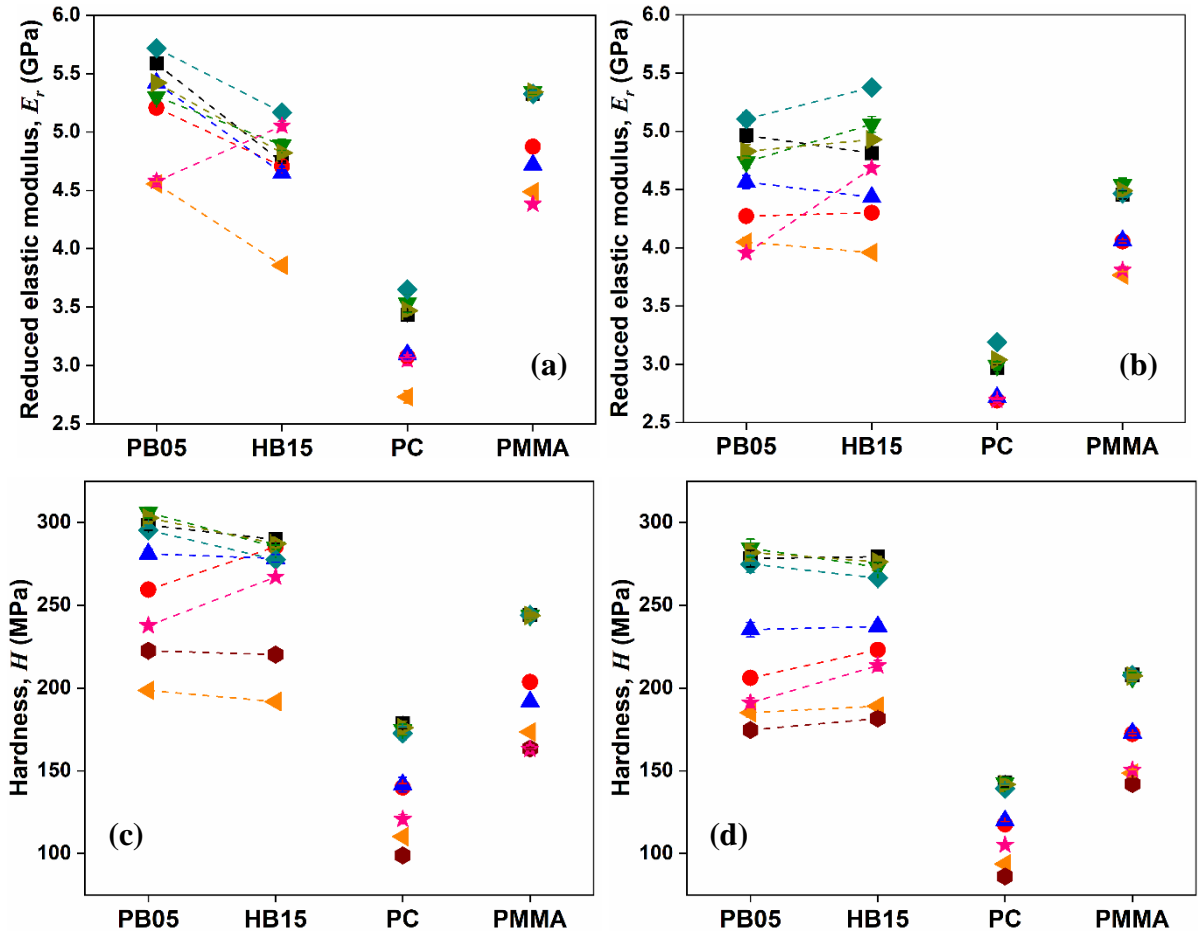


Figure 14: E_r values for (a) $P_m = 1000 \mu\text{N}$, and (b) $P_m = 9000 \mu\text{N}$ and H values for (c) $P_m = 1000 \mu\text{N}$, and (d) $P_m = 9000 \mu\text{N}$. Here, \blacksquare [2], \bullet [62], \blacktriangle [14], \blacktriangledown [72], \blacklozenge [71], \blacktriangleleft [15], \blacktriangleright [69], \blacklozenge [19], [20], and \star Our data.

Next, we consider uniaxial compression properties, at the equivalent uniaxial strain rate, $\dot{\varepsilon} = c\dot{h}/h = 0.5c\dot{P}/P \sim 0.0045/s$. $c \sim 0.09$ [73], [78], [144] correlates the notional nanoindentation strain rate, $\dot{\varepsilon}_N \sim \dot{h}/h$, to the uniaxial strain rate. At this strain rate, σ_y values estimated by interpolating the literature data are ~ 93 MPa for HB15 (from [73], [74]), ~ 66 MPa for PC (from [125], [126]), ~ 120 MPa for PMMA (from [123], [124]). Similarly, the respective E values are ~ 2.2 GPa for HB15, ~ 2.4 GPa for PC and ~ 2.7 GPa for PMMA. Partially crosslinked SU-8 (PB05) is not easily amenable to form micropillars because micropillars are formed by washing away soluble, uncrosslinked material [73], [74].

The nanoindentation properties of glassy polymers, as conventionally defined, are significantly different from those obtained by uniaxial deformation testing (last two rows of Table 6). For a broad range of EP materials [145], $E_N \sim E$ and $H \sim 3\sigma_y$. In our experiments, we find that $E_N > E$ and $\sigma_y < H \leq 3\sigma_y$. Thus, for glassy polymers, there is a dichotomy in the trends between the two metrics of nanoindentation deformation, with respect to the corresponding uniaxial deformation properties.

For E_N only, corrections have been suggested; e.g., Tranchida *et al.* [24], have introduced a phenomenological correction factor, $\chi = E_N/E$, to account for the significant deviation of E_N from E . In this understanding, we need to know *a priori*, the E values, corresponding to the stress-strain curve of the bulk material. This deviation of E_N has been accounted for by Mokhtari *et al.* [146], by equating S to the slope at 42% of P_m , for $P_m = 100$ mN.

We explore if the underlying deformation phenomena in polymers can be understood through our definition-faithful property estimates. The deformation schematic of Fig. 13 (which is based on the SPM profiles), indicates that the high compliance induces greater volume-conserving upflow, whose

effects need to be understood and accounted for. In this regard it is pertinent to note that the contact fraction, κ , correlates directly with the polymer's compliance; i.e., correlates inversely with E_N .

In the next section, we examine the clues from the dichotomy of the trends in our definition-based estimates of E_N and H , obtained from P - h data and SPM analyses. We qualitatively decompose the VEP glassy polymer deformation by benchmarking against the EP deformation (P - h relationship) of the quartz standard. We also examine the effects of constraints during the localized nanoindentation deformation and recovery, vis-à-vis bulk uniaxial deformation.

5.4 Nanoindentation deformation phenomena: Elastic, EP, VEP effects

Here, we provide a separation of the various contributions to nanoindentation deformation. Such decompositions have been provided previously – e.g., see [93], [94] – considering the OP method for contact region size. Our approach recognizes the mechanistic differences between nanoindentation of compliant VEP materials such as glassy polymers and the nanoindentation of EP materials. In this section, we first estimate the hypothetical nanoindentation hardness, if the VE effects were absent. Subsequently, combining learnings from the E_N values from the previous section, and from the resultant EP deformation-based H values, we propose a mechanism for the constraint-induced nanoindentation deformation and its recovery. We retain the high κ values, because they are a consequence of the high compliance and ν , and not caused VE effects.

5.4.1 Phenomena contributing to polymer nanoindentation: Loading Analyses

In addition to the consistently high load-bearing contact fraction of the compliant glassy polymers, another consistent observation for polymers is that, the average stress or the nanoindentation property, hardness, $H = P_m/A_c$, consistently decreases with increasing P_m . We recognize that the

significant difference between polymers and the six OP materials, is that the former exhibit VE (time-dependent) deformation. Therefore, the most likely cause of this “indentation size effect” in our amorphous glassy polymers, could be the viscoelasticity exhibited by these materials. We have indicated above the FEA study [42], which employs the quadratic VEP model [122] to describe the range of phenomena. Another example [72] of addressing VE effects, including the creep effects during loading employs a generalized VE model along with the OP framework for the contact area. We provide an approach which is model-free, and qualitatively addresses time-dependence effects.

Recognizing that the contact ratio, κ , does not vary with P_m , i.e., with loading time, we assume (as a first approximation) that even during the loading period (subscript L), the ratio, $\kappa = (h_{cL} + h_b) / (h_{mL} + h_b)$, is a constant (or varies linearly, in case of HB15). This means that the contact depth would be a function only of the indentation depth (i.e., a consequence of compliance-driven upflow).

Nanoindentation data are available for $P_m = 1000 \mu\text{N}$, $P_m = 3000 \mu\text{N}$ and $P_m = 9000 \mu\text{N}$ for PB05, PC and PMMA, and for $P_m = 1000 \mu\text{N}$ and $P_m = 9000 \mu\text{N}$, for HB15. Employing h_{cL} from above, the estimate of the average stress at the end of the loading period, $H_L = P_m / (24.5(h_{cL} + h_b)^2)$, is plotted against $\ln P_m$ (Fig. 15(a)) and against $(\ln P_m)^2$ (Fig. 15(b)). Here, for HB15 only, we linearly interpolate the slight variation in κ vs $(h_m + h_b)$, to estimate the corresponding H_L .

The objective is to estimate the zero-time, limiting loading hardness, H_{L0} . The experimental data are in the range of $\ln P_m$ values, ~ 9 to ~ 7 ; hence, the extrapolation range for $\ln P_m$ is ~ 7 to 0. In comparison, the $(\ln P_m)^2$ range for the experimental data, is from ~ 85 to ~ 47 . In this case, the extrapolation is over a smaller fraction of the range, from ~ 47 to 0. The statistical spread in the data

at each $\ln P_m$ (or $(\ln P_m)^2$), indicates that both fits could be applicable (similar values for $R^2 \sim 0.97$). The statistical spread of the data at each $\ln P_m$, causes an uncertainty in the intercept, H_{L0} . The choice of the variable affects the estimate of H_{L0} by $\sim 20\%$. The consequent effect on the elastoplastic contact depth, h_{cL0} , obtained from $H_{L0} = P_m / \left(24.5 (h_{cL0} + h_b)^2 \right)$, is $\sim 10\%$. We choose $\ln P_m$ as the variable, because the loading step is at constant $\frac{d}{dt}(\ln P)$. The time required for VE effects during loading, is proportional to $\ln P_m$. Zero loading time occurs when $\ln P_m = 0$. Since the preload, $P_0 = 1 \mu\text{N}$, for $\ln P_m$ to be proportional to loading time, the units for P_m are μN . Then, at zero time, we consider that time-dependent VE effects are absent.

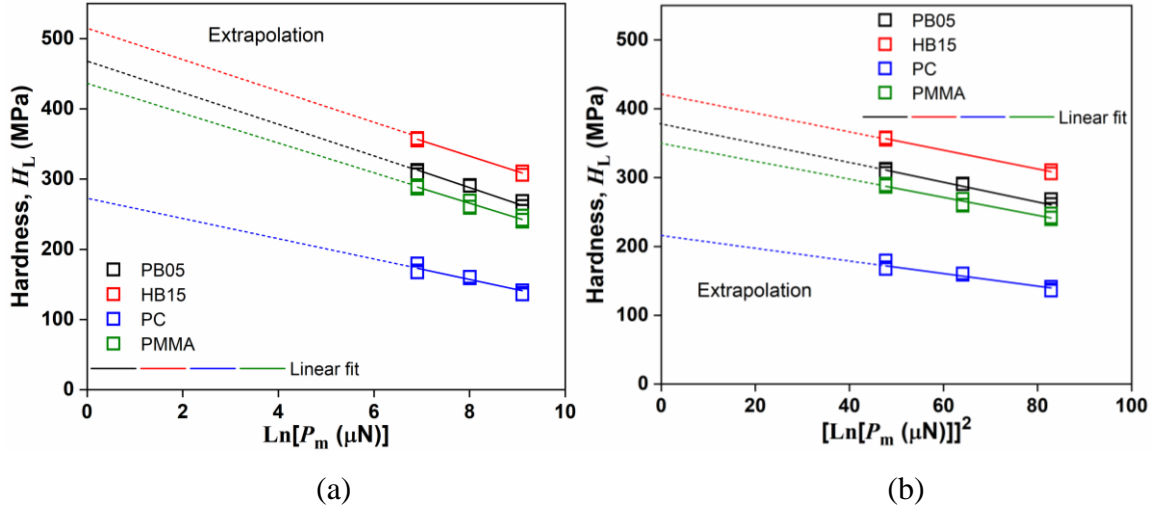


Figure 15: Estimate of EP (zero loading time) hardness, H_{L0} , by extrapolating the experimental loading hardness, H_L to zero loading time ($\ln P_m = 0$). (a) Fitting H_L vs $\ln P_m$ (b) Fitting H_L vs $(\ln P_m)^2$. The intercepts of the two methods differ by $\sim 20\%$.

Therefore, in the subsequent discussion, we will consider the effects of H_{L0} (no VE effects) obtained as the intercept of the linear fit with $\ln P_m$. Also, in that discussion and in the subsequent analysis below, we have implemented the analogous slight linear variation in κ for HB15. The extension from constant κ to linearly varying κ is straightforward.

The H_{L0} values are 473 MPa (PB05), 507 MPa (HB15), 433 MPa (PMMA) and 273 MPa (PC).

Thus, similar to the case of EP quartz standard ([Appendix H](#)), a hypothetical EP P - h loading plot can

constructed as $(h_{cEP} + h_b) = \left(\frac{P}{24.5\kappa^2 H_{L0}} \right)^{0.5}$. Considering $\kappa = \frac{(h_{cEP} + h_b)}{(h_{EP} + h_b)}$, retains the volume

conserving effect, for EP deformation as well, to estimate the EP displacement, h_{EP} , as function of

P . Then at $P = P_m$, $h_{EP} = h_{EP,m}$, and at any P during loading, the additional penetration, $(h - h_{EP})$,

would be due to VE effects (e.g., loading step creep) superimposed on the EP effects.

While we have found in [Section 5.3.4](#) that for glassy polymers, $H \leq 3\sigma_y$, this analysis finds

$H_{L0} > 3\sigma_y$. H_{L0}/σ_y values are ~ 5.4 for HB15, ~ 4.1 for PC and ~ 3.6 for PMMA. $H_{L0} > 3\sigma_y$, even

if we consider H_{L0} from [Fig. 15\(b\)](#). This means that creep effects result in a lower hardness. Thus,

the trend for hypothetical EP polymer hardness values (H_{L0}), becomes consistent with the trend,

$E_N > E$. A similar treatment on E_N , would remove VE effects on it as well. However, since the

dependence is $E_N \sim (1/\sqrt{A_c})$, as opposed to $H \sim (1/A_c)$, we find $E_N > E$, even with the VE effects

causing a greater h_m , and thus, a greater A_c . The implications of the consistent trends, $E_N > E$ and

$H_{L0} > 3\sigma_y$, are addressed in [Section 5.4.2](#).

As determined previously [147], during unloading of EP materials, we can consider that the contact

depth, $h_{c,u}$, at any unloading depth h_u from h_m to h_f , is the same as that during loading, at the

corresponding load, P . Thus, for EP materials, the average stress (instantaneous hardness, H) during

unloading, would be constant as well, and equal to that during loading at the corresponding P .

Exploiting this property of EP nanoindentation, we first identify the relevant differences between the

indentation profiles for quartz and those of glassy polymers. Then, aspects from quartz

nanoindentation analysis, on objective mapping to polymer nanoindentation, would provide

estimates of the elastic and EP components, of polymer deformation. The remaining contribution would correspond to VE aspects.

Despite the small fitting range in [section 5.1.3](#), we have found corroborating phenomenological similarity between the polymers and quartz, in the elastic unloading segment. We exploit this similarity employing the EP hardness estimates for the polymers. We translate the hypothetical elastic unloading $P-h$ curve leftwards, by a distance, $(h_m - h_{EP,m})$. The shifted curve will then represent the elastic unloading curve, corresponding to the hypothetical parabolic [10] EP loading $P-h$ curve for the polymer, from $(0, 0)$ to $((h_{EP,m} + h_b), P_m)$. The parabola for HB15 is modified to accommodate the slight variation of κ with h . [Figure 16](#) illustrates our simplified deconvolution of the elastic, EP and VEP components during loading, followed by VE unloading (unloading creep) as well as hypothetical elastic unloading.

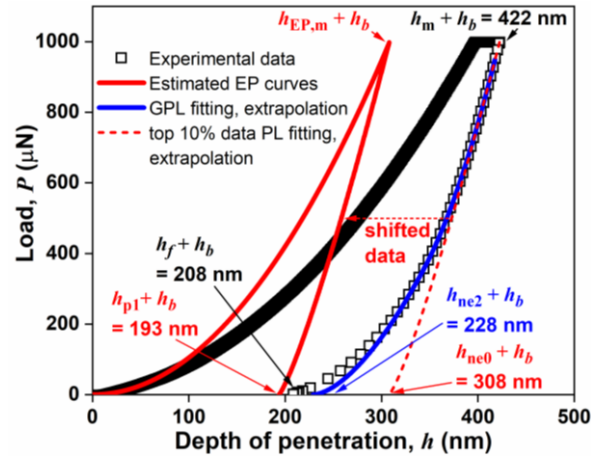


Figure 16: A simplified deconvolution of the nanoindentation deformation to facilitate visualization of its various contributions: elastic component ($h_e = h_m - h_{ne0} = 116 \text{ nm}$), time-independent plastic component ($h_p + h_b$), EP component ($h_{ep,m} + h_b = h_p + h_b + h_e = 308 \text{ nm}$), remaining time-dependent VEP component ($h_m - h_{ep,m} = h_{ne0} - h_p = 115 \text{ nm}$).

After examining the material behavior, we examine next, the effects of the surrounding constraints on the localized deformation and recovery

5.4.2 Constraint induced deformation and recovery

If we consider the hypothetical EP loading, and its corresponding hypothetical elastic unloading, then its post-unloading displacement $(h_p + h_b)$, at $P=0$, is consistently lower than $(h_f + h_b)$. However, from the post unloading SPM scans we find that the residual depth rises to h_r . This rise would not occur if entire the residual imprint (after EP loading and elastic unloading) only consisted of plastic deformation. All local VE recovery of the zone beneath the apex would be almost complete, at the time of reaching h_p . Any plastic deformation of an isolated body (such as a micropillar) would be permanent. We contrast this with constrained and constraint-induced deformation and recovery phenomena during nanoindentation.

We suggest that in the case of nanoindentation, the broad set of phenomena are a complex combination of localized VE, EP and yield events. The localized events are confounded by constraints due to the surrounding material. We speculate that (i) the influence of the surroundings is amplified by the greater upflow beneath the tip. (ii) the upflow itself might absorb part of the downward strain, reducing the yield content and distributing it as elastic strain, spread downwards, over a greater depth.

Figure 17 provides a visualization of the likely events. There is a permanent imprint of the sharp edges, that radiates outward from the tip apex. The yield region beneath the edges is very shallow, compared to a deep yielded region beneath the apex. On unload, the E_0 elastic recovery (**Section 5.1.2**) occurs everywhere in a localized sense. The outer regions recover significantly while the apex region undergoes limited recovery. However, due to VE effects, the less-yielded outer regions continue to recover further at zero load. We find that the inner regions (despite the progressively greater yielded content) also continue to recover. Hence, the local recovery of the less-yielded regions surrounding the apex, “pulls up” the significantly yielded region at the apex; i.e., the greatly yielded apex region undergoes additional constraint-induced recovery.

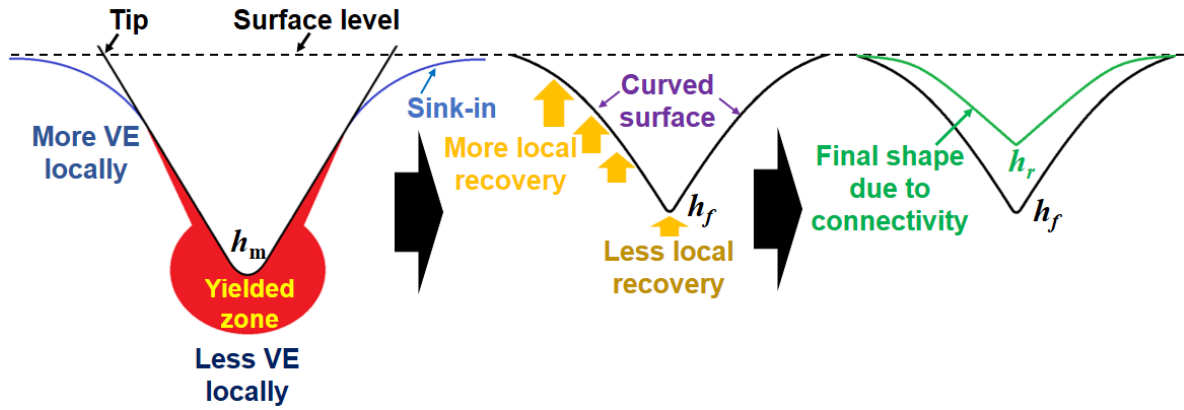


Figure 17: Visualization of the effect of the tip apex region of the residual imprint being connected to its surroundings. Even if the apex has completed VE recovery (with a deep permanently yielded zone underneath), the surrounding region with a shallow yielded region beneath the imprints of the edges, continues to recover from its VE compression, and pulls the apex upwards, giving rise to constraint-induced additional recovery.

As in post-unload constraint-induced recovery constraints from the surroundings, also affect the loading step. The lower stresses on the surrounding regions, give rise to lower deformations in those regions. Note that the LS-described sink-in occurs where there is no direct contact stress. The regions further away from the apex, asymptotically approach zero strain, and constrain the deformation at the apex. After normalizing with contact size, a , these outer regions (higher r/a values) on glassy polymers, are relatively closer to the tip surface (compared to those on OP materials) because of the upflow. The well correlated compliance-induced increase in A_c in glassy polymers, increases the required P_m for a given displacement. For a given deformation, the constraints, due to their less deformed state, increase the required load P_m , even further. The consequence thus explains our findings in [Section 5.3.4](#), that for glassy polymers, $E_N > E$ and $H_{L0} > 3\sigma_y$; i.e., in polymers, the effect of constraints due to the surroundings, is greater. The comparatively lower stresses and the greater upflow, retain the connectivity between the regions beneath the tip, with the outer regions. Such connectivity in OP-type materials is reduced, possibly because of the relatively greater normalized distances (r/a values) and creation of slip-lines during nanoindentation [148].

6. Conclusions

In this investigation, we have broadly identified the material phenomena during Berkovich nanoindentation of amorphous glassy polymers. We have considered PMMA and PC to represent thermoplastics and partly cross-linked (PB05) and highly cross-linked (HB15) SU-8 epoxies to represent thermosets. This contribution provides a rational description of the various events during glassy polymer nanoindentation. Such an understanding will enable development of physics-based predictive models and exposes the range of phenomena to account for, when building the correct “user-described models” in FE simulation platforms.

During nanoindentation, all effects, namely, elastic, viscous and plastic, occur simultaneously, from the onset of loading. To an extent, they can be separated only during unloading. Therefore, we first examine the *de facto* constant unload rate range of the rapid unloading step (full unload over 2 s), to identify the possible elastic effects. We find that the unload h - P data (h is the dependent variable) in this range, corresponds to a Generalized Power Law (GPL), where the exponent of P is a function of $\ln P$. The resultant fitted intercept at $P=0$, h_{ne2} , is one estimate of non-elastic deformation.

The GPL nature of these data suggests that the considered elastic recovery during the rapid unload over 2s, still contains viscoelastic (VE) contributions. We estimate the “instantaneous” elastic recovery contribution via Power Law (PL) fitting the h - P data in top 10% of the *de facto* constant unload rate range (i.e., the range $0.95 P_m$ up to $0.885 P_m$). The fitted intercept at $P=0$, h_{ne0} , is another estimate of non-elastic deformation. The fitted parameters of all the polymers map well with those of the benchmark quartz standard, as well as with those of other elastoplastic (EP) materials, suggesting that $(h_m - h_{ne0})$ is the likely instantaneous elastic recovery contribution. Both frameworks compute accurately and identically, the stiffness S as the slope at the unloading onset.

Visual observation of nanoindentation deformation, provides direct evidence, that for PB05, only sink-in occurs during loading, and observable pile-up occurs only during unloading. We have obtained specific quantitative evidence, via detailed SPM analyses of topographical images. The sharp edges of the indenter tip provide the permanent line imprints, and enable explicit estimation of the contact region size. Estimation of the size of non-contact region is enabled by directly estimating the blunt height via quartz calibration.

We interpret the SPM profiles to estimate the full-load deformation profile in two steps. We first estimate the ideal elastic indentation profile for an ideal Berkovich indenter, considering it to be a family of cones with varying semi-angles. The imprint sizes indicate that the sink-in at the corners, is reduced due to volume-conserving internal upflow. We find that even though the reported required criterion for OP framework validity are met ($(h_f/h_m) \sim 0.6$), the contact fractions are significantly greater than those predicted by the OP method; broadly independent of the applied load, $\kappa = h_c^\Delta/h_m^\Delta \sim 0.92-0.95$.

We represent this reduced sink-in by an outward shifting the axis of the ideal indenter deformation profile at full load, so that the Love-Sneddon topology is combined with the actual SPM-based A_c , to obtain the deformation profile at full load. This profile at full load is consistent with the internal upflow (relative to the sink-in along the edges) at the facet middle position (for PC, with its low sink-in, the pile-up is likely to be external as well).

Thus, we provide a mechanistic visualization of the events during deformation. The low moduli and high Poisson ratios of the polymers (compared to the OP materials) enable much greater compressive deformation. This greater deformation during loading, causes upward redirection of the lateral volume-conserving Poisson expansion, along the path of least resistance. This upflow is not accounted for by the OP and other frameworks.

Another key inference from the SPM data is that due to the upflow, there is simultaneous reduced sink-in (at the edges) and pile-up (at the facets), and that the maximum pile-up is further away from the contact with the indenter tip; i.e., $h_c^{\text{PU}} < h_m^{\text{PU}}$. Based on this topology, we have provided a flow schematic of the deformation phenomena, which provides a rational estimate of the contact, load-bearing pile-up.

We have estimated the conventionally defined nanoindentation properties, E_N and H , for glassy polymers. We find that for these polymers, the contact fraction κ is inversely correlated with E_N . As estimated, their magnitudes vis-à-vis the uniaxial deformation properties, E and σ_y , exhibit opposing trends, i.e., $E_N > E$, but $H < 3\sigma_y$. Hence, we have also estimated the hypothetical zero-time hardness, H_{L0} , corresponding to absence of VE effects. The nanoindentation properties then follow trends, consistent with each other; i.e., $E_N > E$ and $H_{L0} > 3\sigma_y$. These greater magnitudes suggest significant constraint effects of the surroundings on the local deformation.

The estimated H_{L0} enables a deconvolution of the loading-based time-independent EP contribution from the overall viscoelastoplastic (VEP) nanoindentation deformation. We also estimate the conventional unloading-based zero-time elastic contribution from the estimated EP loading component, in terms of the corresponding hypothetical P - h data. This representation – unloading data to “visual” evidence to loading data – facilitates a visual deconvolution of the underlying VEP deformation phenomena during nanoindentation, into the approximate elastic, EP and VE components.

Finally, we identify the constraint effects, i.e., with the extra time-dependent recovery of the highly yielded apex region, being “pulled up” during unloading and zero-load recovery, by the surrounding less yielded region. This suggests that during loading as well, these constraints will demand a greater load (even after accounting for the greater A_c) for deformation, and thus accounts for the

conventionally defined properties, E_N and H , being significantly greater than their corresponding uniaxial deformation properties, E and $3\sigma_y$.

Acknowledgments

We would like to thank the Centre of Excellence in Nanoelectronics (CEN), IIT Bombay, for providing SU-8 epoxy and facilities for the SU-8 sample fabrication. The authors would like to acknowledge the Nanoindenter lab, Central facility, IIT Bombay for providing the standard quartz, and for the nanoindentation experiments.

Funding

No funding was available for this project.

Appendix A

Structural characterization of cross-linked SU-8 via FT-IR

We place the UV exposed spin coated SU-8 inside the furnace, ramp the temperature to 95°C, and hold for 5 min. This corresponds to the post-baked sample, PB05. To obtain the hard-baked sample (HB15), after 30 min of the PB step, we raise the temperature to 150°C, and hold for 15 min. The I_{914} peak represents the epoxy group ($-C-O-C-$) in the SU-8 monomer, and I_{1608} peak is for the aromatic group, which does not take part in the cross-linking reaction [149]. With increase in extent of cross-linking, I_{914} decreases, and would vanish when the SU-8 is fully cross-linked [150]. The extent of cross-linking (%) = $\left[(A_{BE} - A_{AB}) \times 100\% / A_{BE} \right]$ [151]. Here, A_{AB} is the value of the I_{914} peak, normalized by the I_{1608} peak, of the baked sample after UV-exposure. A_{BE} is the same ratio of the sample, before UV exposure.

Appendix B

h vs P unload curve fitting equations

We consider here a quadratic fit model for $1/m$. Since $1/m$ is the power in the $h - h_{ne}$ vs P plot (PL model) for clarity, we represent $\ln(h - h_{ne})$ by D_2 and $\ln P$ by F .

$$\frac{dD_2}{dF} = k_2 F^2 + k_1 F + k_0 \quad \text{eqn. B.1}$$

Integrating and rearranging,

$$D_2 = \left[F \left(\frac{k_2 F^2}{3} + \frac{k_1 F}{2} + k_0 \right) \right] + k_Q \quad \text{eqn. B.2}$$

Hence,

$$h = g P^{\frac{k_2 (\ln P)^2}{3} + \frac{k_1 \ln P}{2} + k_0} + h_{ne} \quad \text{eqn. B.3}$$

$g = \exp(k_Q)$, k_2 , k_1 , and k_0 are the fitting parameters for the h vs P unload data.

The stiffness, S is given by eqn. 3. For any polymer, the S values from the different methods, all lie numerically, within $\sim 10\%$ of each other (Table B). However, for $P_m = 1000 \mu\text{N}$, we find, S (PB05) $>$ S (HB15), via all methods except the GPL method. For $P_m = 9000 \mu\text{N}$, S (PB05) $>$ S (HB15), only for the PL equation fitting. Also recognizing that the polymer nanoindentation h_f fitted values via all the literature methods, are unphysical, in general, we infer that only the data-faithful GPL method yields S (PB05) $<$ S (HB15).

Table B: Calculated S ($\mu\text{N}/\text{nm}$) estimates via various methods reported in the literature.

References	P_m (μN)	PB05	HB15	PC	PMMA
Oliver-Pharr [2]	1000	11.53 ± 0.02	9.93 ± 0.03	9.13 ± 0.01	12.16 ± 0.06
	9000	31.86 ± 0.10	30.83 ± 0.02	26.45 ± 0.02	32.95 ± 0.04
Kossman <i>et al.</i> [71]	1000	11.86 ± 0.03	11.06 ± 0.05	9.88 ± 0.02	12.17 ± 0.06
	9000	32.96 ± 0.07	35.27 ± 0.10	28.81 ± 0.03	33.03 ± 0.03
Liu <i>et al.</i> [72]	1000	10.80 ± 0.05	10.32 ± 0.09	9.51 ± 0.16	12.28 ± 0.16
	9000	30.07 ± 0.10	32.79 ± 0.36	26.71 ± 0.40	33.70 ± 0.26
Gong <i>et al.</i> [69]	1000	11.11 ± 0.02	10.14 ± 0.04	9.30 ± 0.01	12.20 ± 0.04
	9000	30.78 ± 0.11	31.75 ± 0.04	27.21 ± 0.02	33.26 ± 0.02
GPL method	1000	10.59 ± 0.09	11.02 ± 0.09	9.87 ± 0.04	12.22 ± 0.09
	9000	30.63 ± 0.14	34.31 ± 0.06	27.97 ± 0.02	33.12 ± 0.07

Appendix C

Elastic Nanoindentation Unloading of EP Quartz Standard

Here, we briefly describe the EP behavior of the quartz standard, so as to employ it as a benchmark, against which, the corresponding response of the polymers can be described. The data for quartz are available from the tip calibration experiments carried out on various days during the tip's lifetime.

We have considered loading up to the maximum load, $P_m = 10,000 \mu\text{N}$, to represent all loads from

$100 \mu\text{N}$ onwards. The unloading follows the PL, $P = B(h - h_f)^m$, (in the range from $0.2 P_m$ to $0.95 P_m$), where B , m , h_f are the fitting constants; h_f is the residual depth at $P = 0 \mu\text{N}$. Hence,

stiffness, $S = m P_m / (h_m - h_f)$. We fit $B = \sum_{i=0}^3 b_i \times (h_m + h_b)^i$, and employ our empirical finding,

$(h_f + h_b) = \sqrt{\left(\frac{P_m}{0.48} \right)}$; we find that m varies linearly from ~ 1.25 (for $P_m \sim 2,000 \mu\text{N}$) to ~ 1.31 (for

$P_m \sim 10,000 \mu\text{N}$). For the elastoplastic quartz standard, the stiffness, S , varies in a parabolic fashion vs P_m (Fig. C(a)), as it does in case of the amorphous glassy polymers (Fig. C(b)).

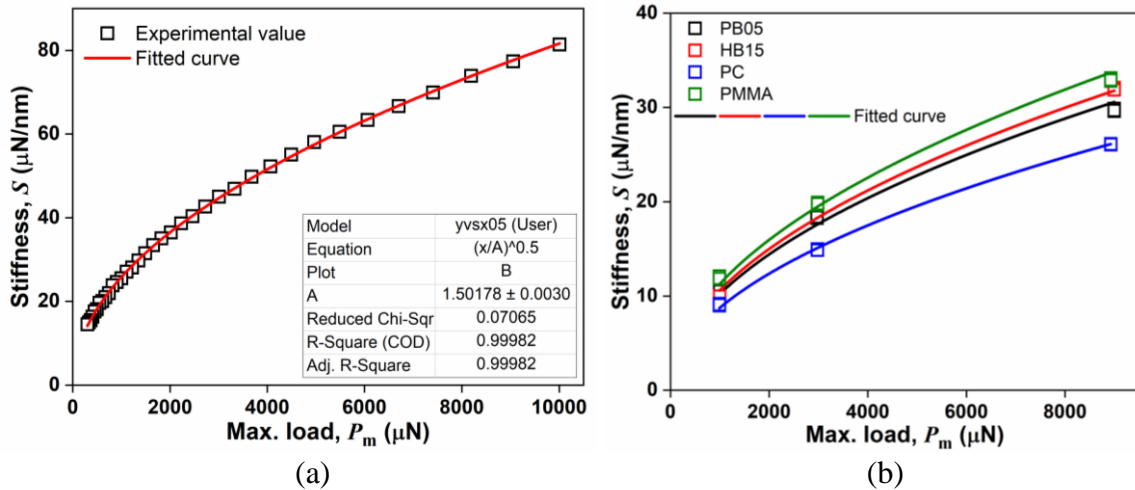


Figure C: S exhibits a parabolic relationship vs P_m for (a) the quartz standard (b) glassy polymers.

Appendix D

Blunt height estimation of tip during each usage day

The P - h curves of the tip area calibration on quartz standard, provide the contact depth, h_c , as per the OP method. For each P_m , the known $E_r = 69.6 \pm 3.5$ GPa, and $H = 9.3 \pm 0.9$ GPa, yield two A_c values, $A_c^{E_r} = \pi S^2 / 4E_r^2$ and $A_c^H = P_m / H$, respectively. We consider the average of the two areas, recognizing that $A_c(h_c) \approx 24.5 \times (h_c + h_b)^2$ [27], [55], [57], [58], [152], to yield the fitted h_b . This fitting is implemented by self-consistently disregarding data in the low h_c range ($h_c < R/3$) [153], where $R = h_b [\sin \alpha / (1 - \sin \alpha)]$, is the tip radius.

We have performed SEM analyses (model: dual beam FEI Carl Zeiss Auriga™) of the indenter tip on usage day 568, as shown in Fig. D(a) provides the direct estimate of h_b . Figure D(b) is a plot of the average of the two h_b values as a function of usage days (when the quartz calibration was performed). We find that the linear fit of the average h_b values, describes the trend very well, and the SEM h_b value (~ 27 nm) lies very clearly on the linear fit.

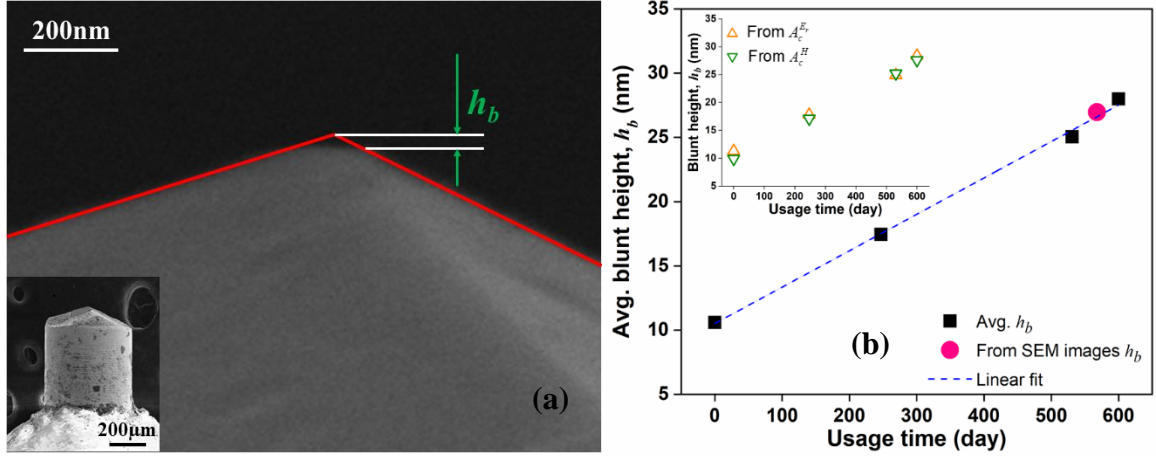


Figure D: (a) SEM images of Berkovich tip and h_b measurement and (b) h_b values change by progressive utilization. The linear fit is $h_b = pt + q$.

Appendix E

Viscoelastic effects on imaged pile-up

Figure C(a) demonstrates via consecutive SPM profiles of HB15 and PC ($r > a_c$), at times t_1 and t_2

that $\frac{h_{r1}^{p,PU}(r)}{h_{r2}^{p,PU}(r)} \approx \frac{(h_c - h_{r1})}{(h_c - h_{r2})}$. The relative residuals (%) from proportional profiles for HB15 and PC

are shown in Fig. E(b). It is seen that the residuals are random, scattered and within $\pm 15\%$.

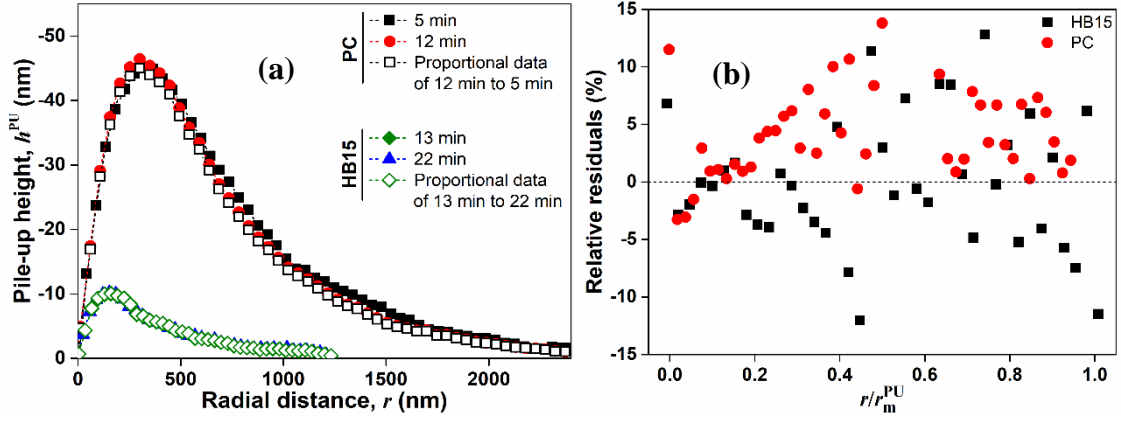


Figure E: (a) Pile-up profiles for HB15 and PC. The mentioned times indicate the delay time when the images were acquired just after removal of load. (b) the relative residuals (%) from proportional profiles for HB15 and PC. Here, we have taken $r_{m,HB15}^{PU} = 1200$ nm and $r_{m,PC}^{PU} = 2400$ nm.

Appendix F

Polymer Nanoindentation: Surface Topology Estimate at P_m

Figure F(a)-(b) is a rational quantification of the likely surface topology for PC, which would yield the profile obtained via the SPM imaging.

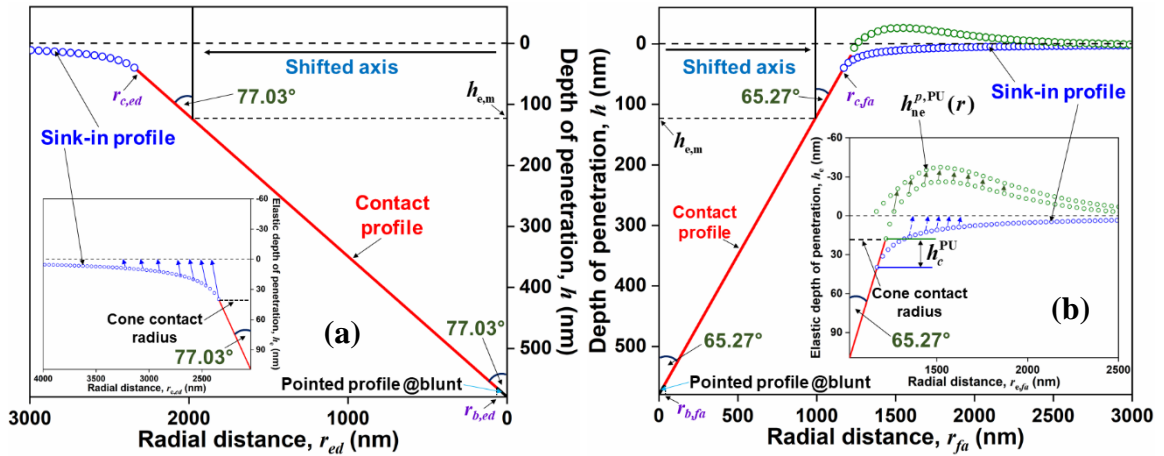


Figure F: Deformation profile for PC at P_m (a) edge side, (b) facet side.

Appendix G

Effects of Pile-up on Contact Area

The increase in A_c , is the minor segment of a circle, bound by an arc (half-angle = η) and the chord (the a -line). The projected area of the elevation, i.e., the segment area is calculated as shown in Fig. G(a)-(b). The arc sector radius, $r^{\text{PU}} = \left(h_c^{\text{PU}}/2\right) + \left(a^2/8h_c^{\text{PU}}\right)$. As h_c^{PU} increases, r^{PU} decreases and η increases (Fig. G(c)). The h_c^{PU} -based additional projected area (eqn. 8) is added to the imprint-based A_c^{Δ} [11], [12], [16]–[20]. The values for r^{PU} , η (radians), and A_c^{PU} for all the indentations, are listed in [Supporting Information 6](#).

$$A_c^{\text{PU}} = 3 \left[\frac{\pi r^2 \eta}{360} - \left(\frac{a}{2} \frac{a/2}{\tan(\eta/2)} \right) \right]$$

eqn. G.1

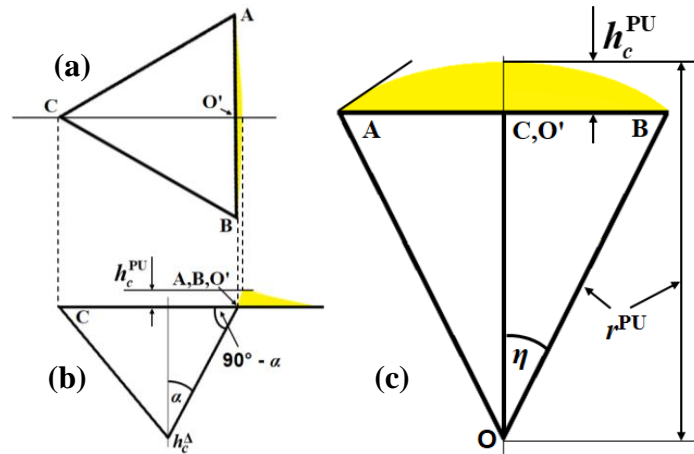


Figure G: Schematic depicting the deformation profile with pile-up arc: (a) top view (b) side view, and (c) the section of the hypothetical circle (r^{PU} and η) with the pile-up arc (arc tangent is indicated). Note that the depth scales in (a)-(b) and (c) are different; also, $r^{\text{PU}} \gg h_c^{\Delta}$ and $\eta \gg \alpha$.

Our analysis estimates the h_c^{PU} on the facet via a proportional downscaling (Fig. 11(b)) of the SPM-based profile, followed by identifying the location of the contact. Directly considering the SPM-imaged h_m^{PU} (instead of h_c^{PU}), increases the overall A_c estimates by $\sim 1.5\%$ for HB15 and by $\sim 6.1\%$ for PC.

Appendix H

Loading Data Analysis for Quartz Nanoindentation

We have considered loading up to the maximum load, $P_m = 10,000 \mu\text{N}$, to represent all loads from $100 \mu\text{N}$ onwards. The loading curve for any tip usage day, is described by $P(\mu\text{N}) \sim 0.11 \times (h(\text{nm}) + h_b)^2$. This power law is expected for purely elastic materials [6]–[8] as well as for EP materials [10]. There is no additional displacement (no creep) during the hold period at P_m , which is consistent with quartz's EP (very large viscosity) nature. Consequently, the average stress (instantaneous hardness, H) is constant during loading (i.e., $P(\mu\text{N}) \sim 0.225 \times (h_c(\text{nm}) + h_b)^2$). The contact depth, h_c , during loading at any given P , can be considered to be that at the onset of unloading from that P ; i.e., we substitute $P_m = P$, in the equation, $h_c = h_m - (0.75P_m/S)$.

References

- [1] A. C. Fischer-Cripps, *Nanoindentation*. in Mechanical Engineering Series. New York, NY: Springer New York, 2004. doi: 10.1007/978-1-4757-5943-3.
 - [2] W. C. Oliver and G. M. Pharr, “An improved technique for determining hardness and elastic modulus using load and displacement sensing indentation experiments,” *J. Mater. Res.*, vol. 7, pp. 1564–1583, 1992, doi: 10.1557/JMR.1992.0613.
 - [3] W. C. Oliver and G. M. Pharr, “Measurement of hardness and elastic modulus by instrumented indentation: advances in understanding and refinements to methodology,” *J. Mater. Res.*, vol. 19, no. 1, pp. 3–20, 2004, doi: 10.1557/jmr.2004.19.1.3.
 - [4] G. M. Pharr, W. C. C. Oliver, and F. R. R. Brotzen, “On the generality of the relationship among contact stiffness, contact area, and elastic modulus during indentation,” *J. Mater. Res.*, vol. 7, no. 3, pp. 613–617, 1992, doi: 10.1557/JMR.1992.0613.
 - [5] A. E. H. Love, “Boussinesq’s problem for a rigid cone,” *Q. J. Math.*, vol. os-10, pp. 161–175, 1939, doi: 10.1093/qmath/os-10.1.161.
 - [6] J. W. Harding and I. N. Sneddon, “The elastic stresses produced by the indentation of the plane surface of a semi-infinite elastic solid by a rigid punch,” *Math. Proc. Cambridge Philos. Soc.*, vol. 41, pp. 16–26, Jun. 1945, doi: 10.1017/S0305004100022325.
 - [7] I. N. Sneddon, “Boussinesq’s problem for a rigid cone,” *Math. Proc. Cambridge Philos. Soc.*, vol. 44, no. 4, pp. 492–507, Oct. 1948, doi: 10.1017/S0305004100024518.
 - [8] I. N. Sneddon, “The relation between load and penetration in the axisymmetric boussinesq problem for a punch of arbitrary profile,” *Int. J. Eng. Sci.*, vol. 3, no. 1, pp. 47–57, May 1965, doi: 10.1016/0020-7225(65)90019-4.
 - [9] J. L. Loubet, J. M. Georges, O. Marchesini, and G. Meille, “Vickers Indentation Curves of Magnesium Oxide (MgO),” *J. Tribol.*, vol. 106, pp. 43–48, Jan. 1984, doi: 10.1115/1.3260865.
 - [10] J. L. Loubet, J. M. Georges, and G. Meille, “Vickers Indentation Curves of Elastoplastic Materials,” in *Microindentation Techniques in Materials Science and Engineering, ASTM STP889*, P. J. Blau and B. R. Lawn, Eds., Philadelphia: American Society for Testing and Materials, 1986, pp. 72–89.
-

- [11] E. Renner, Y. Gaillard, F. Richard, F. Amiot, and P. Delobelle, “Sensitivity of the residual topography to single crystal plasticity parameters in Berkovich nanoindentation on FCC nickel,” *Int. J. Plast.*, vol. 77, pp. 118–140, 2016, doi: 10.1016/j.ijplas.2015.10.002.
 - [12] R. Saha and W. D. Nix, “Soft films on hard substrates - Nanoindentation of tungsten films on sapphire substrates,” *Mater. Sci. Eng. A*, vol. 319–321, pp. 898–901, 2001, doi: 10.1016/S0921-5093(01)01076-0.
 - [13] S. Bec, A. Tonck, J.-M. Georges, E. Georges, and J.-L. Loubet, “Improvements in the indentation method with a surface force apparatus,” *Philos. Mag. A*, vol. 74, no. 5, pp. 1061–1072, Nov. 1996, doi: 10.1080/01418619608239707.
 - [14] G. Hochstetter, A. Jimenez, and J. L. Loubet, “Strain-rate effects on hardness of glassy polymers in the nanoscale range. Comparison between quasi-static and continuous stiffness measurements,” *J. Macromol. Sci. Part B*, vol. 38, no. 5–6, pp. 681–692, Sep. 1999, doi: 10.1080/00222349908248131.
 - [15] M. Hardiman, T. J. Vaughan, and C. T. McCarthy, “The effects of pile-up, viscoelasticity and hydrostatic stress on polymer matrix nanoindentation,” *Polym. Test.*, vol. 52, pp. 157–166, 2016, doi: 10.1016/j.polymertesting.2016.04.003.
 - [16] K. O. Kese, Z. C. Li, and B. Bergman, “Method to account for true contact area in soda-lime glass during nanoindentation with the Berkovich tip,” *Mater. Sci. Eng. A*, vol. 404, no. 1–2, pp. 1–8, 2005, doi: 10.1016/j.msea.2005.06.006.
 - [17] K. Kese and Z. C. Li, “Semi-ellipse method for accounting for the pile-up contact area during nanoindentation with the Berkovich indenter,” *Scr. Mater.*, vol. 55, no. 8, pp. 699–702, Oct. 2006, doi: 10.1016/j.scriptamat.2006.06.030.
 - [18] J. Hu, Y. Zhang, W. Sun, and T. Zhang, “Nanoindentation-induced pile-up in the residual impression of crystalline Cu with different grain size,” *Crystals*, vol. 8, pp. 1–10, 2018, doi: 10.3390/cryst8010009.
 - [19] L.-N. Zhu, B.-S. Xu, H.-D. Wang, and C.-B. Wang, “Determination of hardness of plasma-sprayed FeCrBSi coating on steel substrate by nanoindentation,” *Mater. Sci. Eng. A*, vol. 528, no. 1, pp. 425–428, Nov. 2010, doi: 10.1016/j.msea.2010.09.028.
 - [20] P. Zhu, Y. Zhao, S. Agarwal, J. Henry, and S. J. Zinkle, *Toward accurate evaluation of bulk hardness from nanoindentation testing at low indent depths*, vol. 213. 2022. doi: 10.1016/j.matdes.2021.110317.
-

- [21] J. L. Loubet, M. Bauer, A. Tonck, S. Bec, and B. Gauthier-Manuel, “Nanoindentation with a surface force apparatus,” *Mech. Prop. Deform. Behav. Mater. Having Ultra-Fine Microstruct.*, vol. 233, pp. 429–447, 1993, doi: https://doi.org/10.1007/978-94-011-1765-4_28.
 - [22] S. I. Bulychev, V. P. Alekhin, M. K. Shorshorov, and A. P. Ternovskii, “Mechanical properties of materials studied from kinetic diagrams of load versus depth of impression during microimpression,” *Strength Mater.*, vol. 8, no. 9, pp. 1084–1089, 1976, doi: 10.1007/BF01529860.
 - [23] D. Tabor, “A simple theory of static and dynamic hardness,” *Proc. R. Soc. London. Ser. A. Math. Phys. Sci.*, vol. 192, no. 1029, pp. 247–274, 1948, doi: 10.1098/rspa.1948.0008.
 - [24] D. Tranchida, S. Piccarolo, J. Loos, and A. Alexeev, “Accurately evaluating Young’s modulus of polymers through nanoindentations: A phenomenological correction factor to the Oliver and Pharr procedure,” *Appl. Phys. Lett.*, vol. 89, pp. 2004–2007, 2006, doi: 10.1063/1.2364863.
 - [25] D. Tranchida, S. Piccarolo, J. Loos, and A. Alexeev, “Mechanical characterization of polymers on a nanometer scale through nanoindentation. A study on pile-up and viscoelasticity,” *Macromolecules*, vol. 40, no. 4, pp. 1259–1267, 2007, doi: 10.1021/ma062140k.
 - [26] J. C. Hay, A. Bolshakov, and G. M. Pharr, “A critical examination of the fundamental relations used in the analysis of nanoindentation data,” *J. Mater. Res.*, vol. 14, no. 6, pp. 2296–2305, Jun. 1999, doi: 10.1557/JMR.1999.0306.
 - [27] Y. Choi, H.-S. Lee, and D. Kwon, “Analysis of sharp-tip-indentation load–depth curve for contact area determination taking into account pile-up and sink-in effects,” *J. Mater. Res.*, vol. 19, no. 11, pp. 3307–3315, Nov. 2004, doi: 10.1557/JMR.2004.0419.
 - [28] V. Tvergaard and A. Needleman, “Polymer indentation: Numerical analysis and comparison with a spherical cavity model,” *J. Mech. Phys. Solids*, vol. 59, no. 9, pp. 1669–1684, 2011, doi: 10.1016/j.jmps.2011.06.006.
 - [29] R. Seltzer, A. P. Cisilino, P. M. Frontini, and Y. W. Mai, “Determination of the DruckerPrager parameters of polymers exhibiting pressure-sensitive plastic behaviour by depth-sensing indentation,” *Int. J. Mech. Sci.*, vol. 53, no. 6, pp. 471–478, Jun. 2011, doi: 10.1016/j.ijmecsci.2011.04.002.
-

- [30] D. J. Celentano, B. Guelorget, M. François, M. A. Cruchaga, and A. Slimane, “Numerical simulation and experimental validation of the microindentation test applied to bulk elastoplastic materials,” *Model. Simul. Mater. Sci. Eng.*, vol. 20, no. 4, p. 045007, Jun. 2012, doi: 10.1088/0965-0393/20/4/045007.
 - [31] V. Tvergaard and A. Needleman, “Effect of viscoplastic material parameters on polymer indentation,” *Model. Simul. Mater. Sci. Eng.*, vol. 20, no. 6, 2012, doi: 10.1088/0965-0393/20/6/065002.
 - [32] Z. Hu, K. J. Lynne, S. P. Markondapatnaikuni, and F. Delfanian, “Material elastic-plastic property characterization by nanoindentation testing coupled with computer modeling,” *Mater. Sci. Eng. A*, vol. 587, pp. 268–282, 2013, doi: 10.1016/j.msea.2013.08.071.
 - [33] V. Tvergaard and A. Needleman, “Indentation of pressurized viscoplastic polymer spherical shells,” *J. Mech. Phys. Solids*, vol. 93, pp. 16–33, Aug. 2016, doi: 10.1016/j.jmps.2016.03.007.
 - [34] V. Tvergaard and A. Needleman, “Indentation of pressurized viscoplastic polymer spherical shells,” *J. Mech. Phys. Solids*, vol. 93, pp. 16–33, 2016, doi: 10.1016/j.jmps.2016.03.007.
 - [35] L. Zheng *et al.*, “Mechanical characterization of PMMA by AFM nanoindentation and finite element simulation,” *Mater. Res. Express*, vol. 3, no. 11, 2016, doi: 10.1088/2053-1591/3/11/115302.
 - [36] Z. Wang, P. Gu, H. Zhang, Z. Zhang, and X. Wu, “Indenter geometrical effects on sub-micro/nano indentation and scratch behaviors of polymeric surfaces,” *Mech. Adv. Mater. Struct.*, vol. 23, no. 3, pp. 291–300, 2016, doi: 10.1080/15376494.2014.955154.
 - [37] M. Hardiman, T. J. Vaughan, and C. T. McCarthy, “A review of key developments and pertinent issues in nanoindentation testing of fibre reinforced plastic microstructures,” *Compos. Struct.*, vol. 180, pp. 782–798, 2017, doi: 10.1016/j.compstruct.2017.08.004.
 - [38] Y. Wang, D. Raabe, C. Klüber, and F. Roters, “Orientation dependence of nanoindentation pile-up patterns and of nanoindentation microtextures in copper single crystals,” *Acta Mater.*, vol. 52, no. 8, pp. 2229–2238, May 2004, doi: 10.1016/j.actamat.2004.01.016.
 - [39] C. Jiang, M. Davis, and J. Zekonyte, “Finding Minimal Optimal Indent Separation for Polystyrene via Instrumental Nanoindentation and FEA Method,” *Appl. Sci.*, vol. 10, no. 12, p. 4262, Jun. 2020, doi: 10.3390/app10124262.
 - [40] K. Goto, I. Watanabe, and T. Ohmura, “Inverse estimation approach for elastoplastic
-

- properties using the load-displacement curve and pile-up topography of a single Berkovich indentation,” *Mater. Des.*, vol. 194, p. 108925, Sep. 2020, doi: 10.1016/j.matdes.2020.108925.
- [41] M. C. Barick, Y. Gaillard, A. Lejeune, F. Amiot, and F. Richard, “On the uniqueness of intrinsic viscoelastic properties of materials extracted from nanoindentation using FEMU,” *Int. J. Solids Struct.*, vol. 202, pp. 929–946, Oct. 2020, doi: 10.1016/j.ijsolstr.2020.03.015.
- [42] H. Li, J. Chen, Q. Chen, and M. Liu, “Determining the constitutive behavior of nonlinear visco-elastic-plastic PMMA thin films using nanoindentation and finite element simulation,” *Mater. Des.*, vol. 197, p. 109239, Jan. 2021, doi: 10.1016/j.matdes.2020.109239.
- [43] K. Li *et al.*, “Experimental and simulation analysis of residual topography dominated deformation mechanism of nanoindentation: a case study of Inconel 625 superalloy,” *J. Mater. Res. Technol.*, vol. 13, pp. 1521–1533, Jul. 2021, doi: 10.1016/j.jmrt.2021.05.054.
- [44] A. Greco, E. Sgambitterra, and F. Furgiele, “A new methodology for measuring residual stress using a modified Berkovich nano-indenter,” *Int. J. Mech. Sci.*, vol. 207, no. July, p. 106662, 2021, doi: 10.1016/j.ijmecsci.2021.106662.
- [45] M. Wu, X. Gao, and H. Lin, “Simulation analysis of the deformation behavior of nanoindentation based on elasto–plastic constitutive model,” *Polym. Bull.*, vol. 80, no. 5, pp. 4879–4889, 2023, doi: 10.1007/s00289-022-04292-1.
- [46] S. Park, K. P. Marimuthu, G. Han, and H. Lee, “Deep learning based nanoindentation method for evaluating mechanical properties of polymers,” *Int. J. Mech. Sci.*, vol. 246, p. 108162, May 2023, doi: 10.1016/j.ijmecsci.2023.108162.
- [47] Z. Shen, R. Dong, J. Li, Y. Su, and X. Long, “Determination of gradient residual stress for elastoplastic materials by nanoindentation,” *J. Manuf. Process.*, vol. 109, pp. 359–366, Jan. 2024, doi: 10.1016/j.jmapro.2023.10.030.
- [48] M. Mata and J. Alcalá, “The role of friction on sharp indentation,” *J. Mech. Phys. Solids*, vol. 52, no. 1, pp. 145–165, Jan. 2004, doi: 10.1016/S0022-5096(03)00075-9.
- [49] S. Swaddiwudhipong, L. H. Poh, J. Hua, Z. S. Liu, and K. K. Tho, “Modeling nano-indentation tests of glassy polymers using finite elements with strain gradient plasticity,” *Mater. Sci. Eng. A*, vol. 404, no. 1–2, pp. 179–187, Sep. 2005, doi: 10.1016/j.msea.2005.05.063.
- [50] S. Bellemare, M. Dao, and S. Suresh, “The frictional sliding response of elasto-plastic materials in contact with a conical indenter,” *Int. J. Solids Struct.*, vol. 44, no. 6, pp. 1970–
-

- 1989, Mar. 2007, doi: 10.1016/j.ijsolstr.2006.08.008.
- [51] C. G. N. Pelletier, J. M. J. Den Toonder, L. E. Govaert, N. Hakiri, and M. Sakai, “Quantitative assessment and prediction of contact area development during spherical tip indentation of glassy polymers,” *Philos. Mag.*, vol. 88, no. 9, pp. 1291–1306, Mar. 2008, doi: 10.1080/14786430802123224.
- [52] B. Poon, D. Rittel, and G. Ravichandran, “An analysis of nanoindentation in elasto-plastic solids,” *Int. J. Solids Struct.*, vol. 45, no. 25–26, pp. 6399–6415, 2008, doi: 10.1016/j.ijsolstr.2008.08.016.
- [53] F. Bédoui, F. Sansoz, and N. S. Murthy, “Incidence of nanoscale heterogeneity on the nanoindentation of a semicrystalline polymer: Experiments and modeling,” *Acta Mater.*, vol. 56, no. 10, pp. 2296–2306, Jun. 2008, doi: 10.1016/j.actamat.2008.01.021.
- [54] J. K. Deuschle, H. Matthias Deuschle, S. Enders, and E. Arzt, “Contact area determination in indentation testing of elastomers,” *J. Mater. Res.*, vol. 24, no. 3, pp. 736–748, Mar. 2009, doi: 10.1557/jmr.2009.0093.
- [55] E. Ramakers-van Dorp, T. Haenel, D. Ciongwa, B. Möglinger, and B. Hausnerova, “Development of an Advanced Dynamic Microindentation System to Determine Local Viscoelastic Properties of Polymers,” *Polymers (Basel)*, vol. 11, no. 5, p. 833, May 2019, doi: 10.3390/polym11050833.
- [56] B. Du, O. K. C. Tsui, Q. Zhang, and T. He, “Study of Elastic Modulus and Yield Strength of Polymer Thin Films Using Atomic Force Microscopy,” *Langmuir*, vol. 17, no. 11, pp. 3286–3291, May 2001, doi: 10.1021/la001434a.
- [57] J. Čech, P. Haušild, O. Kovářík, and A. Materna, “Examination of Berkovich indenter tip bluntness,” *Mater. Des.*, vol. 109, pp. 347–353, Nov. 2016, doi: 10.1016/j.matdes.2016.07.033.
- [58] F. Alisafaei, C.-S. Han, and N. Lakhera, “Characterization of indentation size effects in epoxy,” *Polym. Test.*, vol. 40, no. October 2015, pp. 70–78, Dec. 2014, doi: 10.1016/j.polymertesting.2014.08.012.
- [59] B. Du, J. Zhang, Q. Zhang, D. Yang, T. He, and O. K. C. Tsui, “Nanostructure and Mechanical Measurement of Highly Oriented Lamellae of Melt-Drawn HDPE by Scanning Probe Microscopy,” *Macromolecules*, vol. 33, no. 20, pp. 7521–7528, Oct. 2000, doi: 10.1021/ma000943g.
-

- [60] T. Sawa, Y. Akiyama, A. Shimamoto, and K. Tanaka, "Nanoindentation of a 10 nm thick thin film," *J. Mater. Res.*, vol. 14, no. 6, pp. 2228–2232, Jun. 1999, doi: 10.1557/JMR.1999.0299.
 - [61] T. Sawa and K. Tanaka, "Simplified method for analyzing nanoindentation data and evaluating performance of nanoindentation instruments," *J. Mater. Res.*, vol. 16, no. 11, pp. 3084–3096, Nov. 2001, doi: 10.1557/JMR.2001.0426.
 - [62] N. . Randall, C. Julia-Schmutz, J. . Soro, J. von Stebut, and G. Zacharie, "Novel nanoindentation method for characterising multiphase materials," *Thin Solid Films*, vol. 308–309, no. 1–4, pp. 297–303, Oct. 1997, doi: 10.1016/S0040-6090(97)00558-0.
 - [63] B. P. A. Gabriele, C. J. Williams, M. E. Lauer, B. Derby, and A. J. Cruz-Cabeza, "Nanoindentation of molecular crystals: lessons learned from aspirin," *Cryst. Growth Des.*, vol. 20, no. 9, pp. 5956–5966, 2020, doi: 10.1021/acs.cgd.0c00635.
 - [64] A. Selby, C. Maldonado-Codina, and B. Derby, "Influence of specimen thickness on the nanoindentation of hydrogels: Measuring the mechanical properties of soft contact lenses," *J. Mech. Behav. Biomed. Mater.*, vol. 35, pp. 144–156, 2014, doi: 10.1016/j.jmbbm.2013.11.023.
 - [65] S. Hengsberger, A. Kulik, and P. h. Zysset, "Nanoindentation discriminates the elastic properties of individual human bone lamellae under dry and physiological conditions," *Bone*, vol. 30, no. 1, pp. 178–184, 2002, doi: 10.1016/S8756-3282(01)00624-X.
 - [66] J. D. Kaufman, G. J. Miller, E. F. Morgan, and C. M. Klapperich, "Time-dependent mechanical characterization of poly(2- hydroxyethyl methacrylate) hydrogels using nanoindentation and unconfined compression," *J. Mater. Res.*, vol. 23, no. 5, pp. 1472–1481, May 2008, doi: 10.1557/JMR.2008.0185.
 - [67] M. Olek, K. Kempa, S. Jurga, and M. Giersig, "Nanomechanical Properties of Silica-Coated Multiwall Carbon NanotubesPoly(methyl methacrylate) Composites," *Langmuir*, vol. 21, no. 7, pp. 3146–3152, Mar. 2005, doi: 10.1021/la0470784.
 - [68] M. Y. N'jock *et al.*, "A criterion to identify sinking-in and piling-up in indentation of materials," *Int. J. Mech. Sci.*, vol. 90, pp. 145–150, 2015, doi: 10.1016/j.ijmecsci.2014.11.008.
 - [69] J. Gong, B. Deng, and D. Jiang, "A universal function for the description of nanoindentation unloading data: Case study on soda-lime glass," *J. Non. Cryst. Solids*, vol. 544, pp. 120067-1–8, 2020, doi: 10.1016/j.jnoncrysol.2020.120067.
 - [70] S. V. Kontomaris, A. Stylianou, K. S. Nikita, A. Malamou, and T. Stylianopoulos, "A
-

simplified approach for the determination of fitting constants in Oliver-Pharr method regarding biological samples,” *Phys. Biol.*, vol. 16, no. 5, pp. 056003-1–8, 2019, doi: 10.1088/1478-3975/ab252e.

- [71] S. Kossman, T. Coorevits, A. Iost, and D. Chicot, “A new approach of the Oliver and Pharr model to fit the unloading curve from instrumented indentation testing,” *J. Mater. Res.*, vol. 32, pp. 2230–2240, 2017, doi: 10.1557/jmr.2017.120.
 - [72] E. Liu, L. Kong, G. Xiao, J. Lin, G. Zhao, and H. Li, “Creep correction of elastic modulus and hardness for viscoelastic materials during microindentation,” *Polym. Adv. Technol.*, vol. 32, pp. 955–963, 2021, doi: 10.1002/pat.5142.
 - [73] S. Chattaraj, P. Pant, and H. Nanavati, “Inter-relationships between mechanical properties of glassy polymers from nanoindentation and uniaxial compression,” *Polymer (Guildf)*, vol. 144, pp. 128–141, May 2018, doi: 10.1016/j.polymer.2018.04.040.
 - [74] S. Chattaraj, P. Pant, D. N. D. N. Pawaskar, and H. Nanavati, “How many network chains of a densely crosslinked glassy thermoset deform cooperatively at yield?,” *Polymer (Guildf)*, vol. 82, pp. 305–318, Jan. 2016, doi: 10.1016/j.polymer.2015.11.023.
 - [75] N. X. Randall, “Direct measurement of residual contact area and volume during the nanoindentation of coated materials as an alternative method of calculating hardness,” *Philos. Mag. A Phys. Condens. Matter, Struct. Defects Mech. Prop.*, vol. 82, no. 10, pp. 1883–1892, 2002, doi: 10.1080/01418610208235700.
 - [76] A. A. Y. Jee and M. Lee, “Comparative analysis on the nanoindentation of polymers using atomic force microscopy,” *Polym. Test.*, vol. 29, no. 1, pp. 95–99, 2010, doi: 10.1016/j.polymertesting.2009.09.009.
 - [77] A. Samadi-Dooki, L. Malekmotiei, and G. Z. G. Z. Voyiadjis, “Characterizing shear transformation zones in polycarbonate using nanoindentation,” *Polymer (Guildf)*, vol. 82, pp. 238–245, 2016, doi: 10.1016/j.polymer.2015.11.049.
 - [78] L. Malekmotiei, A. Samadi-Dooki, and G. Z. G. Z. Voyiadjis, “Nanoindentation study of yielding and plasticity of poly(methyl methacrylate),” *Macromolecules*, vol. 48, no. 15, pp. 5348–5357, Aug. 2015, doi: 10.1021/acs.macromol.5b01064.
 - [79] Y. Yang, “Sensitivity of nanoindentation strain rate in poly(ester-ester-ketone) using atomic force microscopy,” *Polym. Test.*, vol. 53, pp. 85–88, 2016, doi: 10.1016/j.polymertesting.2016.05.013.
-

-
- [80] D. Tranchida, S. Piccarolo, and M. Soliman, “Nanoscale mechanical characterization of polymers by AFM nanoindentations: critical approach to the elastic characterization,” *Macromolecules*, vol. 39, pp. 4547–4556, Jun. 2006, doi: 10.1021/ma052727j.
- [81] D. Tranchida, Z. Kiflie, and S. Piccarolo, “Viscoelastic recovery behavior following atomic force microscope nanoindentation of semicrystalline poly(ethylene),” *Macromolecules*, vol. 40, pp. 7366–7371, 2007, doi: 10.1021/ma070682b.
- [82] M. Lei, B. Xu, Y. Pei, H. Lu, and Y. Q. Fu, “Micro-mechanics of nanostructured carbon/shape memory polymer hybrid thin film,” *Soft Matter*, vol. 12, no. 1, pp. 106–114, 2015, doi: 10.1039/c5sm01269d.
- [83] I. Karapanagiotis and W. W. Gerberich, “Curvature Driven Flow of Thin Polymer Films and Diffusivity Measurements,” *Macromolecules*, vol. 38, no. 8, pp. 3420–3425, Apr. 2005, doi: 10.1021/ma048216z.
- [84] I. Karapanagiotis, D. F. Evans, and W. W. Gerberich, “Leveling and Dewetting Processes of Nanoindentation-Induced Defects on Thin Polymer Films,” *Macromolecules*, vol. 34, no. 11, pp. 3741–3747, May 2001, doi: 10.1021/ma001762h.
- [85] A. M. Díez-Pascual, M. A. Gómez-Fatou, F. Ania, and A. Flores, “Nanoindentation in polymer nanocomposites,” *Prog. Mater. Sci.*, vol. 67, pp. 1–94, Jan. 2015, doi: 10.1016/j.pmatsci.2014.06.002.
- [86] G. Mallikarjunachari and P. Ghosh, “Pile-up response of polymer thin films to static and dynamic loading,” *Thin Solid Films*, vol. 677, pp. 1–12, 2019, doi: 10.1016/j.tsf.2019.01.040.
- [87] C. A. Tweedie and K. J. van Vliet, “On the indentation recovery and fleeting hardness of polymers,” *J. Mater. Res.*, vol. 21, no. 12, pp. 3029–3036, Dec. 2006, doi: 10.1557/jmr.2006.0377.
- [88] H. Lu, B. Wang, J. Ma, G. Huang, and H. Viswanathan, “Measurement of Creep Compliance of Solid Polymers by Nanoindentation,” *Mech. Time-Dependent Mater.*, vol. 7, no. 3/4, pp. 189–207, 2003, doi: 10.1023/B:MTDM.0000007217.07156.9b.
- [89] B. J. Briscoe, L. Fiori, and E. Pelillo, “Nano-indentation of polymeric surfaces,” *J. Phys. D. Appl. Phys.*, vol. 31, no. 19, pp. 2395–2405, Oct. 1998, doi: 10.1088/0022-3727/31/19/006.
- [90] K. L. Johnson, “The correlation of indentation experiments,” *J. Mech. Phys. Solids*, vol. 18, pp. 115–126, 1970, doi: 10.1016/0022-5096(70)90029-3.
-

- [91] G. Z. Voyiadjis and L. Malekmoitei, "Variation of the strain rate during CSM nanoindentation of glassy polymers and its implication on indentation size effect," *J. Polym. Sci. Part B Polym. Phys.*, pp. 1–9, 2016, doi: 10.1002/polb.24127.
 - [92] G. Z. Voyiadjis, L. Malekmoitei, and A. Samadi-Dooki, "Indentation size effect in amorphous polymers based on shear transformation mediated plasticity," *Polymer (Guildf)*, vol. 137, pp. 72–81, 2018, doi: 10.1016/j.polymer.2018.01.006.
 - [93] G. Peng, T. Zhang, Y. Feng, and Y. Huan, "Determination of shear creep compliance of linear viscoelastic-plastic solids by instrumented indentation," *Polym. Test.*, vol. 31, no. 8, pp. 1038–1044, Dec. 2012, doi: 10.1016/j.polymertesting.2012.07.007.
 - [94] C.-K. Liu, S. Lee, L.-P. Sung, and T. Nguyen, "Load-displacement relations for nanoindentation of viscoelastic materials," *J. Appl. Phys.*, vol. 100, no. 3, Aug. 2006, doi: 10.1063/1.2220649.
 - [95] J. Giró-Paloma *et al.*, "Depth-sensing indentation applied to polymers: A comparison between standard methods of analysis in relation to the nature of the materials," *Eur. Polym. J.*, vol. 49, no. 12, pp. 4047–4053, 2013, doi: 10.1016/j.eurpolymj.2013.09.010.
 - [96] M. Alderighi, V. Ierardi, F. Fusco, M. Allegrini, and R. Solaro, "Size effects in nanoindentation of hard and soft surfaces," *Nanotechnology*, vol. 20, no. 23, pp. 235703-1–9, 2009, doi: 10.1088/0957-4484/20/23/235703.
 - [97] F. J. Balta Calleja, A. Flores, and G. H. Michler, "Microindentation studies at the near surface of glassy polymers: influence of molecular weight," *J. Appl. Polym. Sci.*, vol. 93, pp. 1951–1956, 2004, doi: 10.1002/app.20665.
 - [98] A. C. M. Chong and D. C. C. Lam, "Strain gradient plasticity effect in indentation hardness of polymers," *J. Mater. Res.*, vol. 14, no. 10, pp. 4103–4110, 1999, doi: <https://doi.org/10.1557/JMR.1999.0554>.
 - [99] T. Jin, Z. Zhou, Z. Liu, G. Xiao, G. Yuan, and X. Shu, "Sensitivity of PMMA nanoindentation measurements to strain rate," *J. Appl. Polym. Sci.*, vol. 132, no. 17, pp. 1–5, 2015, doi: 10.1002/app.41896.
 - [100] R. W. Snyder and P. C. Painter, "Dynamic fourier transform-IR analysis of cure reactions and kinetics of polyimides," in *Polymeric Materials for Electronics Packaging and Interconnection*, 1989, pp. 49–56. doi: 10.1021/bk-1989-0407.ch003.
 - [101] C. A. Pryde, "IR studies of polyimides. I. Effects of chemical and physical changes during
-

- cure,” *J. Polym. Sci. Part A Polym. Chem.*, vol. 27, pp. 711–724, 1989, doi: 10.1002/pola.1989.080270229.
- [102] S. Verma, P. Sarkar, and P. Pant, “Thermal drift in room temperature nanoindentation experiments: measurement and correction,” *J. Mater. Res.*, vol. 36, pp. 3436–3444, Sep. 2021, doi: 10.1557/s43578-021-00386-0.
- [103] M. S. Bobji and S. K. Biswas, “Estimation of hardness nanoindentation of rough surfaces,” *J. Mater. Res.*, vol. 13, p. 1998, 2014, doi: 10.1557/JMR.1998.0438.
- [104] J. Wang *et al.*, “Thickness dependence of elastic modulus and hardness of on-wafer low-k ultrathin polytetrafluoroethylene films,” *Scr. Mater.*, vol. 42, pp. 687–694, 2000, doi: [https://doi.org/10.1016/S1359-6462\(99\)00421-2](https://doi.org/10.1016/S1359-6462(99)00421-2).
- [105] J. Malzbender and G. de With, “The use of the indentation loading curve to detect fracture of coatings,” *Surf. Coatings Technol.*, vol. 137, pp. 72–76, 2001, doi: [https://doi.org/10.1016/S0257-8972\(00\)01091-4](https://doi.org/10.1016/S0257-8972(00)01091-4).
- [106] F. Carrillo *et al.*, “Nanoindentation of polydimethylsiloxane elastomers: effect of crosslinking, work of adhesion, and fluid environment on elastic modulus,” *J. Mater. Res.*, vol. 20, pp. 2820–2830, 2005, doi: 10.1557/JMR.2005.0354.
- [107] S. Gupta, F. Carrillo, C. Li, L. Pruitt, and C. Puttlitz, “Adhesive forces significantly affect elastic modulus determination of soft polymeric materials in nanoindentation,” *Mater. Lett.*, vol. 61, pp. 448–451, 2007, doi: 10.1016/j.matlet.2006.04.078.
- [108] A. J. Wrucke, C. S. Han, and P. Majumdar, “Indentation size effect of multiple orders of magnitude in polydimethylsiloxane,” *J. Appl. Polym. Sci.*, vol. 128, pp. 258–264, 2013, doi: 10.1002/app.38161.
- [109] A. T. Al-Halhouli, I. Kampen, T. Krah, and S. Büttgenbach, “Nanoindentation testing of SU-8 photoresist mechanical properties,” *Microelectron. Eng.*, vol. 85, no. 5–6, pp. 942–944, May 2008, doi: 10.1016/j.mee.2008.01.033.
- [110] S. Kim, “Photoresist Passivation Structures for Laser Lifted-Off Light Emitting Diodes,” *Electrochem. Solid-State Lett.*, vol. 13, no. 7, p. H240, 2010, doi: 10.1149/1.3416375.
- [111] O. Casals and J. Alcalá, “Analytical and experimental resolutions in the duality of mechanical property extractions from instrumented indentation experiments: Comments on “On determination of material parameters from loading and unloading responses in nanoindentation with a single,” *J. Mater. Res.*, vol. 22, no. 5, pp. 1138–1144, 2007, doi:
-

10.1557/jmr.2007.0182.

- [112] S. Y. Chang, *In-situ nanomechanical testing in electron microscopes*. 2019. doi: 10.1007/978-981-10-6884-3_53.
 - [113] J. K. J. K. Deuschle, G. Buerki, H. M. M. Deuschle, S. Enders, J. Michler, and E. Arzt, “In situ indentation testing of elastomers,” *Acta Mater.*, vol. 56, no. 16, pp. 4390–4401, 2008, doi: 10.1016/j.actamat.2008.05.003.
 - [114] A. Z. Juri, A. K. Basak, and L. Yin, “Microstructural responses of Zirconia materials to in-situ SEM nanoindentation,” *J. Mech. Behav. Biomed. Mater.*, vol. 118, p. 104450, 2021, doi: 10.1016/j.jmbbm.2021.104450.
 - [115] H. Nili, K. Kalantar-Zadeh, M. Bhaskaran, and S. Sriram, “In situ nanoindentation: Probing nanoscale multifunctionality,” *Prog. Mater. Sci.*, vol. 58, pp. 1–29, 2013, doi: 10.1016/j.pmatsci.2012.08.001.
 - [116] J. M. Wheeler, R. Raghavan, and J. Michler, “In situ SEM indentation of a Zr-based bulk metallic glass at elevated temperatures,” *Mater. Sci. Eng. A*, vol. 528, no. 29–30, pp. 8750–8756, 2011, doi: 10.1016/j.msea.2011.08.057.
 - [117] “We employ usage days as a measure, because over the intervals we have considered, the usage is uniform in terms of type of material indented, number of indents, etc.”.
 - [118] M. Beyaoui, P. E. P. E. Mazeran, M. F. M. F. Arvieu, M. Bigerelle, and M. Guigon, “Analysis of nanoindentation curves in the case of bulk amorphous polymers,” *Int. J. Mater. Res.*, vol. 100, no. 7, pp. 943–949, 2009, doi: 10.3139/146.110137.
 - [119] Y. Y. Lim and M. Munawar Chaudhri, “Indentation of elastic solids with a rigid Vickers pyramidal indenter,” *Mech. Mater.*, vol. 38, no. 12, pp. 1213–1228, Dec. 2006, doi: 10.1016/j.mechmat.2006.04.006.
 - [120] A. E. Giannakopoulos, “Elastic and viscoelastic indentation of flat surfaces by pyramid indentors,” *J. Mech. Phys. Solids*, vol. 54, pp. 1305–1332, 2006, doi: 10.1016/j.jmps.2006.01.011.
 - [121] R. F. Cook and M. L. Oyen, “Nanoindentation behavior and mechanical properties measurement of polymeric materials,” *Zeitschrift fuer Met. Res. Adv. Tech.*, vol. 98, no. 5, pp. 370–378, 2007.
 - [122] M. L. Oyen and R. F. Cook, “Load–displacement behavior during sharp indentation of
-

- viscous–elastic–plastic materials,” *J. Mater. Res.*, vol. 18, no. 1, pp. 139–150, Jan. 2003, doi: 10.1557/JMR.2003.0020.
- [123] N. M. Ames, V. Srivastava, S. A. Chester, and L. Anand, “A thermo-mechanically coupled theory for large deformations of amorphous polymers. Part II: Applications,” *Int. J. Plast.*, vol. 25, no. 8, pp. 1495–1539, 2009, doi: 10.1016/j.ijplas.2008.11.005.
- [124] Z. El-Qoubaa, L. Colard, R. Matadi Boumbimba, and A. Rusinek, “Experimental Study and Modelling of Poly (Methyl Methacrylate) and Polycarbonate Compressive Behavior from Low to High Strain Rates,” *J. Dyn. Behav. Mater.*, vol. 4, no. 2, pp. 179–189, 2018, doi: 10.1007/s40870-018-0147-5.
- [125] P. Yu, X. Yao, Q. Han, S. Zang, and Y. Gu, “A visco-elastoplastic constitutive model for large deformation response of polycarbonate over a wide range of strain rates and temperatures,” *Polymer (Guildf.)*, vol. 55, no. 25, pp. 6577–6593, Dec. 2014, doi: 10.1016/j.polymer.2014.09.071.
- [126] H. Zhu, H. Ou, and A. Popov, “A new phenomenological constitutive model for thermoplastics,” *Mech. Mater.*, vol. 157, p. 103817, 2021, doi: 10.1016/j.mechmat.2021.103817.
- [127] S. Chung and S. Park, “Effects of temperature on mechanical properties of SU-8 photoresist material,” *J. Mech. Sci. Technol.*, vol. 27, pp. 2701–2707, 2013, doi: 10.1007/s12206-013-0714-6.
- [128] M. M. Chaudhri, “The love equation for the normal loading of a rigid cone on an elastic half-space and a recent modification: A review,” *Mater. Trans.*, vol. 60, pp. 1404–1410, 2019, doi: 10.2320/matertrans.MD201908.
- [129] M. M. Chaudhri, “The Love Equation for the Normal Loading of a Rigid Cone on an Elastic Half-Space and a Recent Modification: A Review,” *Mater. Trans.*, vol. 60, no. 8, pp. 1404–1410, Jul. 2019, doi: 10.2320/matertrans.MD201908.
- [130] M. M. Chaudhri, “The Love equation for the normal loading of a rigid cone on an elastic half-space: no need for a modification,” *Philos. Mag. Lett.*, vol. 97, pp. 343–349, 2017, doi: 10.1080/09500839.2017.1361554.
- [131] Y. Y. Lim † and M. M. Chaudhri ‡, “Indentation of elastic solids with rigid cones,” *Philos. Mag.*, vol. 84, no. 27, pp. 2877–2903, Sep. 2004, doi: 10.1080/14786430410001716782.
- [132] M. S. R. N. Kiran, B. Haberl, J. S. Williams, and J. E. Bradby, “Temperature dependent
-

- deformation mechanisms in pure amorphous silicon,” *J. Appl. Phys.*, vol. 115, no. 11, p. 113511, Mar. 2014, doi: 10.1063/1.4869136.
- [133] S. Z. Chavoshi and S. Xu, “Temperature-dependent nanoindentation response of materials,” *MRS Commun.*, vol. 8, no. 1, pp. 15–28, Mar. 2018, doi: 10.1557/mrc.2018.19.
- [134] J. E. Jakes and D. Stauffer, “Contact area correction for surface tilt in pyramidal nanoindentation,” *J. Mater. Res.*, vol. 36, no. 11, pp. 2189–2197, Jun. 2021, doi: 10.1557/s43578-021-00119-3.
- [135] C. Li and A. Strachan, “Free volume evolution in the process of epoxy curing and its effect on mechanical properties,” *Polymer (Guildf)*, vol. 97, pp. 456–464, Aug. 2016, doi: 10.1016/j.polymer.2016.05.059.
- [136] G. Feng and A. H. W. Ngan, “Effects of creep and thermal drift on modulus measurement using depth-sensing indentation,” *J. Mater. Res.*, vol. 17, no. 3, pp. 660–668, 2002, doi: 10.1557/JMR.2002.0094.
- [137] F. Lapique and K. Redford, “Curing effects on viscosity and mechanical properties of a commercial epoxy resin adhesive,” *Int. J. Adhes. Adhes.*, vol. 22, no. 4, pp. 337–346, Jan. 2002, doi: 10.1016/S0143-7496(02)00013-1.
- [138] S. L. Simon, G. B. McKenna, and O. Sindt, “Modeling the evolution of the dynamic mechanical properties of a commercial epoxy during cure after gelation,” *J. Appl. Polym. Sci.*, vol. 76, no. 4, pp. 495–508, Apr. 2000, doi: 10.1002/(SICI)1097-4628(20000425)76:4<495::AID-APP7>3.0.CO;2-B.
- [139] M. Hojjati, A. Johnston, S. V. Hoa, and J. Denault, “Viscoelastic behavior of Cytec FM73 adhesive during cure,” *J. Appl. Polym. Sci.*, vol. 91, no. 4, pp. 2548–2557, Feb. 2004, doi: 10.1002/app.13416.
- [140] M. Aldridge, A. Wineman, A. Waas, and J. Kieffer, “In Situ Analysis of the Relationship between Cure Kinetics and the Mechanical Modulus of an Epoxy Resin,” *Macromolecules*, vol. 47, no. 23, pp. 8368–8376, Dec. 2014, doi: 10.1021/ma501441c.
- [141] Y. Zhang, Z. Chen, H. Zheng, R. Chen, C. Ma, and G. Zhang, “Multifunctional hard yet flexible coatings fabricated using a universal step-by-step strategy,” *Adv. Sci.*, vol. 2200268, pp. 1–10, 2022, doi: 10.1002/advs.202200268.
- [142] W. D. Zhang, L. Shen, I. Y. Phang, and T. Liu, “Carbon nanotubes reinforced nylon-6 composite prepared by simple melt-compounding,” *Macromolecules*, vol. 37, no. 2, pp. 256–
-

259, 2004, doi: 10.1021/ma035594f.

- [143] J. Moosburger-Will, M. Greisel, M. G. R. M. G. R. Sause, R. Horny, and S. Horn, “Influence of partial cross-linking degree on basic physical properties of RTM6 epoxy resin,” *J. Appl. Polym. Sci.*, vol. 130, no. 6, pp. 4338–4346, Jul. 2013, doi: 10.1002/app.39722.
 - [144] W. H. Poisl, W. C. Oliver, and B. D. Fabes, “The relationship between indentation and uniaxial creep in amorphous selenium,” *J. Mater. Res.*, vol. 10, pp. 2024–2032, 1995, doi: <https://doi.org/10.1557/JMR.1995.2024>.
 - [145] N. A. Stilwell and D. Tabor, “Elastic recovery of conical indentations,” *Proc. Phys. Soc.*, vol. 78, pp. 169–179, 1961, doi: 10.1088/0370-1328/78/2/302.
 - [146] A. Mokhtari, N. Tala-Ighil, and Y. A. Masmoudi, “Nanoindentation to Determine Young’s Modulus for Thermoplastic Polymers,” *J. Mater. Eng. Perform.*, vol. 31, pp. 2715–2722, Apr. 2022, doi: 10.1007/s11665-021-06386-9.
 - [147] J. S. Field and M. V Swain, “A simple predictive model for spherical indentation,” *J. Mater. Res.*, vol. 8, no. 2, pp. 297–306, 1993, doi: 10.1557/JMR.1993.0297.
 - [148] D. Tabor, *The Hardness of Metals*. New York, NY: Clarendon Press, 1951.
 - [149] S. M. P. Kalaiselvi, T. L. Tan, R. S. Rawat, P. Lee, S. P. Heussler, and M. B. H. Breese, “FTIR spectroscopic studies on cross linking of SU-8 photoresist,” *Cosmos*, vol. 9, pp. 37–46, 2013, doi: 10.1142/s021960771350002x.
 - [150] K. M. Gunde, N. Hauptman, M. Maček, and M. Kunaver, “The influence of hard-baking temperature applied for SU8 sensor layer on the sensitivity of capacitive chemical sensor,” *Appl. Phys. A Mater. Sci. Process.*, vol. 95, pp. 673–680, 2009, doi: 10.1007/s00339-008-4966-4.
 - [151] D. I. Bower and W. F. Maddams, *The Vibrational Spectroscopy of Polymers*. Cambridge: Cambridge University Press, 1989. doi: 10.1017/CBO9780511623189.
 - [152] F. Alisafaei and C.-S. Han, “Indentation Depth Dependent Mechanical Behavior in Polymers,” *Adv. Condens. Matter Phys.*, vol. 2015, pp. 1–20, 2015, doi: 10.1155/2015/391579.
 - [153] Hysitron, “TI Premier User Manual: Revision 9.4.0914,” pp. 1–349, 2014.
-

Supporting Information:

**Physical phenomena during nanoindentation deformation of
amorphous glassy polymers**

Prakash Sarkar¹, Prita Pant¹, Hemant Nanavati^{2*}

¹Department of Metallurgical Engineering and Materials Science, Indian Institute of Technology
Bombay, Mumbai- 400076, Maharashtra, India

²Department of Chemical Engineering, Indian Institute of Technology Bombay, Mumbai- 400076,
Maharashtra, India

*E-mail: hnanavati@iitb.ac.in

Supporting Information 1

S.1.1. h vs P unload curve, GPL fitting parameters

The generalized power law (GPL) fitting has been described in [Section 5.1.2](#). The corresponding fitted values are listed in Table S.1.1.

Table S.1.1: **GPL fitted constants and their ranges.**

Sample	P_m (μN)	k_0	k_1	k_2	1/ m (Value or range)	
					$h = gP^{D_{IF}/F} + h_{ne}$	$P = B(h - h_f)^m$
PB05	1000	8.15 ± 0.47	-2.21 ± 0.01	0.16 ± 0.01	0.46 to 0.64	0.26
	9000	11.02 ± 0.30	-2.35 ± 0.07	0.13 ± 0.00	0.45 to 0.57	0.27
HB15	1000	7.94 ± 0.76	-2.20 ± 0.23	0.16 ± 0.02	0.48 to 0.62	0.33
	9000	9.55 ± 0.65	-1.96 ± 0.15	0.11 ± 0.01	0.40 to 0.56	0.34
PC	1000	5.12 ± 0.74	-1.28 ± 0.22	0.09 ± 0.02	0.46 to 0.62	0.35
	9000	8.74 ± 0.67	-1.80 ± 0.14	0.10 ± 0.01	0.45 to 0.59	0.36
PMMA	1000	1.51 ± 0.01	-0.13 ± 0.01	--	0.65 to 0.79	0.52
	9000	0.89 ± 0.01	-0.03 ± 0.01	--	0.57 to 0.60	0.54

h_f values in all the literature methods are fitted values. They are either unphysical or significantly lower than the experimental values (Table S.1.2).

Table S.1.2: **Experimental and fitted h_f (nm) values, via various methods.**

References	P_m (μN)	PB05	HB15	PC	PMMA
Oliver-Pharr [1]	1000	68 ± 3	117 ± 1	248 ± 5	321 ± 5
	9000	320 ± 15	504 ± 7	933 ± 16	1033 ± 9
Kossmann <i>et al.</i> [2]	1000	9 ± 6	-199 ± 18	97 ± 4	321 ± 6
	9000	93 ± 34	-1177 ± 26	443 ± 18	1033 ± 9
Liu <i>et al.</i> [3]	1000	$-1.8\text{E}6 \pm 1.7\text{E}6$	$-3.2\text{E}6 \pm 2.4\text{E}6$	$-3.2\text{E}6 \pm 0.5\text{E}6$	$1.1\text{E}6 \pm 1.5\text{E}6$
	9000	$1.5\text{E}6 \pm 1.8\text{E}6$	$-7.0\text{E}6 \pm 0.5\text{E}6$	$-19.1\text{E}6 \pm 7.0\text{E}6$	$7.9\text{E}6 \pm 2.5\text{E}6$
Experimental values	1000	191 ± 1	172 ± 1	300 ± 3	304 ± 7
	9000	529 ± 15	473 ± 7	983 ± 15	904 ± 4

Supporting Information 2

S.2.1. h vs P unload curves with GPL fitting

We have seen that the GPL framework describes well, the relationship between $h - h_{ne}$ and P , over the entire constant unload rate range, as shown in Fig. S.2.1, Fig. S.2.2(a)-(b), Fig. S.2.3(a)-(b) and Fig. S.2.4(a)-(b), for PB05, HB15, PC and PMMA, respectively. We find that the relative residuals of this fitted equation are small, scattered and random (up to $\sim 0.03\%$), with $R^2 \sim 0.999$.

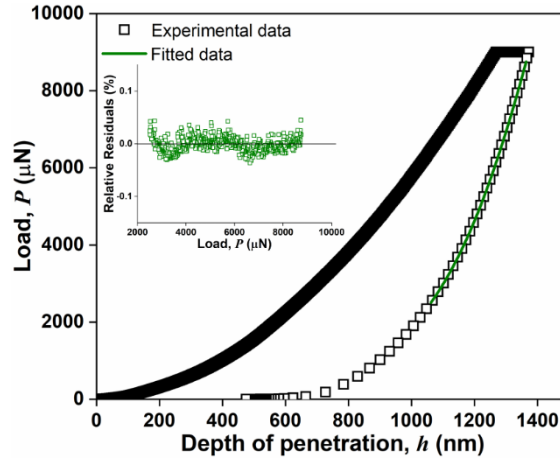


Figure S.2.1: P - h curves for PB05 for $P_m = 9000 \mu\text{N}$. Unloading curve fitted to GPL equation.

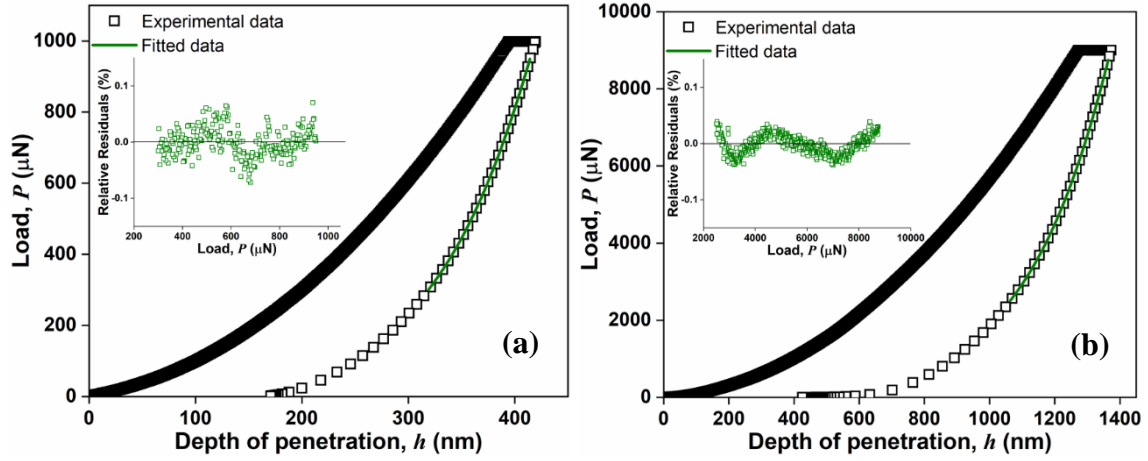


Figure S.2.2: P - h curves for HB15 for $P_m =$ (a) $1000 \mu\text{N}$, (b) $9000 \mu\text{N}$. Unloading curve fitted to GPL equation.

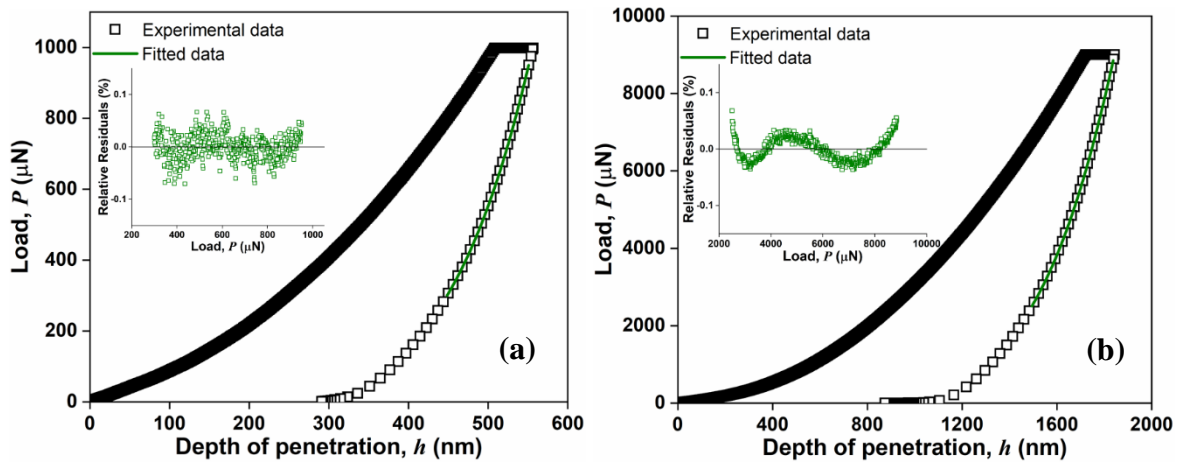


Figure S.2.3: P - h curves for PC for $P_m =$ (a) $1000 \mu\text{N}$, (b) $9000 \mu\text{N}$. Unloading curve fitted to GPL equation.

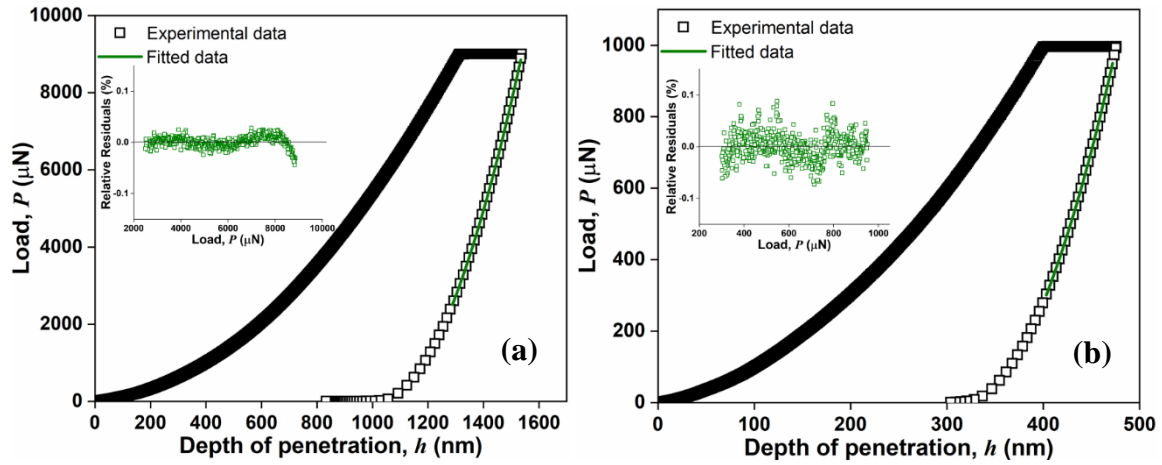


Figure S.2.4: P - h curves for PMMA for $P_m =$ (a) 1000 μN , (b) 9000 μN . Unloading curve fitted to GPL equation.

Supporting Information 4

S.4.1. SPM images of residual imprints

The SPM top view image to compute A_c , are presented on PB05 for $P_m = 9000 \mu\text{N}$ (Fig. S.4.1), on HB15 for $P_m = 1000 \mu\text{N}$ (Fig. S.4.2(a)), for $P_m = 9000 \mu\text{N}$ (Fig. S.4.2(b)), on PC for $P_m = 1000 \mu\text{N}$ (Fig. S.4.3(a)), for $P_m = 9000 \mu\text{N}$ (Fig. S.4.3(b)), and on PMMA for $P_m = 1000 \mu\text{N}$ (Fig. S.4.4(a)), for $P_m = 9000 \mu\text{N}$ (Fig. S.4.4(b)).

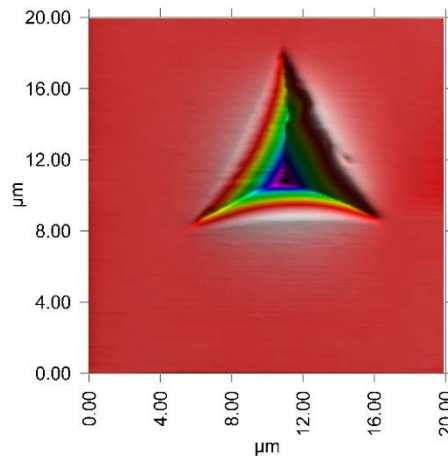


Figure S.4.1: Top view of residual imprint of PB05 for $P_m = 9000 \mu\text{N}$.

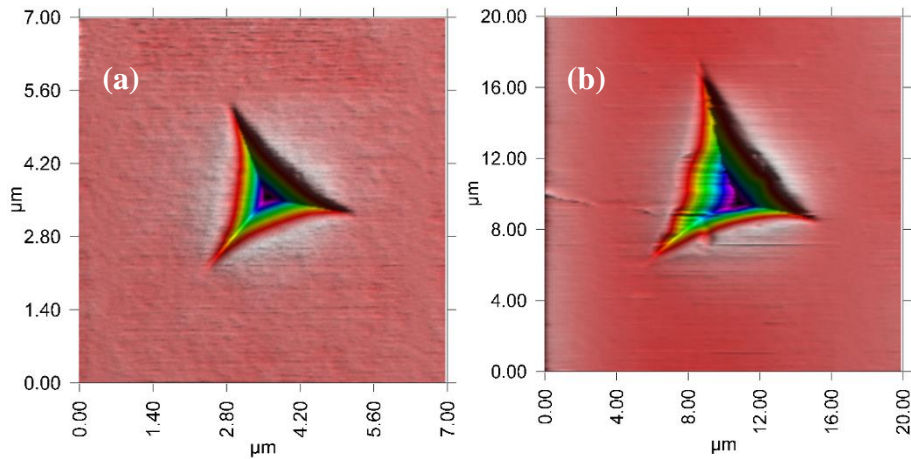


Figure S.4.2: Top view of residual imprint of HB15 for $P_m =$ (a) $1000 \mu\text{N}$, (b) $9000 \mu\text{N}$.

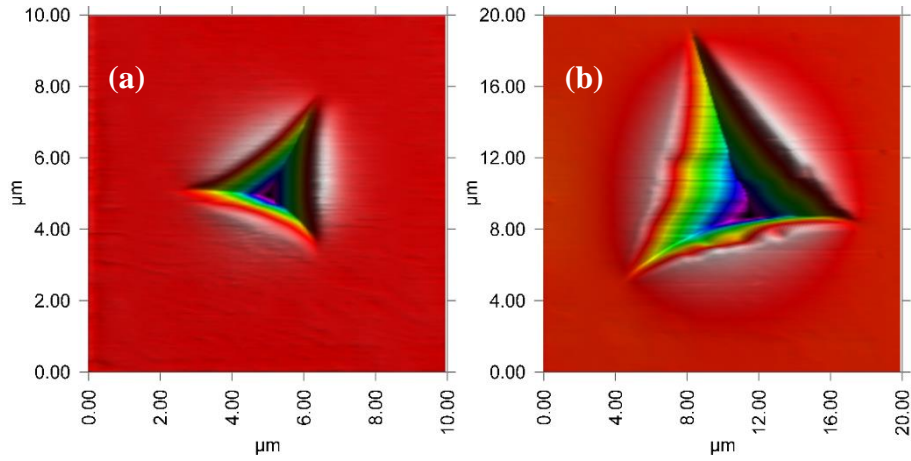


Figure S.4.3: Top view of residual imprint of PC for $P_m =$ (a) 1000 μN , (b) 9000 μN .

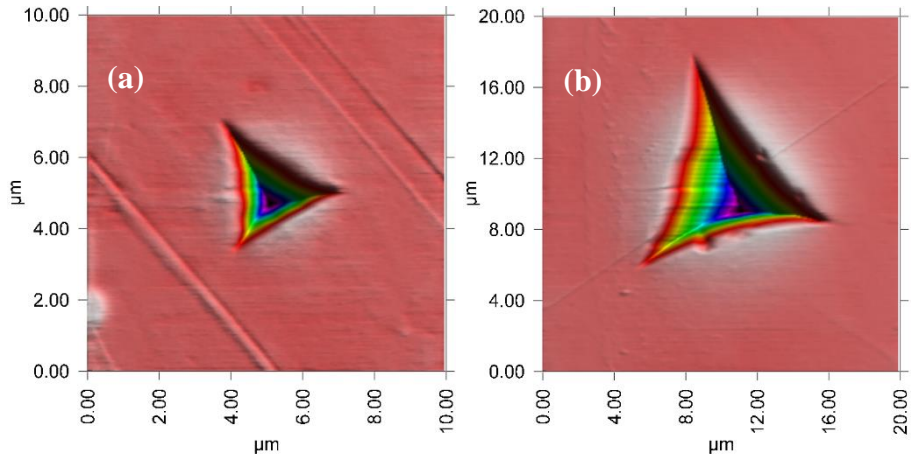


Figure S.4.4: Top view of residual imprint of PMMA for $P_m =$ (a) 1000 μN , (b) 9000 μN .

S.4.2. Location of maximum pile-up

The maximum pile-up is located beyond the α -line, and beyond geometric contact, can be inferred from the magnified version of Fig. 7(a), is shown in Fig. S.4.5.

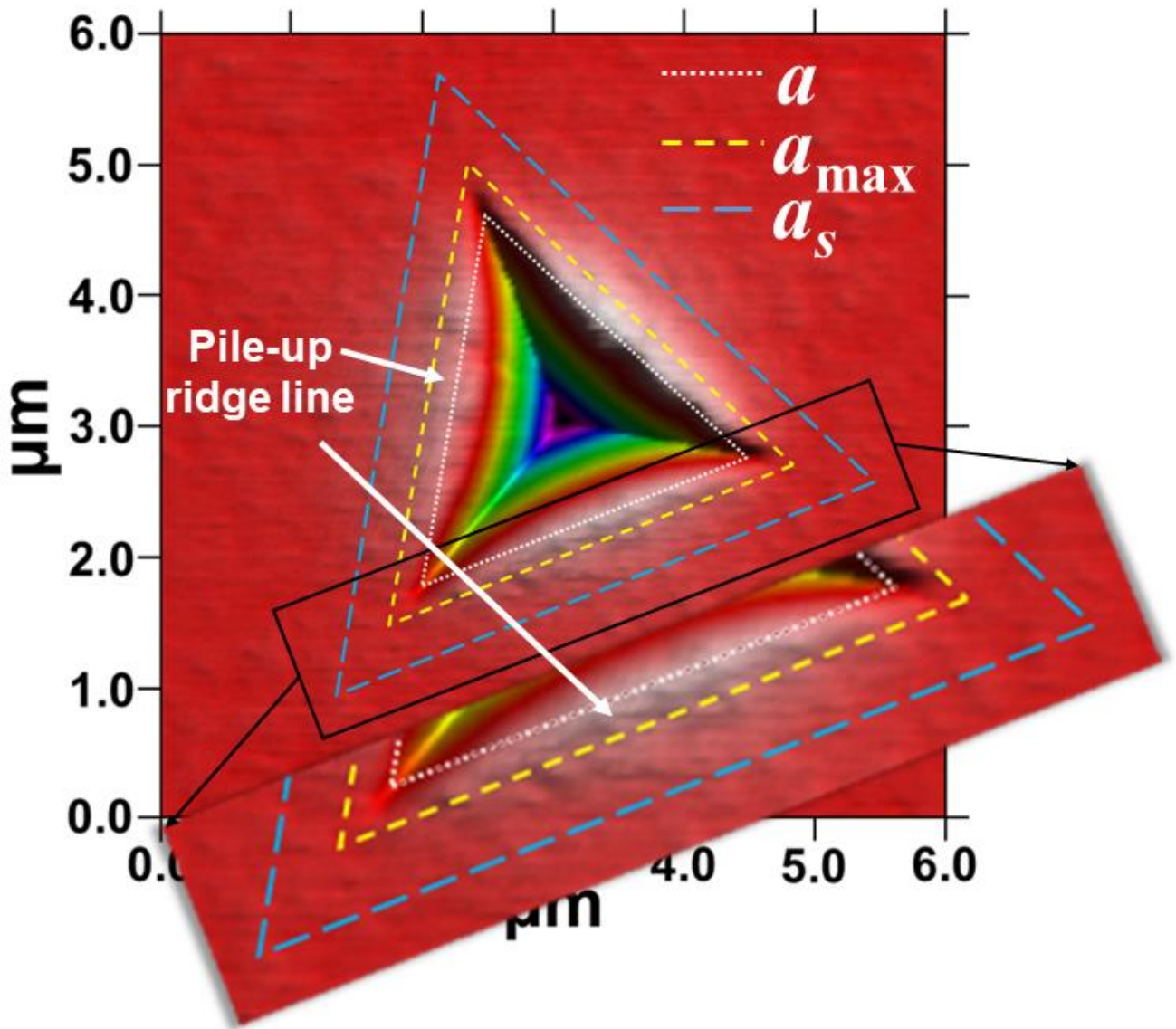


Figure S.4.5: Top view of residual imprint of PB05 for $P_m = 1000 \mu\text{N}$. The maximum pile-up (Ridge-line) is beyond the a -line.

Supporting Information 5

S.5.1. Uniform h_s during nanoindentation for an elastic medium

The mapping of the nanoindentation via a perfectly conical indenter to Berkovich nanoindentation has been described in [Section 5.3.3](#). The interpretation in Fig. S.5.1 retains the assumption of the effective circular cross-section, in providing the ideal h_s estimate (eqn. 6). We consider a uniform sink-in during purely elastic nanoindentation, all about the triangle's perimeter.

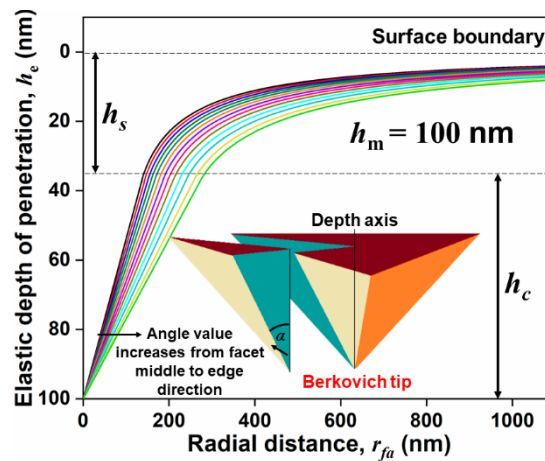


Figure S.5.1: Deformation profile at different angles from the facet middle direction to edge direction, for an elastic medium. Here, $h_m = 100$ nm and the cone angle increase from 65.27° to 77.03° .

S.5.2. Radial shift during deformation

Figure S.5.2 illustrates the inward (radial) surface displacement as discussed in [Section 5.3.3](#).

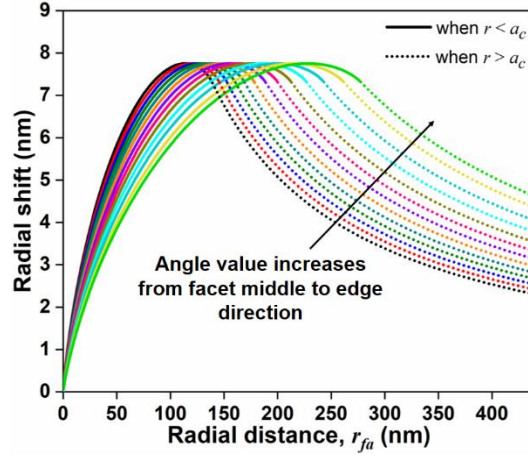


Figure S.5.2: Radial shift when $r < a_c$ (solid line) and $r > a_c$ (dotted line) from the facet middle direction to the edge direction, for an elastic medium, following eqn. 5 and eqn. 7. Here, $h_m = 100$ nm, $\nu = 0.35$, and the cone angle increases from 65.27° to 77.03° .

S.5.3. h_s estimation from S^{GPL}

We know that [4], for purely elastic deformation, $h_c/h_m = 2/\pi$

$$\Rightarrow \frac{h_c - h_{ne}}{h_m - h_{ne}} = \frac{2}{\pi} \quad (\text{Corresponding to the elastic contribution to the total deformation})$$

$$\Rightarrow 1 - \frac{h_c - h_{ne}}{h_m - h_{ne}} = 1 - \frac{2}{\pi}, \Rightarrow \frac{h_m - h_c}{h_m - h_{ne}} = \frac{h_s}{h_m - h_{ne}} = \frac{\pi - 2}{\pi}$$

$$h_s = \frac{\pi - 2}{\pi} (h_m - h_{ne}) \quad \text{eqn. S.5.1}$$

$$\text{From eqn. 2 and eqn. 3, } S^{\text{GPL}} = \left(\frac{h_m - h_{ne}}{P_m} \frac{dD}{dF} \right)^{-1}, \Rightarrow h_m - h_{ne} = \left(\frac{S^{\text{GPL}}}{P_m} \frac{dD}{dF} \right)^{-1}$$

Combining with eqn. S.5.1,

$$\Rightarrow h_s^{\text{GPL}} = \frac{\pi - 2}{\pi} \left(\frac{S^{\text{GPL}}}{P_m} \frac{dD_i}{dF} \right)^{-1} \quad \text{eqn. S.5.2}$$

Supplementary Information 6

S.6.1. Residual imprint analysis

As shown in Fig.S.6.1 for PB05 and HB15, SPM images indicate that the a -values (corresponding to instantaneous, permanent plastic deformation) remain unchanged even after 12 hrs. after unloading.

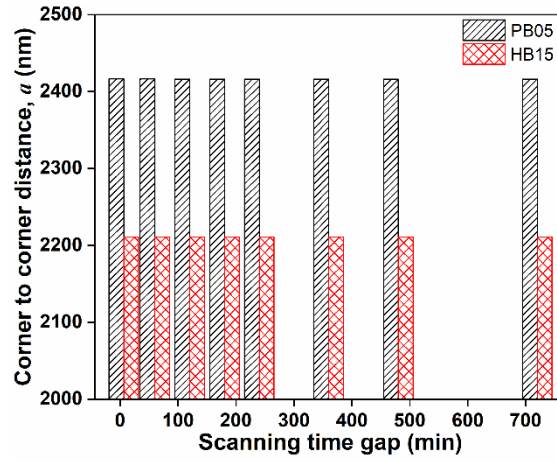


Figure S.6.1: a -line observation via SPM images over 12 hrs. duration for PB05 and HB15.

The viscoelastic variation in h^{PU} is illustrated in Fig. S.6.2(a)-(b) (PB05) and Fig. S.6.3(a)-(b) (HB15).

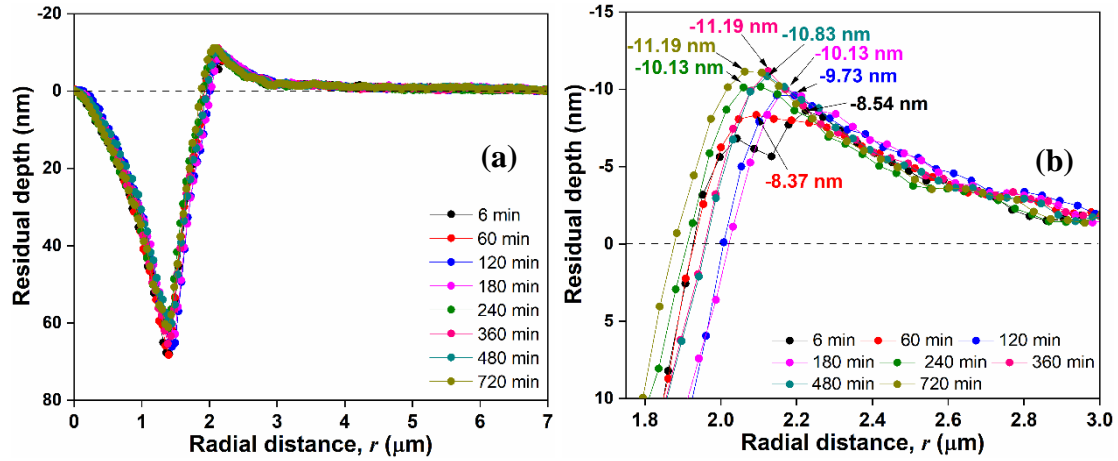


Figure S.6.2: Scan line of residual indent imprint for PB05 (a) full and (b) magnified pile-up region.

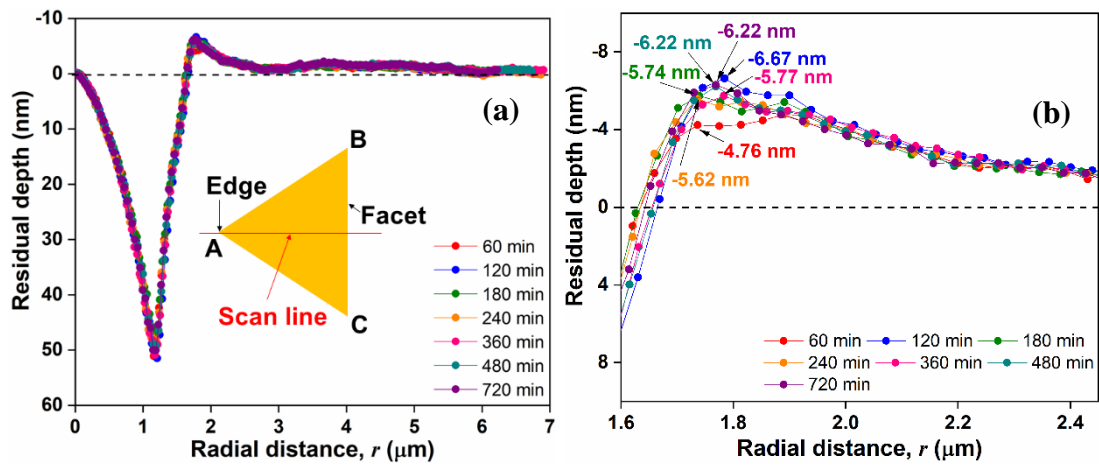


Figure S.6.3: Scan line of residual indent imprint for HB15 (a) full and (b) magnified pile-up region.

S.6.2. Corrections to Estimates of A_c

Pile-up parameters

The values for r^{PU} , η (radians), and the projected area of the elevation, A_c^{PU} , are listed in Table S.6.1.

Table S.6.1: The r^{PU} , η , and A_c^{PU} values based on various pile-up measures.

Parameters	Pile-up height (nm)	PB05		HB15		PC		PMMA	
		1000 μN	9000 μN	1000 μN	9000 μN	1000 μN	9000 μN	1000 μN	9000 μN
r^{PU} (mm)	h_c^{PU}	0.22 ± 0.06	0.73 ± 0.15	1.04 ± 0.11	1.52 ± 0.21	0.14 ± 0.05	0.99 ± 0.12	0.33 ± 0.03	3.35 ± 1.75
	$h_{\text{ne,m}}^{\text{PU}}$	0.15 ± 0.08	0.46 ± 0.05	0.34 ± 0.01	0.92 ± 0.03	0.06 ± 0.01	0.43 ± 0.04	0.28 ± 0.04	1.13 ± 0.12
	$h_{r,c}^{\text{PU}}$	0.13 ± 0.03	0.41 ± 0.08	0.54 ± 0.06	0.80 ± 0.12	0.10 ± 0.02	0.29 ± 0.08	0.13 ± 0.02	1.34 ± 0.76
	h_m^{PU}	0.08 ± 0.01	0.26 ± 0.01	0.18 ± 0.00	0.41 ± 0.05	0.04 ± 0.00	0.18 ± 0.00	0.09 ± 0.01	0.38 ± 0.02
η (radian)	h_c^{PU}	0.41 ± 0.09	0.41 ± 0.07	0.08 ± 0.01	0.19 ± 0.02	0.90 ± 0.25	0.39 ± 0.05	0.30 ± 0.03	0.12 ± 0.05
	$h_{\text{ne,m}}^{\text{PU}}$	0.57 ± 0.03	0.63 ± 0.06	0.24 ± 0.01	0.30 ± 0.01	2.03 ± 0.37	0.88 ± 0.08	0.36 ± 0.05	0.28 ± 0.03
	$h_{r,c}^{\text{PU}}$	0.69 ± 0.13	0.73 ± 0.14	0.15 ± 0.02	0.35 ± 0.05	1.25 ± 0.22	1.39 ± 0.30	0.75 ± 0.09	0.30 ± 0.13
	h_m^{PU}	1.06 ± 0.09	1.12 ± 0.03	0.46 ± 0.01	0.69 ± 0.08	2.70 ± 0.07	2.14 ± 0.06	1.10 ± 0.10	0.83 ± 0.05
A_c^{PU} (μm^2)	h_c^{PU}	0.07 ± 0.01	0.78 ± 0.13	0.01 ± 0.00	0.33 ± 0.04	0.28 ± 0.08	1.29 ± 0.14	0.07 ± 0.01	0.27 ± 0.12
	$h_{\text{ne,m}}^{\text{PU}}$	0.10 ± 0.01	1.20 ± 0.13	0.04 ± 0.00	0.53 ± 0.02	0.63 ± 0.12	2.93 ± 0.23	0.08 ± 0.01	0.64 ± 0.07
	$h_{r,c}^{\text{PU}}$	0.12 ± 0.02	1.39 ± 0.26	0.02 ± 0.00	0.62 ± 0.08	0.39 ± 0.07	4.61 ± 0.96	0.17 ± 0.02	0.69 ± 0.31
	h_m^{PU}	0.18 ± 0.02	2.13 ± 0.07	0.07 ± 0.00	1.22 ± 0.14	0.84 ± 0.01	7.13 ± 0.28	0.24 ± 0.02	1.89 ± 0.13

Tip tilt effects on contact area estimations

Since the indenter tip is attached to the holder manually, some non-zero tilt between the surface and the tip, is inevitable. Figure S.6.4 illustrates the representative effects of tip- surface tilt that we have encountered in our experiments. Instead of the imprint being an equilateral triangle, we find two limiting cases of isosceles triangles.

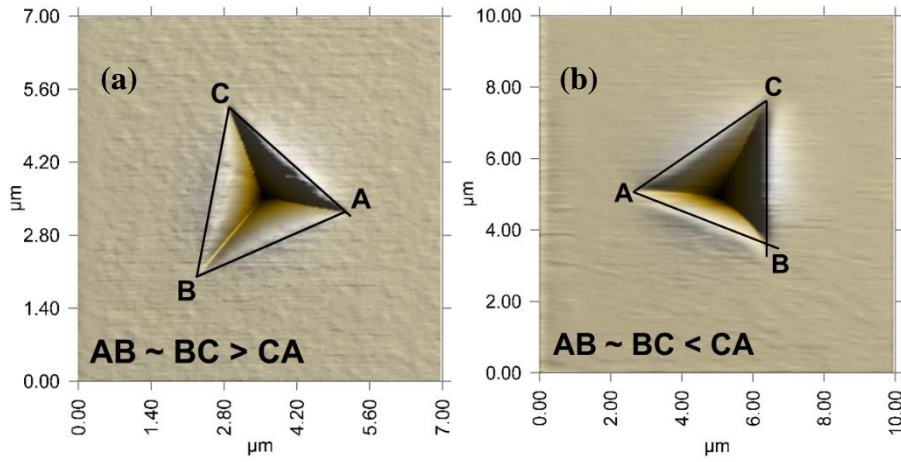


Figure S.6.4: Side edge length relation from top view SPM images for $P_m = 1000 \mu\text{N}$ for (a) PB05, (b) PC.

The quantified corrections to the A_c due to tilt, expressed in terms of the relative lengths of the imprint triangle, have been provided by Jakes *et al.* [5]. The lengths of triangle sides in our samples, deviate from equilateral values, by $\sim 3\%$ to $\sim 16\%$. These deviations result in A_c estimate corrections of $< 1\%$ for PB05 and HB15, $\sim 1.5\%$ for PC and $\sim 3\%$ for PMMA. Still, these corrections have been included here for completeness, and have been listed in Table S.6.2.

Table S.6.2: **Long side and short side ratio, and tilt correction factor when $P_m = 1000 \mu\text{N}$ and $P_m = 9000 \mu\text{N}$.**

Parameters	P_m (μN)	PB05	HB15	PC	PMMA
Side edge	1000	AB ~ BC > CA	AB ~ BC > CA	AB ~ BC < CA	AB ~ BC < CA
	9000	AB ~ BC > CA	AB ~ BC > CA	AB ~ BC > CA	AB ~ BC > CA
Long side	1000	1.074 ± 0.007	1.065 ± 0.005	1.120 ± 0.004	1.164 ± 0.009
Short side	9000	1.061 ± 0.015	1.036 ± 0.010	1.092 ± 0.016	1.140 ± 0.008
Tilt correction factor	1000	1.007	1.006	1.015	1.027
	9000	1.005	1.002	1.012	1.030

Supporting Information 7

S.7.1. Literature formulae to evaluate E_r and H

Various methods have been employed by previous researchers, to evaluate the nanoindentation properties, E_r and H . The formulae corresponding to the respective methods, are tabulated in Table S.7.1.

Table S.7.1: **Formulae to evaluate E_r and H used by previous researchers.**

References	Unload curve fitting equations	Contact area measurement equations
Oliver-Pharr [1]	$P = B(h - h_f)^m$	$h_c = h_m - (\varepsilon P_m / S); A_c = C_0 h_c^2 + \sum_{i=1}^8 C_i h_c^{2-(i-1)}$
Randall <i>et al.</i> [6]	$P = B(h - h_f)^m$	$A_c = \sqrt{3}a^2/4$
Hochstetter <i>et al.</i> [7]	$P = B(h - h_f)^m$	$A_c = C_0 \left[\zeta (h_m - (P_m / S) + h_b)^2 \right]$
Zhu <i>et al.</i> [8]	--	$A_c = 3(\pi r^2 \eta / 360) - \left[3.765k(h_m + h_m^{\text{PU}}) \right] \tan \alpha + (\sqrt{3}/4) \left[7.53(h_m + h_m^{\text{PU}}) \right]$
Hardiman <i>et al.</i> [9]	$P = B(h - h_f)^m$	$h_c = h_m - (\varepsilon P_m / S); A_c = C_0 h_c^2 + \sum_{i=1}^8 C_i h_c^{2-(i-1)}$
Kossman <i>et al.</i> [2]	$h/h_m = h_f/h_m + G(P/P_m)^m$	$h_c = h_m - (\varepsilon P_m / S); A_c = C_0 h_c^2 + \sum_{i=1}^8 C_i h_c^{2-(i-1)}$
Liu <i>et al.</i> [3]	$h = h_f + a_1 P^{1/2} + \dots + a_6 P^{1/64}$	$h_c = h_m - (\varepsilon P_m / S); A_c = C_0 h_c^2 + \sum_{i=1}^8 C_i h_c^{2-(i-1)}$
Gong <i>et al.</i> [10]	$P = P_m \left[a_0 + a_1 (h/h_m) + a_2 (h/h_m)^2 \right]$	$h_c = h_m - (\varepsilon P_m / S); A_c = C_0 h_c^2 + \sum_{i=1}^8 C_i h_c^{2-(i-1)}$

S.7.2. E_r and H estimates from literature methods

By following the formulae and methods in Table S.7.1, we have evaluated E_r and H . These estimates are listed in Table S.7.2 and Table S.7.3, respectively.

Table S.7.2: E_r estimates via methods followed by earlier researchers.

Ref.	PB05		HB15		PC		PMMA	
	1000 μN	9000 μN	1000 μN	9000 μN	1000 μN	9000 μN	1000 μN	9000 μN
[1]	5.59 ± 0.03	4.97 ± 0.06	4.74 ± 0.01	4.81 ± 0.02	3.43 ± 0.03	2.97 ± 0.03	5.32 ± 0.03	4.46 ± 0.03
[6]	5.21 ± 0.02	4.27 ± 0.02	4.71 ± 0.02	4.30 ± 0.01	3.08 ± 0.05	2.69 ± 0.02	4.87 ± 0.03	4.05 ± 0.01
[7]	5.42 ± 0.03	4.56 ± 0.05	4.65 ± 0.01	4.43 ± 0.02	3.10 ± 0.04	2.72 ± 0.03	4.72 ± 0.03	4.06 ± 0.03
[9]	4.56 ± 0.02	4.05 ± 0.04	3.86 ± 0.01	3.96 ± 0.02	2.73 ± 0.05	2.40 ± 0.02	4.49 ± 0.02	3.77 ± 0.03
[2]	5.72 ± 0.03	5.11 ± 0.06	5.17 ± 0.01	5.38 ± 0.02	3.65 ± 0.04	3.19 ± 0.03	5.33 ± 0.03	4.46 ± 0.03
[3]	5.30 ± 0.04	4.74 ± 0.05	4.89 ± 0.05	5.06 ± 0.07	3.53 ± 0.08	2.99 ± 0.03	5.35 ± 0.03	4.54 ± 0.06
[10]	5.42 ± 0.03	4.83 ± 0.06	4.82 ± 0.01	4.93 ± 0.02	3.47 ± 0.04	3.04 ± 0.03	5.34 ± 0.03	4.49 ± 0.03

Table S.7.3: H estimates via methods followed by earlier researchers.

Ref.	PB05		HB15		PC		PMMA	
	1000 μN	9000 μN	1000 μN	9000 μN	1000 μN	9000 μN	1000 μN	9000 μN
[1]	298.5 ± 3.1	278.3 ± 5.1	289.8 ± 2.3	279.3 ± 3.3	178.7 ± 3.4	143.0 ± 2.8	244.1 ± 2.0	207.9 ± 3.1
[6]	259.4 ± 1.1	206.0 ± 0.9	285.3 ± 1.0	223.0 ± 1.2	139.9 ± 2.3	117.6 ± 1.8	203.6 ± 3.3	172.2 ± 1.0
[7]	281.1 ± 3.0	235.3 ± 4.5	278.3 ± 2.4	237.2 ± 2.9	141.6 ± 4.4	119.9 ± 2.5	198.8 ± 1.6	172.8 ± 2.7
[8]	222.5 ± 2.1	174.7 ± 2.3	220.2 ± 1.2	181.5 ± 2.7	98.8 ± 1.2	86.1 ± 1.8	163.4 ± 0.8	142.0 ± 2.3
[9]	198.1 ± 1.6	185.1 ± 2.7	191.7 ± 1.0	189.0 ± 2.4	110.2 ± 1.6	93.6 ± 1.9	173.4 ± 1.0	148.5 ± 2.3
[2]	295.3 ± 3.0	274.9 ± 5.9	277.6 ± 2.3	266.4 ± 3.1	172.7 ± 3.9	139.3 ± 2.7	244.1 ± 2.0	207.7 ± 3.1
[3]	306.1 ± 3.2	284.5 ± 5.4	285.2 ± 1.2	273.1 ± 2.5	174.8 ± 3.3	142.6 ± 3.3	243.8 ± 2.1	206.5 ± 2.8
[10]	302.7 ± 3.1	281.9 ± 5.2	287.3 ± 2.4	276.2 ± 3.2	176.0 ± 3.9	141.7 ± 2.8	243.8 ± 2.0	207.3 ± 3.1

S.7.3. Deviation of E_r and H from our estimated values

Figure S.7.1 and Fig. S.7.2 indicate that the E_r and H values of the polymers examined in this work, estimated employing earlier methods, deviate up to $\sim 50\%$ from our estimates.

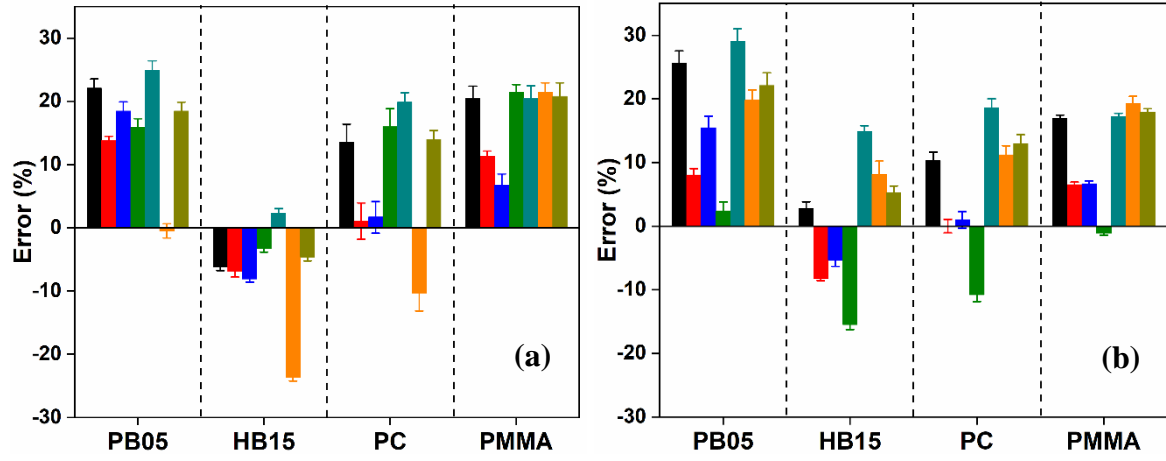


Figure S.7.1: Deviation of E_r values for $P_m =$ (a) $1000 \mu\text{N}$, (b) $9000 \mu\text{N}$. Here, ■ [1], ■ [6],

■ [7], ■ [3], ■ [2], ■ [9], ■ [10], and ■ [8].

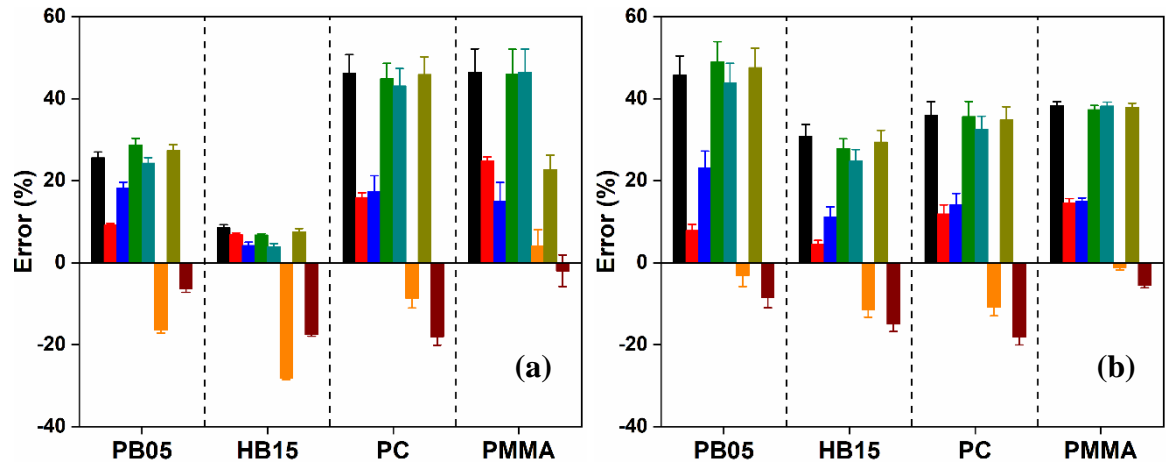


Figure S.7.2: Deviation of H values for $P_m =$ (a) $1000 \mu\text{N}$, (b) $9000 \mu\text{N}$. Here, ■ [1], ■ [6],

■ [7], ■ [3], ■ [2], ■ [9], ■ [10], and ■ [8].

References

- [1] W. C. Oliver and G. M. Pharr, “An improved technique for determining hardness and elastic modulus using load and displacement sensing indentation experiments,” *J. Mater. Res.*, vol. 7, pp. 1564–1583, 1992, doi: 10.1557/JMR.1992.0613.
 - [2] S. Kossman, T. Coorevits, A. Iost, and D. Chicot, “A new approach of the Oliver and Pharr model to fit the unloading curve from instrumented indentation testing,” *J. Mater. Res.*, vol. 32, pp. 2230–2240, 2017, doi: 10.1557/jmr.2017.120.
 - [3] E. Liu, L. Kong, G. Xiao, J. Lin, G. Zhao, and H. Li, “Creep correction of elastic modulus and hardness for viscoelastic materials during microindentation,” *Polym. Adv. Technol.*, vol. 32, pp. 955–963, 2021, doi: 10.1002/pat.5142.
 - [4] I. N. Sneddon, “Boussinesq’s problem for a rigid cone,” *Math. Proc. Cambridge Philos. Soc.*, vol. 44, no. 4, pp. 492–507, Oct. 1948, doi: 10.1017/S0305004100024518.
 - [5] J. E. Jakes and D. Stauffer, “Contact area correction for surface tilt in pyramidal nanoindentation,” *J. Mater. Res.*, vol. 36, no. 11, pp. 2189–2197, Jun. 2021, doi: 10.1557/s43578-021-00119-3.
 - [6] N. X. Randall, C. Julia-Schmutz, J. . Soro, J. von Stebut, and G. Zacharie, “Novel nanoindentation method for characterising multiphase materials,” *Thin Solid Films*, vol. 308–309, no. 1–4, pp. 297–303, Oct. 1997, doi: 10.1016/S0040-6090(97)00558-0.
 - [7] G. Hochstetter, A. Jimenez, and J. L. Loubet, “Strain-rate effects on hardness of glassy polymers in the nanoscale range. Comparison between quasi-static and continuous stiffness measurements,” *J. Macromol. Sci. Part B*, vol. 38, no. 5–6, pp. 681–692, Sep. 1999, doi: 10.1080/00222349908248131.
 - [8] L.-N. Zhu, B.-S. Xu, H.-D. Wang, and C.-B. Wang, “Determination of hardness of plasma-sprayed FeCrBSi coating on steel substrate by nanoindentation,” *Mater. Sci. Eng. A*, vol. 528, no. 1, pp. 425–428, Nov. 2010, doi: 10.1016/j.msea.2010.09.028.
 - [9] M. Hardiman, T. J. Vaughan, and C. T. McCarthy, “The effects of pile-up, viscoelasticity and hydrostatic stress on polymer matrix nanoindentation,” *Polym. Test.*, vol. 52, pp. 157–166, 2016, doi: 10.1016/j.polymertesting.2016.04.003.
 - [10] J. Gong, B. Deng, and D. Jiang, “A universal function for the description of nanoindentation unloading data: Case study on soda-lime glass,” *J. Non. Cryst. Solids*, vol. 544, pp. 120067-1–8, 2020, doi: 10.1016/j.jnoncrysol.2020.120067.
-